The integration of spaceborne accelerometry in the precise orbit determination of low-flying satellites

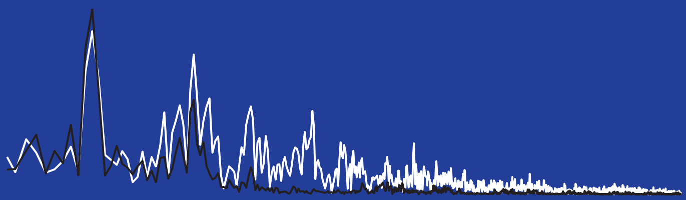

Tom Van Helleputte

Tom Van Helleputte

The integration of spaceborne accelerometry in the precise orbit determination of low-flying satellites

The integration of spaceborne accelerometry in the precise orbit determination of low-flying satellites

Proefschrift

ter verkrijging van de graad van doctor
aan de Technische Universiteit Delft,
op gezag van de Rector Magnificus prof.ir. K.C.A.M. Luyben,
voorzitter van het College voor Promoties,
in het openbaar te verdedigen op dinsdag 18 januari 2011 om 12:30 uur

door

Tom VAN HELLEPUTTE

ingenieur luchtvaart & ruimtevaart
geboren te Gent, België

Dit proefschrift is goedgekeurd door de promotor:

Prof.ir. B.A.C. Ambrosius

Copromotor:

Dr.ir. P.N.A.M. Visser

Samenstelling promotiecommissie:

Rector Magnificus,	voorzitter
Prof.ir. B.A.C. Ambrosius,	Technische Universiteit Delft, promotor
Dr.ir. P.N.A.M. Visser,	Technische Universiteit Delft, copromotor
Prof.dr. E.K.A. Gill,	Technische Universiteit Delft
Prof.ir. K.F. Wakker,	Technische Universiteit Delft
Prof.Dr.-Ing. R. Rummel,	Technische Universität München, Germany
Dr. O. Montenbruck,	Deutsches Zentrum für Luft- und Raumfahrt, Germany
Ir. R.H.N. Haagmans,	ESA/ESTEC - European Space Agency
Prof.dr.ir. R.F. Hanssen,	Technische Universiteit Delft, reservelid

Publicatie van het proefschrift is mede mogelijk gemaakt door een financiële bijdrage van de vakgroep Astrodynamica en Satellietsystemen, faculteit Lucht- en Ruimtevaarttechniek, Technische Unversiteit Delft.

Printed by: DCL Print & Sign, Zelzate

Cover illustration: Tom Van Helleputte

since the Earth has left my feet,
I lost the touch of gravity ..

from *Losing Gravity*
by The Bony King Of Nowhere, 2009

radial distance (AU)	115.81
radial distance (million km)	17324.93
heliographic latitude (degrees)	34.4
heliographic inertial longitude (degrees)	173.8

Voyager 1 location in heliocentric coordinates
on 14/01/2011, according to 'Vgrlocations.pdf' on
http://voyager.jpl.nasa.gov/spacecraft/index.html

Contents

Summary

Satellites in low Earth orbits provide valuable insight on our planet. To meet the stringent requirements on the accuracy of the computed orbits geopotential Earth observation satellites are equipped with a high-precision GPS (Global Positioning System) receiver. Using these GPS observations, the orbit of the satellite is computed with a precision at the few cm level by precise orbit determination (POD) techniques. A recent development is the addition of a high sensitivity accelerometer on board of such satellite missions, to measure the non-gravitational forces acting on it. In the instrument transfer functions, biases and scale factors are introduced which are sensitive to instrument operations and the satellite environment. This leads to the necessity to calibrate the accelerometer measurements before using them. The objective of the research described in this dissertation is to develop, implement and validate a strategy to calibrate the accelerometer measurements of LEO satellites by processing them with precise GPS-based orbit determination techniques.

The CHAMP mission was the first Earth observation satellite to carry an ultrasensitive accelerometer, the STAR instrument. The GRACE mission carries its more precise successor SuperSTAR. The GOCE mission is based on differential accelerometry, with 6 even more precise accelerometers combined in a gradiometer configuration. The first accelerometers in space were used to measure the atmospheric drag acting on the spacecraft. Although not the main scientific goal, the accelerometer measurements of CHAMP and GRACE were soon applied for atmospheric profiling, and more specifically the retrieval of thermosphere density and winds. A driver for this research is an improved calibration of accelerometer measurements in support of the retrieval of thermosphere density [*Doornbos et al.*, 2009]. Data of the CHAMP and GRACE missions were processed for this study.

Because the orbit determination is done only with GPS observations, namely the undifferenced ionosphere-free linear combination, the performance of the GPS receivers used in this research is analyzed. This analysis confirms their high quality. The BlackJack receiver on CHAMP and GRACE and the GRAS receiver, flying on MetOp-A and based on the same chipset as the Lagrange receiver flying on GOCE, show a comparable quality. The Lagrange receiver on board of GOCE proves to meet its requirements.

The least-squares orbit determination technique has been applied, comprising of the iterative adjustment of dynamical trajectory and measurement model parameters from a set of observations and implemented in the GHOST software. When applying the accelerometer measurements, they replace the non-gravitational accelerations computed from force models and are directly inserted into the equation of motion. Scale and bias parameters are estimated in the least-squares adjustment procedure. For the estimation of the biases, especially in radial and cross-track direction, a good a priori value proved to be necessary because of high correlations of this parameter with the initial conditions of the orbit (position and velocity at start time). The a priori bias value is determined by the difference between the mean of modeled non-gravitational accelerations and the mean of the accelerometer measurements. It was found that in these two directions the GPS-based POD technique serves more as validation than as calibration. The estimation of empirical accelerations in the POD, to compensate for deficiencies in the employed dynamical models, improves the orbit determination, while the values of the calibration parameters hardly change.

Five years (2003-2007) of CHAMP and GRACE data are processed, computing daily calibration parameters. A strong anti-correlation between scale and bias parameters is apparent when estimating both scale and bias parameters with loose constraints. A stable (unconstrained) estimation of the scale factor, showing a small variation, occurs when the signal strength is large. Reversely, with a reducing acceleration strength due to a decreasing solar activity, the formal error increases, as well as the variation of the estimated parameter. Keeping the scale factor constant in all three directions results in much smoother bias values, showing a clear trend, and distinct jumps in the bias values are visible, which can be related to instrument behavior. The resulting GRACE orbits have a 3-dimensional RMS precision of around 3.5 cm compared to external trajectories, which is supported by SLR analysis. Phase residuals for GRACE fluctuate under the cm level and even reach 6 mm when phase center variations maps are incorporated.

The calibration benefits from a sequential procedure, where first daily biases and scale factors are estimated, after which the average of the scale factor is determined. In the next step, the scale factor is kept constant and new daily biases are estimated. The scale factor can also be estimated with a multi-arc technique, where the normal matrices are stacked for a long period and one scale factor is estimated for the whole period. With this technique the influence of the signal strength on the estimation becomes clear, as days with a stronger signal contribute more to the solution than days with a smaller signal. Therefore, the stacked matrices approach is conceptually a good technique to estimate the scale parameter.

Although also carrying accelerometers, GOCE differs from the CHAMP and GRACE missions. The flying altitude is much lower, resulting in higher aerodynamic forces acting on the satellite, which are compensated by the drag-free control system. On board of GOCE six accelerometers are combined into a gradiometer, with the common-mode accelerations formed by combining accelerometer measurements along a gradiometer axis. These common-mode accelerations are inserted in the orbit determination. When the satellite is not flying in drag-free mode, a scale factor in along-track and cross-track direction can be estimated unconstrained and values close to one are found. In radial direction the signal is too small to estimate a scale parameter. When the drag compensation is active, this only remains possible in cross-track direction, as now also in flight direction the signal is small. For a one month period when GOCE was not flying drag-free, the estimated scale factor in along-track and cross-track direction is stable, showing small variations. A second period has GOCE in science mode and flying drag-free. Now only the scale in cross-track direction is estimated freely and has a slightly higher variation, caused by the smaller signal as the drag-free compensation also works in this direction. In both cases the bias parameter in flight direction can be estimated reliably, and in the two other directions this parameter is constrained to a priori values, because of the before mentioned correlations with the initial conditions. These two months are also processed with the stacked matrices approach, and the obtained results support that the signal strength is the driving factor for a reliable estimation of the scale parameter. In general, it can be concluded that there is no indication that the scale factors for GOCE are statistically different from one.

The developed method to calibrate accelerometer measurements of LEO satellites with a GPS based orbit determination technique, produces reliable results in flight direction, when the acceleration signal is strong enough. In the other directions it more validates scale factors (obtained e.g with a multi-arc technique) and bias parameters derived from dynamic models, which can be further improved. The processing of the accelerometer data of CHAMP and GRACE will be continued for both missions, and as the analysis on GOCE data was limited in scope, more in depth analysis can be performed, like the application of individual accelerometer measurements in the POD and an assessment of the ion engine behaviour.

Samenvatting

Satellieten in een lage baan om de Aarde leveren waardevolle inzichten in onze planeet. Om te voldoen aan de vereisten gesteld aan de berekende banen zijn missies gericht op het aardse zwaartekrachtsveld uitgerust met een heel precieze GPS (Global Positioning System) ontvanger. Met deze GPS metingen wordt de baan van de satelliet door middel van precieze baanbepalingstechnieken berekend tot een paar cm nauwkeurig. Een recente ontwikkeling hierbij is het integreren van een uiterst gevoelige versnellingsmeter aan boord van dergelijke satelliet missies, om de niet-gravitationele versnellingen te meten. De metingen van dit instrument moeten gecorrigeerd worden voor calibratie parameters (schaal en constante meetafwijking, zogenaamd 'bias'), die beïnvloed worden door de aansturing van het instrument en de omgeving aan boord van de satelliet. Daarom moeten deze metingen gecalibreerd worden voor gebruik. Het doel van het onderzoek beschreven in deze dissertatie is daarom het ontwikkelen, implementeren en valideren van een strategie om de metingen van de versnellingsmeters aan boord van boven genoemde satellieten te calibreren, door ze te gebruiken in de precieze baanberekening gebaseerd op GPS metingen.

De CHAMP missie was de eerste aardobservatie-satelliet met een ultra-gevoelige versnellingsmeter aan boord, het STAR instrument. De GRACE missie gebruikt de meer preciese opvolger SuperSTAR. De GOCE missie tenslotte is gebaseerd op differentiële accelerometrie, met 6 versnellingsmeters gecombineerd in een gradiometer configuratie. De eerste versnellingsmeters in de ruimte werden gebruikt om de atmosferische weerstand die op het ruimtetuig werkt, te meten. Hoewel dit niet het primaire wetenschappelijke doel is van deze missies, werden de metingen van de versnellingsmeters aan boord van CHAMP en GRACE al snel gebruikt voor atmosferische profilering, namelijk het bepalen van de dichtheid van de thermosfeer. Een motivatie voor dit onderzoek is een verbeterde calibratie van de versnellingsmeter metingen ter ondersteuning van het bepalen van de dichtheid van de thermosfeer [*Doornbos et al.*, 2009]. Data van de CHAMP en GRACE missies zijn gebruikt voor deze toepassing.

Omdat de baanberekening uitsluitend gebaseerd is op GPS metingen, namelijk de niet-gedifferentieerde ionosfeer-vrije combinatie, zijn allereerst de prestaties van de GPS ontvangers gebruikt in dit onderzoek geanalyseerd. Deze analyse bevestigt hun hoge kwaliteit. In het bijzonder, hebben de BlackJack ontvanger van CHAMP en GRACE en de GRAS ontvanger, aan boord van MetOp-A, een vergelijkbare kwaliteit. Deze laatste is gebaseerd op dezelfde chipset als de Lagrange ontvanger aan boord van GOCE. Een eerste analyse van de Lagrange ontvanger toont aan dat die aan de voor de lancering gedefinieerde vereisten voldoet.

In het hier beschreven onderzoek is de methode van de kleinste kwadraten toegepast. Deze bestaat uit het iteratief aanpassen van een dynamische baan en parameters uit de GPS metingen. Dit is geïmplemteerd in de GHOST software. Wanneer versnellingsmetingen gebruikt worden, vervangen ze de niet-gravitationele versnellingen berekend uit krachtmodellen, en worden deze meegenomen in de bewegingsvergelijkingen. Schaal en bias parameters worden dan bepaald met de kleinste kwadraten schatting. Voor het schatten van de bias, vooral in radiale richting en de richting loodrecht op het baanvlak (aangeduid met 'normaal'), bleek een goede a priori waarde nodig te zijn, omwille van hoge correlaties met de initiële condities van de baan (positie en snelheid op het begintijdstip). Deze a priori waarde wordt bepaald door het verschil tussen het gemiddelde van gemodelleerde niet-gravitationele versnellingen en het gemiddelde van de versnellingsmeter metingen. Het blijkt dat in deze twee richtingen de precieze baanbepaling met GPS observaties meer als validatie dient dan als calibratie. Het meeschatten van empirische versnellingen, die fouten in de gebruikte dynamische modellen opvangen, verbetert de baanbepaling, terwijl de waarden van de calibratieparameters nauwelijks veranderen.

Vijf jaren (2003-2007) CHAMP en GRACE data zijn verwerkt, waarbij dagelijks calibratie parameters bepaald zijn. Een sterke anti-correlatie tussen schaal en bias parameters duikt op wanneer beide geschat worden met losse beperkingen. Een stabiele (vrije) schatting van de schaalfactor, die een kleine variatie vertoont, is mogelijk als de signaalsterkte groot is. Omgekeerd verhoogt de formele fout bij een afnemende sterkte van de versnellingen, veroorzaakt door de afnemende zonneactiviteit, waardoor ook de variatie van de geschatte parameter toeneemt. Een constante schaalfactor in alle richtingen resulteert in een kleinere spreiding van de bias waarden, die een duidelijke trend met afgelijnde sprongen tonen, die gerelateerd kunnen worden aan het gedrag van het instrument. De zo bepaalde banen van de GRACE satellieten hebben een 3-dimesionele RMS van ongeveer 3.5 cm vergeleken met externe banen. Dit werd ook bevestigd door analyse van laser afstands of SLR residuen. Fase residuen voor GRACE fluctueren onder de cm grens en halen zelfs 6 mm wanneer fase-centrum-variaties gebruikt worden.

De calibratie verbetert wanneer gebruik wordt gemaakt van een sequentiële procedure, waar eerst de dagelijkse schaal en bias paremeters geschat worden, en vervolgens het gemiddelde van de schaalfactor bepaald wordt. In de volgende stap wordt de schaalfactor constant gehouden en worden nieuwe dagelijkse bias waarden bepaald. De schaalfactor kan ook geschat worden met een 'multi-arc' techniek, waarbij de normaalmatrices opgeslaan worden voor een lange periode en één schaalfactor bepaald wordt voor de hele periode. Met deze techniek wordt de invloed van de signaalsterkte op de schatting duidelijk, omdat dagen met een sterker signaal meer bijdragen tot de oplossing dan dagen met een zwakker signaal. Daarom is deze multi-arc methode conceptueel een goede techniek om de schaalfactor te bepalen.

Hoewel GOCE ook versnellingsmeters aan boord heeft, verschilt deze missie van CHAMP en GRACE. De hoogte waarop deze satelliet vliegt is veel lager, wat een hogere aerodynamische weerstand als gevolg heeft. Deze weerstand wordt gecompenseerd door het zogenaamde 'drag-free' systeem. De zes versnellingsmeters aan boord van GOCE worden gecombineerd tot een gradiometer, waarbij de 'common-mode' versnellingen verkregen worden door het het gemiddelde te nemen van versnellingen langs één arm van de gradiometer. Deze common-mode versnellingen worden gebruikt in de ontwikkelde techniek en komen grotendeels overeen met vesnellingen zoals gemeten door één versnellingsmeter in het massamiddelpunt van de satelliet (zoals bij CHAMP en GRACE). Wanneer de luchtweerstand niet gecompenseerd wordt, kan in vlieg- en normale richting een schaalfactor vrij geschat worden, met waarden dicht bij één als resultaat. Radiaal is het signaal te klein om een schaalfactor te kunnen schatten. Als de compensatie van de weerstand actief is, kan enkel in normale richting nog een schaalfactor geschat worden, omdat nu ook in vliegrichting het signaal te klein is. Gedurende een maand wanneer GOCE vloog zonder compensatie van de weerstand, is de schaalfactor in vlieg- en normale richting stabiel, en toont deze een kleine variatie. Tijdens een tweede periode vloog GOCE in wetenschappelijke modus, met compensatie van de luchtweerstand. Nu kan enkel in normale richting een schaalfactor geschat worden, die een iets hogere variatie toont, daar het signaal ook kleiner is omdat de compensatie van de weerstand ook deels in deze richting werkt. In beide gevallen kan de bias parameter in vliegrichting betrouwbaar geschat worden. In de twee andere richtingen wordt deze parameter sterk beperkt tot a priori waarden, omwille van de boven genoemde correlaties met de initiële condities. Deze twee periodes zijn ook verwerkt met de multi-arc methode, en de behaalde resultaten bevestigen dat de signaalsterkte de bepalende factor is voor een betrouwbare schatting van de schaal parameter. Algemeen kan gesteld worden dat er geen indicatie is dat de schaalfactoren van GOCE statistisch beduidend afwijken van één en dat de metingen dus goed gecalibreerd zijn.

De ontwikkelde methode om metingen van versnellingsmeters aan boord van satellieten in lage banen om de Aarde te calibreren, produceert betrouwbare resultaten in vliegrichting, wanneer het signaal van de versnelling sterk genoeg is. In de andere richtingen is de techniek meer een validatie van de schaalfactoren (bijvoorbeeld bepaald met een multi-arc techniek) en bias waarden bepaald uit dynamische modellen. Deze modellen kunnen verder verbeterd worden. Het verwerken van CHAMP en GRACE data zal gecontinueerd worden voor de levensduur van beide missies. Omdat de analyse van resultaten van de GOCE satelliet gezien de recente beschikbaarheid beperkt was in tijd en omvang, kan in de toekomst een meer diepgaande analyse uitgevoerd worden. Hierbij kan ook het gebruik van individuele versnellingsmeters in de baanbepaling onderzocht worden, als ook het gedrag van de ionenmotor, die gebruikt wordt voor de compensatie van de weerstand.

Chapter 1

Introduction

The past decades, low Earth orbit (LEO) has proven to be an excellent observation platform for our planet. Satellites in orbit around the Earth continue to provide valuable insight in meteorology, climatology, ocean currents, the Earth interior, etc. These satellite missions have stringent requirements on the accuracy of the computed orbits, ranging from a few decimeters for earlier missions to the centimeter level for current and upcoming missions. Errors larger than the specified tolerances affect the mission objectives, e.g. the use of altimeter data for oceanography and glaciology or the recovery of the global Earth gravity field. Therefore such satellites are equipped with high-precision tracking systems like retro-reflectors for satellite laser ranging (SLR) and DORIS or GPS (Global Positioning System) receivers. With the data stemming from such tracking systems the orbit of the satellite can be determined by precise orbit determination (POD) techniques.

A more recent development is the addition of a highly sensitive accelerometer on board of a geopotential satellite mission, to measure the non-gravitational forces acting on it. During the gravity field recovery these measurements help to separate gravitational and non-gravitational contributions in the observed orbit perturbations. The first mission to carry such a high class accelerometer is CHAMP (CHAllenging Minisatellite Payload), led by the GeoForschungsZentrum (GFZ) in Potsdam [*Reigber et al.*, 2002] and launched in July 2000. A second one is GRACE (Gravity Recovery And Climate Experiment), a joint US-German mission for accurate determination of the Earth gravity field and its temporal variation [*Tapley et al.*, 2004*b*], launched in March 2002. The most recent is ESA's GOCE (Gravity field and steady-state Ocean Circulation Explorer) mission [*ESA*, 1999], launched in March 2009. GOCE carries six accelerometers, orthogonally aligned in three pairs close to the spacecraft's center of mass, as a gradiometer. The future Swarm mission [*Friis-Christensen et al.*, 2008] is foreseen to consist of three satellites, each carrying an accelerometer.

For precise orbit determination purposes all these missions have a dual-frequency

GPS receiver on board. The application of dual-frequency GPS receivers as main tracking instrument is evolved into a mature and scientifically well researched technique. CHAMP and GRACE are equipped with a Black-Jack receiver developed by the Jet Propulsion Laboratory (JPL), while GOCE flies a Lagrange receiver developed by Thales Alenia Space (formerly Laben). When the spacecraft carries an accelerometer, the measured accelerations can be used to replace the models of the non-gravitational forces, such as air drag and solar radiation pressure, in the orbit determination.

This dissertation focusses on the latter, where the accelerometer measurements are introduced in the orbit determination, replacing the accelerations derived from non-gravitational force models, in an effort to calibrate them. The next section presents an overview of space borne accelerometry, followed by the objective and motivation of this research and its contribution to the field of precise orbit determination (with accelerometer data). A brief introduction of the satellite missions mentioned above (CHAMP, GRACE and GOCE) is given thereafter, as GPS and accelerometer data of these missions were processed and the results are presented and discussed in this dissertation. This introductory chapter is concluded with a detailed outline of all other chapters.

1.1 Accelerometers on board a spacecraft

Electrostatic space accelerometers have been developed since the seventies. The Discos [*DeBra*, 1973] and the Cactus instruments have been respectively launched in 1972 and 1975 for drag compensation control or drag measurement. Both were designed around a high density proof mass, the motion of which is measured with three capacitive sensors. More recently, the ASTRE instrument (French acronym of Accelerometre Spatial TRiaxial Electrostatique) has been optimized for the monitoring of the manned spacecraft environment. The mechanical core of the sensor is defined with a silica core surrounding a parallelepiped proofmass made of titanium alloy. The ASTRE accelerometer flew three times on board the Columbia shuttle in 1996 and 1997. From the ASTRE experience, the STAR (Space Three axis Accelerometer for Research) instrument has been defined. STAR has an internal core configuration similar to ASTRE [*Touboul*, 2001].

The STAR accelerometer was specifically designed for the CHAMP mission, the first Earth observation satellite mission to carry an ultrasensitive accelerometer. The measurement of the surface forces acting on the satellite allows to replace relatively inaccurate non-gravitational force models by precise observations in the accurate determination of the orbit. The gravity signal is deduced from the continuous and three-dimensional tracking of the spacecraft relative to the GPS satellites, the so-called satellite-to-satellite tracking in the high-low mode (SST h-l). For the determination of the gravity anomalies at smaller scale, from wavelengths of several thousands down to below one hundred kilometers two other techniques are applied, the low-low satellite to satellite tracking (SST l-l, GRACE) and the gravity gradiometry (GOCE). For both, accelerometers with an extremely high resolution are necessary, which is for GRACE provided by the SuperSTAR instrument (with an update of the STAR configuration by modifying the core geometry, the position sensing and the electrostatic actuator sensitivities).

The GRACE mission, consisting of two satellites following each other, measures the relative motion of the two spacecraft, where again the accelerometer measurements are used to separate the non-gravitational force contributions from the gravitational ones in the SST h-l and l-l tracking [*Tapley et al.*, 2004*b*]. The GOCE mission is based on differential and common-mode accelerometry, with 6 accelerometers combined in a gradiometer configuration, orthogonally aligned in three pairs [*ESA*, 1999]. This gradiometer ultimately (after corrections) measures the gravity field gradients, the difference in gravitational attraction along the mounted directions, and the non-gravitational accelerations from the common-mode. These measurements are again combined with SST h-l tracking. GOCE is furthermore flying in a drag-free mode, where the atmospheric drag at satellite altitude is compensated by an ion thruster, with closed loop controls exploiting the accelerometer measurements. More sensitive accelerometers will be applied in future scientific missions in the domain of Fundamental Physics, also requiring satellites flying drag-free. This is e.g. the case for the LISA satellites [*Danzmann*, 2000] for the observation of gravity waves.

As stated in the beginning of this section, the first accelerometers in space were used to measure the drag on the spacecraft. Although not the main scientific goal of the before mentioned geopotential missions, the accelerometer measurements of CHAMP and GRACE were soon applied for atmospheric profiling, and more specifically the retrieval of thermosphere density and winds. Results on this topic can be found in [*Bruinsma et al.*, 2003], [*Doornbos et al.*, 2005], [*Liu et al.*, 2006] and [*B.D.Tapley et al.*, 2007]. The application of the accelerometer measurements in this field of research was also a driver for the research described in this dissertation, which is elaborated in the next section.

1.2 Research objective and motivation

The objective of this research is to develop, implement and validate a strategy to optimally calibrate the accelerometer measurements of LEO satellites by processing them with precise orbit determination techniques. Conventionally, accelerometer measurements are calibrated in gravity field recovery attempts, where the calibration is not a goal in itself, but a mandatory integral part of the gravity field retrieval. In this research, the calibration of the accelerometer measurements, the stability of the calibration parameters and the influence of the measurements on the achieved orbits is the main objective. The research outcome is insight in the modeling of non-gravitational forces in POD, application of the calibrated measurements in the retrieval of thermosphere density and winds and monitoring of the accelerometer instrument behavior.

As stated earlier, a driver for this research is improved calibration of accelerometer measurements in support of the retrieval of thermosphere density and winds from them. This was initiated by an ESA/ESTEC study on "Air density models derived from multi-satellite drag observations" [*Doornbos et al.*, 2009]. The study was performed by a group of 4 institutes, under the lead of the chair of Astrodynamics and Space Missions (of the Faculty of Aerospace Engineering, Delft University of Technology). Previous studies in this field focused on the retrieval of density from one sole mission, where the focus of this study was on the gathering of measurements from different observation platforms, in view of the Swarm mission, which consists of three satellites, all equipped with an accelerometer. Data of the CHAMP and GRACE missions were processed for this study.

The recently launched GOCE satellite flies in a very low orbit, at around 250 km altitude. This poses high challenges on the orbit determination and the calibration of the gradiometer. Furthermore it is flying in a drag-free mode, where the drag is compensated by the thrust of an ion engine, which is the first application of this technique in a scientific space mission. Because of the drag-free control, the accelerometer signal along the orbit is small, which is a big difference compared to the other two missions, where the accelerometer signal along the orbit is the largest (mainly consisting of atmospheric drag). The developed methods in this dissertation can also be tested on the GOCE data, and be compared with other calibration efforts and orbit determination products. Part of this research was done in the framework of the High Processing Facility (HPF) [*Koop et al.*, 2006], an ESA project performed by the European GOCE Gravity-Consortium (EGG-C), a group of ten European institutes, of which the chair of Astrodynamics and Space Missions is one. The purpose of the HPF is the processing of Level 1b data stemming from the GOCE satellite (gradiometer measurements, GPS and attitude data) to Level 2 data, consisting of calibrated gravity field gradients, the Earth's static gravity field and precise orbits of the satellite.

1.3 The CHAMP, GRACE and GOCE satellite missions

Throughout this research extensive use is made of GPS and accelerometer data from the CHAMP and GRACE satellite missions, and also data of the recently launched GOCE satellite are processed. A brief overview of these missions is presented here.

The Challenging Minisatellite Payload (CHAMP), illustrated in Figure 1.1, is a German small satellite mission for geoscientific and atmospheric research and applications. On 15 July 2000 CHAMP was launched into an almost circular, near polar orbit with an initial altitude of approximately 454 km. CHAMP's ten-year anniversary has been celebrated and it is expected to re-enter in autumn 2010. The primary mission objectives comprise the accurate determination of the Earth's gravity field, the estimation of the magnetic field including its spatial and temporal variations, and modeling the physical properties of the troposphere and ionosphere. To achieve this, the satellite is equipped with the STAR accelerometer, a JPL BlackJack GPS receiver, multiple magnetometers on a long boom and an autonomous star sensor. A more detailed description of the CHAMP mission can be found in [*Reigber et al.*, 1996].

The JPL BlackJack GPS receiver onboard of the CHAMP satellite is connected to four GPS antennas. A zenith-mounted antenna equipped with a choke ring and a typical cone of 80° serves as prime antenna for precise orbit determination, with a backup POD antenna mounted next to it. On the rear side of the spacecraft a helix antenna for occultation measurements can be found. The fourth antenna is mounted on the bottom side (nadir pointing) and was planned to be used for GPS altimetry. For this research only the GPS data collected by the primary POD antenna are used, for precise orbit determination and data quality assessment.

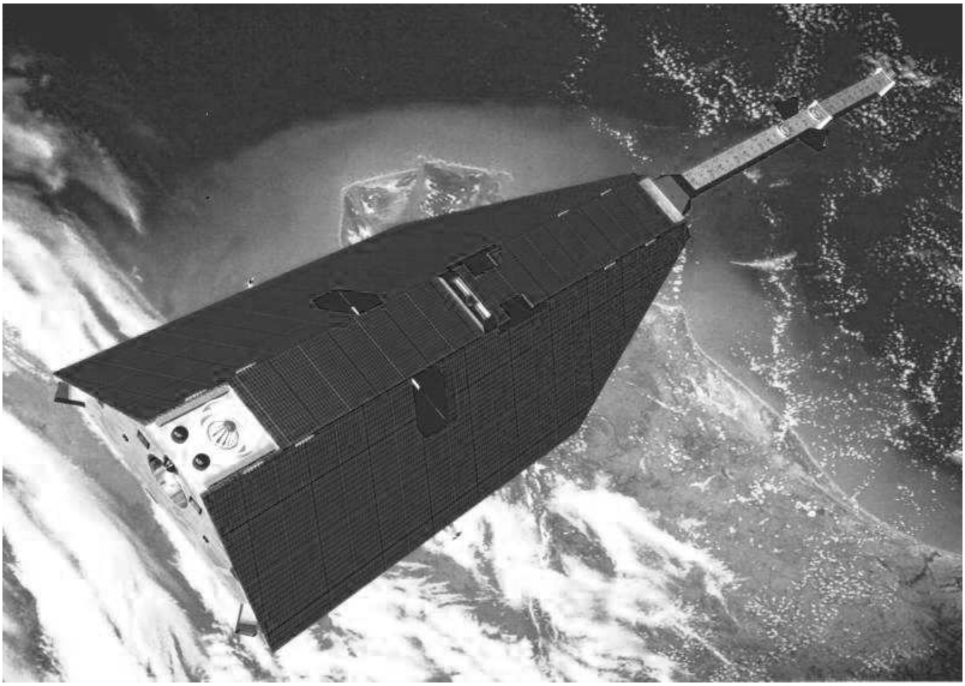

Figure 1.1 Artist's impression of the CHAMP satellite in orbit (Source: Astrium GmbH)

The Gravity Recovery and Climate Experiment (GRACE) mission (Figure 1.2) consists of two identical formation flying spacecraft in a near polar, near circular orbit with an initial altitude of approximately 500 km. They were launched on March 17 2002. The same bus design as for the CHAMP satellite was applied, without the frontal boom. The spacecraft have a nominal separation of 220 km. The primary mission objective is to measure the time varying changes in the Earth's gravity field, which is accomplished by the mission's key instruments, the Ka-Band Ranging System (KBR), the SuperSTAR accelerometers and the BlackJack GPS receivers. The KBR instrument measures the change in distance (biased range) between both spacecraft, which is a measure for the change in gravity, within a precision at the micron level. A complete overview of the entire GRACE mission can be found in [*NASA*, 2002].

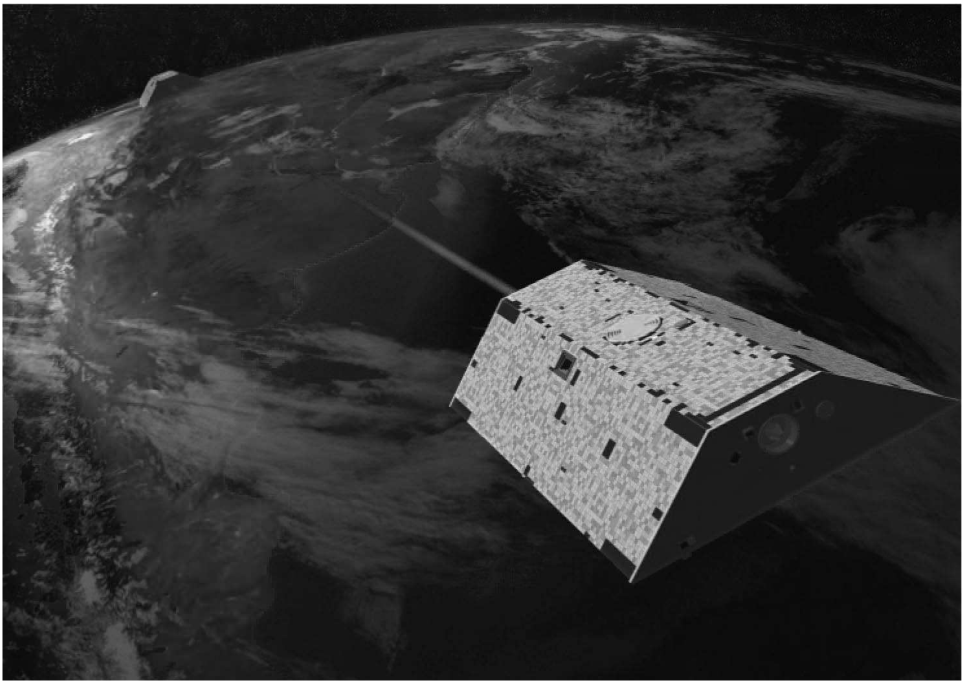

Figure 1.2 Artist's impression of the GRACE satellites in orbit (Source: CSR, University of Texas). The KBR link is illustrated as a beam between the two spacecraft

The Gravity field and steady-state Ocean Circulation Explorer (GOCE) satellite, depicted in Figure 1.3, was launched on March 17 2009, exactly seven years after the GRACE satellites. It is the first mission of ESA'a core Earth Explorer program [*Drinkwater et al.*, 2003]. It is the first satellite to apply gradiometry in space, carrying six highly accurate accelerometers, arranged in pairs along three orthogonal axes. This instrument allows the accurate recovery of the static gravity field of the Earth. To obtain a high sensitivity to the short wavelengths of the gravity field, the satellite flies in an unusually low circular orbit, at an altitude of 254 km. To maintain this orbit under the influence of high anticipated drag forces, the satel-

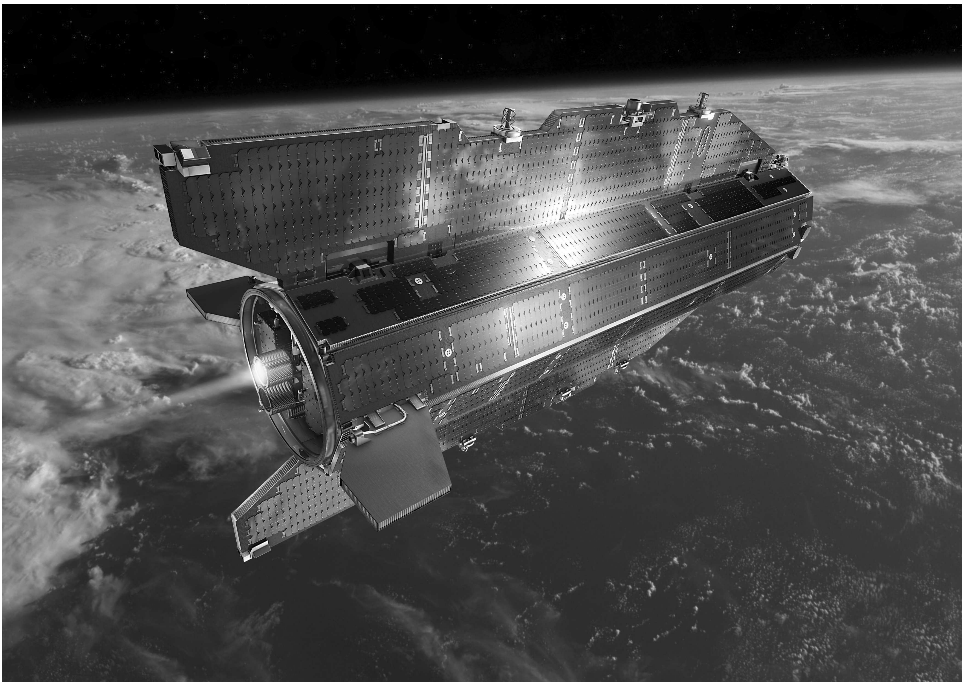

Figure 1.3 Artist's impression of the GOCE satellite in orbit (Source: ESA - AOES Medialab). The ion propulsion is illustrated at the back of the spacecraft

lite is equipped with an ion thruster, which counteracts the measured atmospheric drag. The mission duration is expected to be around 20-30 months, depending on the level of solar activity and fuel budget. The common mode of all accelerometers contains the signal due to the non-gravitational forces, augmented with the continuous accelerations of the ion thruster. For POD purposes, the satellite carries a dual-frequency Lagrange GPS receiver.

1.4 Outline

Because the orbit determination applied in this dissertation is done with GPS observations, chapter 2 provides a detailed overview of the different types of observations used. It deals with the observation modeling, as well as with data quality aspects, including the analysis of systematic errors and thermal noise in the GPS observation data. At the end of the chapter the receiver performance of several space borne GPS receivers is analyzed.

Chapter 3 deals with the forces acting on a spacecraft, both gravitational and non-gravitational. The models applied in the POD are introduced and at the end of the chapter the accelerometer instrument is described.

In chapter 4 the theory of precise orbit determination using GPS observations and its implementation is discussed. The implemented reduced dynamic batch Least-Squares (LSQ) estimator is discussed in detail, followed by the method developed to calibrate the accelerometer measurements by precise orbit determination.

Results of the CHAMP and GRACE calibration efforts are presented in chapter 5.

Because the GOCE mission differs largely from the CHAMP and GRACE missions, first results of GOCE data processing are presented separately in the sequent chapter 6.

At the end of this dissertation the conclusions, recommendations and ideas for future study are presented (chapter 7).

Chapter 2

GPS observations

The Global Positioning System (GPS), developed by the United States Department of Defense, is the most mature Global Navigation Satellite System (GNSS) available, next to the Russian GLONASS, the European GALILEO system, currently under development and intended to be operational by 2013, and the Chinese Compass system, also in the startup phase. Although initiated for military purposes, GPS became available to the scientific and commercial world, both benefiting from it. The latter has today led to the denomination of the acronym to a (portable) car navigation system.

The system consists currently (Feb. 2009) of 31 active satellites (nominally 24) in a constellation of near circular orbits with a radius of 26500 km, divided over 6 orbital planes equally spaced around the equator with an inclination of 55°. This sphere of satellites provides an attractive tracking system for a Low Earth Orbiting (LEO) spacecraft, because it allows for autonomous and continuous tracking in three dimensions, with a coverage of typically 7 or more GPS satellites, excluding the need for ground stations or elaborate antenna pointing. After the successful demonstration of GPS tracking for precise orbit determination on board of the TOPEX/Poseidon satellite [*Yunck et al.*, 1993], availability of flight-proven and affordable space borne receivers increased and GPS has nowadays evolved into a well established and accepted tracking system.

GPS positioning is based on the one way measurement of the signal travel time from GPS satellite to receiver. Multiplication with the speed of light gives the range between satellite and receiver. For this purpose a common reference time, GPS time, has been defined which has a constant offset of -19 seconds with respect to the international atomic time (TAI). The GPS satellites are equipped with atomic clocks, whereas the receivers use temperature compensated crystal oscillators in most cases. Both types experience a clock offset δt, which has to be corrected for, causing the respective GPS satellite (^{s}) and receiver ($_r$) internal times, as function of the GPS system time t, to become:

$$\begin{aligned} t^s(t) &= t + \delta t^s(t) \\ t_r(t) &= t + \delta t_r(t) \end{aligned} \tag{2.1}$$

The first two sections of this chapter deal with the observation types and linear combinations used in the orbit determination applied in this dissertation. A thorough discussion can be found in [*Misra and Enge*, 2001]. In addition, the observation modeling is discussed and at the end of this chapter the tracking performance and data quality of space borne GPS receivers on board of the CHAMP, GRACE, MetOp-A and GOCE spacecrafts is presented. The GRAS receiver of MetOp-A is interesting because this instrument is the first European built GPS receiver and is based on the same chipset [*Silvestrin et al.*, 2000] as the Lagrange receiver on board of GOCE.

2.1 Observation types

Each GPS satellite transmits data on two L-band carrier waves, with frequencies of 1575.42 MHz and 1227.60 MHz, an integer multiplication of the base frequency of the satellite's atomic clock of 10.23 MHz. Both frequencies are modulated with Pseudo Random Noise (PRN) codes for acquisition and tracking of the GPS signal. The first frequency L1 is modulated with the Coarse Acquisition (C/A) code and the second frequency L2 only with the Precision (P) code. The C/A code is accessible to all users, whereas the P-code is encrypted to the P(Y) code, only observable by authorized users. Several techniques, such as (semi-)codeless tracking, have been developed allowing the observation of the P code without the decryption key, at the expense of a lower Signal to Noise Ratio (SNR) and precision [*Woo*, 2000]. Since 2005 the L2C signal is broadcasted on newly launched GPS satellites, which is transmitted on the L2 frequency, but is not encrypted, allowing civil receivers to receive the full SNR [*Meehan et al.*, 2006]. In 2009 a third frequency L5 is implemented, at 1176.45 MHz, modulated with two extra codes. These new signals are not yet supported by presently available spaceborne GPS receivers.

A GPS receiver can measure three different types of observations: code or pseudorange observations, where a copy of the code in the receiver is correlated with the transmitted one to retrieve the signal travel time; carrier phase observations, where the phase of the received carrier wave is compared with the sent one; and the range-rate or instantaneous Doppler observation, where the Doppler shift of the received signal is measured. This research makes use of only the range and phase observations, therefore in the next sections the code and carrier phase observations are discussed in more detail, following [*Husti*, 2000].

2.1.1 Code observations

The code observations are a direct measure of the signal travel time and thus of the range between the antenna phase centers of the transmitting GPS satellite and the receiver. The observed signal travelling time $t_r^s(t)$ at epoch t is written as:

$$t_r^s(t) = t_r(t) - t^s(t - \tau_r^s(t)) \tag{2.2}$$

in which $t_r(t)$ is the receiver time of reception and $t^s(t - \tau_r^s(t))$ is the satellite time of signal transmission. The true signal travelling time is denoted as $\tau_r^s(t)$. Substitution of (2.1) into (2.2) yields

$$t_r^s(t) = \tau_r^s(t) + \delta t_r(t) - \delta t^s(t - \tau_r^s(t)) \tag{2.3}$$

Multiplication of this expression with the speed of light and substitution of the geometric range between the GPS satellite and receiver antenna phase centers, $\rho_r^s(t) = c\tau_r^s(t)$, results in a first approximation of the pseudorange observation

$$P(t) = \rho_r^s(t) + c(\delta t_r(t) - \delta t^s(t - \tau_r^s(t))) \tag{2.4}$$

The actual observation however is affected by different error sources: atmospheric effects, instrumental delays in the receiver and satellite, signal multipath and other systematic errors, and thermal measurement noise. Since this dissertation solely focuses on space applications the only atmospheric effect influencing the observations is the ionospheric delay. Stretching from roughly 50 to 1000 km above the Earth's surface, the ionosphere consists of ions and free electrons and has a frequency dependent effect on radio waves. The first order ionospheric path delay is proportional to the inverse square of the carrier frequency, $\Delta I(t, f) \sim 1/f^2$, which allows for the elimination of this term if dual frequency data are available, as formulated in section 2.2.1.

The measurement thermal noise of the code observation, $\epsilon_P(t)$, is assumed to be purely random with a zero mean and is typically on the decimeter level for geodetic grade receivers. All other errors and biases are contained in one term $M_P(t)$,

$$M_P(t) = b_{iP}(t) + m_P(t) + s_P(t) \tag{2.5}$$

where the GPS satellite and receiver hardware delays are grouped into a code bias on receiver tracking channel i, $b_{iP}(t)$, and the code multipath and other systematic effects are respectively given by $m_P(t)$ and $s_P(t)$. Finally the observation equation for a code observation on any of the two transmitting frequencies yields

$$P(t) = \rho_r^s(t) + c(\delta t_r(t) - \delta t^s(t - \tau_r^s(t))) + \Delta I(t, f) + M_P(t) + \epsilon_P(t) \tag{2.6}$$

2.1.2 Carrier phase observations

Most GPS receivers are also able of accurately tracking the carrier wave onto which the code is modulated. The observed carrier beat phase can be expressed as

$$\phi_r^s(t) = \phi_r(t) - \phi^s(t - \tau_r^s(t)) + N_\phi \tag{2.7}$$

and consists of a phase difference $\phi_r - \phi^s$ and an unknown integer number of carrier cycles N_ϕ. The GPS receiver carrier phase at the moment of signal reception is denoted by $\phi_r(t)$, and $\phi^s(t - \tau_r^s(t))$ represents the carrier phase of the GPS satellite at time of transmission. These last two terms can furthermore be written as

$$\begin{aligned} \phi_r(t) &= \phi_r(t_0) + f \cdot (t - t_0) + f \cdot (\delta t_r(t) - \delta t_r(t_0)) \\ \phi^s(t - \tau_r^s(t)) &= \phi^s(t_0) + f \cdot (t - \tau_r^s(t) - t_0) + f \cdot (\delta t^s(t - \tau_r^s(t)) - \delta t^s(t_0)) \end{aligned} \tag{2.8}$$

where $\phi_r(t_0)$ and $\phi^s(t_0)$ represent the initial phases at t_0 of the GPS receiver and GPS satellite and f the transmitting frequency. Substitution of these expressions into (2.7) yields

$$\phi_r^s(t) = f\tau_r^s(t) + f \cdot (\delta t_r(t) - \delta t^s(t - \tau_r^s(t)) + A \tag{2.9}$$

in which the ambiguity or bias term

$$A = N_\phi + \phi_r(t_0) - f\delta t_r(t_0) - \phi^s(t_0) + f\delta t^s(t_0) \tag{2.10}$$

is a real valued parameter, which is constant over a continuous tracking arc.

After multiplication of (2.9) with the signal wavelength λ and introducing the same kind of error sourcess as for the code observation, the carrier phase observation equation is given by

$$L(t) = \rho_r^s(t) + c(\delta t_r(t) - \delta t^s(t - \tau_r^s(t))) - \Delta I(t, f) + \lambda A + M_L(t) + \epsilon_L(t) \tag{2.11}$$

The first order ionospheric correction to the phase observation has the same magnitude as for the code observation but an opposite sign, because the ionosphere causes an advance on the phase and similarly a delay on the modulated code observation. The measurement noise $\epsilon_r(t)$ is again assumed purely random with a zero mean. All other errors are given by

$$M_L(t) = b_{iL}(t) + m_L(t) + s_L(t) \tag{2.12}$$

The hardware delays from both receiver and satellite for the phase observable are grouped into an additional phase bias on the receiver tracking channel i, $b_{iL}(t)$, and the carrier phase multipath and systematic errors are given by $m_L(t)$ and $s_L(t)$. The thermal noise of the carrier phase measurement $\epsilon_L(t)$ typically is on the mm level and multipath errors are confined to a quarter of the signal wavelength, making this observation type much more precise than code observations.

The major differences between the code and carrier phase observations are the overall precision, the fact that the carrier phase observations are ambiguous and the opposite sign of the ionospheric delay (see also section 2.4 on the tracking performance).

2.1.3 Dual frequency observations

All data analyzed in this dissertation are originating from receivers capable of tracking both GPS frequencies. Therefore the dual frequency model for the P-code and accompanying carrier phase measurements obtained from a same GPS satellite is summarized as

$$
\begin{aligned}
P_1(t) &= \rho_r^s(t) + c(\delta t_r(t) - \delta t^s(t - \tau_r^s(t))) + \Delta I_1(t) & &+ M_{P_1}(t) + \epsilon_{P_1}(t) \\
P_2(t) &= \rho_r^s(t) + c(\delta t_r(t) - \delta t^s(t - \tau_r^s(t))) + \Delta I_2(t) & &+ M_{P_2}(t) + \epsilon_{P_2}(t) \\
L_1(t) &= \rho_r^s(t) + c(\delta t_r(t) - \delta t^s(t - \tau_r^s(t))) - \Delta I_1(t) + \lambda_1 A1 & &+ M_{L_1}(t) + \epsilon_{L_1}(t) \\
L_2(t) &= \rho_r^s(t) + c(\delta t_r(t) - \delta t^s(t - \tau_r^s(t))) - \Delta I_2(t) + \lambda_2 A_2 & &+ M_{L_2}(t) + \epsilon_{L_2}(t)
\end{aligned}
\tag{2.13}
$$

Here, the subscripts 1 and 2 denote the different frequencies, f_1 and f_2. Although not given here, when needed the C/A code and carrier phase observables can be modeled in exactly the same way as the P_1 and L_1 observables respectively. Furthermore, it must be pointed out that in the dual frequency model the geometric range $\rho_r^s(t)$ is assumed to be the same for each observation. As pointed out by [*Teunissen and Kleusberg*, 1998] this is not the case in reality, since the signal travelling time slightly varies for each of the frequencies, but with less than $0.1\mu s$. This results in sub-mm position differences for the GPS satellites, which are negligible compared to the other errors that are present in the observations.

As stated earlier, the thermal noise for each of the observations is assumed to be purely random with a zero mean. Furthermore, an important assumption is that individual observations from a single GPS receiver are completely uncorrelated temporally, spatially and also between the different observation types and frequencies. This means that the covariance matrix of the observation vector is diagonal where the entries are derived from the assumed precision of the observations. In this research the ionospheric-free combination is applied, introduced in the next section, leading to a 2x2 diagonal covariance matrix $\mathbf{Q_z} = [\sigma^2_{P_{IF}}\ \sigma^2_{L_{IF}}]$.

2.2 Linear data combinations

Several linear combinations can be derived from the above presented dual frequency observations in support of precise orbit determination and for assessing the quality of the receiver. Two such combinations are discussed here briefly.

2.2.1 Ionosphere free linear combination

This linear combination eliminates the first order ionospheric path delay, thanks to the frequency-dependent effect on radio waves. It is the main observation combination used for the precise positioning applications described in this dissertation. For the code and carrier phase observations the ionosphere free ($_{\mathrm{IF}}$) combination yields

$$
\begin{aligned}
P_{\mathrm{IF}}(t) &= \tfrac{f_1^2}{f_1^2-f_2^2}P_1(t) - \tfrac{f_2^2}{f_1^2-f_2^2}P_2(t) \approx 2.546P_1(t) - 1.546P_2(t) \\
L_{\mathrm{IF}}(t) &= \tfrac{f_1^2}{f_1^2-f_2^2}L_1(t) - \tfrac{f_2^2}{f_1^2-f_2^2}L_2(t) \approx 2.546L_1(t) - 1.546L_2(t)
\end{aligned}
\tag{2.14}
$$

Applying this to the dual frequency observations results in the following parameterization

$$
\begin{aligned}
P_{\mathrm{IF}}(t) &= \rho_r^s(t) + c(\delta t_r(t) - \delta t^s(t-\tau_r^s(t))) &&+ M_{P_{\mathrm{IF}}}(t) + \epsilon_{P_{\mathrm{IF}}}(t) \\
L_{\mathrm{IF}}(t) &= \rho_r^s(t) + c(\delta t_r(t) - \delta t^s(t-\tau_r^s(t))) + \lambda_{\mathrm{IF}}A_{\mathrm{IF}} &&+ M_{L_{\mathrm{IF}}}(t) + \epsilon_{L_{\mathrm{IF}}}(t)
\end{aligned}
\tag{2.15}
$$

where it must be noted that the carrier phase ambiguity, A_{IF}, does no longer contain an integer part as a result of the non-integer multiplication with the ionospheric wavelength.

A less fortunate consequence of this linear combination is the 3 times higher noise value compared to the single-frequency measurements, as shown here for the pseudorange combination after application of the error propagation law:

$$
\begin{aligned}
\sigma_{P_{IF}} = \sqrt{2.546^2\,\sigma_{P_1}^2 + 1.546^2\,\sigma_{P_2}^2} &\approx \sqrt{2.546^2 + 1.546^2}\,\sigma_{P_1} \\
&\approx 3\,\sigma_{P_1}
\end{aligned}
\tag{2.16}
$$

under the assumptions related to the observation covariance matrix stated above ($\sigma_{P_1} = \sigma_{P_2}$ and $\sigma_{P_1P_2} = 0$).

2.2.2 Multipath combination

The multipath combinations [*Estey and Meertens*, 1999] can be used to assess multipath and systematic errors and the noise level of the pseudorange observations. They are constructed using a mix of code and carrier phase observations, where it is assumed that the systematic errors and noise of the carrier phase measurements are negligible compared to the ones of the code observations, and result in a geometry and ionosphere free observation. The first step is to derive an expression for the ionospheric path delay based on the carrier phase observations:

$$
\Delta I(t) = \frac{1}{\alpha-1}\big(L_1(t) - L_2(t)\big) - \frac{1}{\alpha-1}\big(\lambda_1 A_1 - \lambda_2 A_2\big)
\tag{2.17}
$$

Here, α is the factor describing the square of the ratio between the ionospheric path delays on both frequencies, $\alpha = f_1^2/f_2^2$. The multipath combinations are now formed by subtracting the respective carrier phase observations from their accompanying pseudoranges and substituting the just formed ionospheric delay. When neglecting the carrier phase noise and systematic errors, the multipath observation MP1

$$
MP1(t) = P_1(t) - \left(1 + \frac{2}{\alpha-1}\right)L_1(t) + \left(\frac{2}{\alpha-1}\right)L_2(t)
\tag{2.18}
$$

is parameterized as

$$MP1(t) \approx -\left(1+\frac{2}{\alpha-1}\right)\lambda_1 A_1 + \left(\frac{2}{\alpha-1}\right)\lambda_2 A_2 + M_{P_1}(t) + \epsilon_{P_1}(t) \tag{2.19}$$

consisting of a combined carrier phase bias, constant over a pass, and the systematic errors and the thermal noise of the pseudorange observations. Similar combinations can be formed for the C/A and P2 code observations. These linear combinations are used in section 2.4 for assessing the quality of space borne GPS receivers pseudorange data.

2.3 Observation modeling

When GPS observations are applied for positioning, they are modeled by replacing the terms on the right side of the observation equations (2.15) with known values or estimates of these terms. The differences of the observed and modeled measurements are used in an estimation process, which is further elaborated in chapter 4. The first term in the observation equation, the geometric range between the phase centers of the GPS satellite antenna and the receiver, involves a linearization around approximate values, causing the estimation process to be iterative. This is described in the next section together with some general remarks on the observation models, following [*Kroes*, 2006]. The orbits of the GPS satellites and the behavior of the GPS clocks are assumed to be known and taken from the International GNSS Service (IGS) [*Dow et al.*, 2005]. The associated IGS products are discussed as well.

2.3.1 Linearization for positioning

The parameterization of the geometric ranges $\rho_r^s(t)$ between the phase centers of the receiver and GPS satellite antennas in terms of antenna phase center positions introduces a non-linearity. The geometric range, the distance between the antenna phase center position of the the GPS satellite, $\mathbf{r}^s(t-\tau_r^s(t))$ and the GPS receiver, $\mathbf{r}_r(t)$, at the time of signal transmission and reception respectively, is given by:

$$\rho_r^s(t) = \|\mathbf{r}^s(t-\tau_r^s(t)) - \mathbf{r}_r(t)\| \tag{2.20}$$

When approximate values of both positions are obtained, the geometric range becomes

$$\rho_{r0}^s(t) = \|\mathbf{r}_0^s(t-\tau_r^s(t)) - \mathbf{r}_{r0}(t)\| \tag{2.21}$$

and a linearization around them yields

$$\rho_r^s(t) = \rho_{r0}^s(t) - \mathbf{e}_r^s(t)\cdot\Delta\mathbf{r}_r(t) + \mathbf{e}_r^s(t)\cdot\Delta\mathbf{r}^s(t) \tag{2.22}$$

with $\Delta\mathbf{r}_r(t)$ and $\Delta\mathbf{r}^s(t)$ the phase center position increments of the receiver and GPS satellite respectively, and the partial derivatives given by

$$\mathbf{e}_r^s(t) = \frac{\mathbf{r}_0^s(t - \tau_r^s(t)) - \mathbf{r}_{r0}(t)}{\|\mathbf{r}_0^s(t - \tau_r^s(t)) - \mathbf{r}_{r0}(t)\|} \tag{2.23}$$

equal to the line of sight vector between receiving and transmitting antenna. Substitution of this linearized range into the observation equations results in linear observation models, which are now suitable for use in positioning applications.

At this point it has to be noted that although the GPS observations are parameterized with the antenna phase center position(s) (increments), these are in general not the points of interest for positioning. Throughout this study all positions that are provided or estimated refer to the center of mass of either the GPS satellites or the spacecraft onto which the GPS receiver is mounted. The antenna phase center offsets with respect to the centers of mass of all satellites involved are accounted for in the different positioning applications. These offsets however, have virtually no impact on the linearization presented here.

Throughout this research the GPS satellite positions and clock offsets are obtained from external resources and are assumed known on every epoch, resulting in $\Delta\mathbf{r}^s(t) = 0$, and thus $\mathbf{r}^s(t) = \mathbf{r}_0^s(t)$. A discussion of these so-called GPS ephemerides is provided in the next section. It must however be noted that this introduces an additional uncertainty in the observation model since the externally generated GPS ephemerides data are only accurate to a certain level. Any error in a provided GPS satellite clock offset propagates directly into the observation equations, whereas GPS satellite position errors, $\epsilon_{\mathbf{r}^s}(t)$, affect the observations according to the previously derived linearization, $\mathbf{e}_r^s(t) \cdot \epsilon_{\mathbf{r}^s}(t)$.

Furthermore throughout this research the biases and errors, captured in the M_r^s terms of the different observations, are neglected and not corrected for, except when empirical phase patterns are applied, which account for phase center variations and are introduced in section 2.4.1. The neglected error sources are simply accounted for in the measurement variances, for which realistic values are determined using the data analysis in section 2.4.

The ionosphere free observation model, applied in the precise orbit determination, is now parameterized with the position increment of the GPS receiver antenna phase center, the GPS receiver clock offset and the ionosphere free carrier phase ambiguity. When these parameters are adjusted for using observations from multiple GPS satellites, it must be noted that the mean value of all unmodeled biases and errors over all observations cannot be separated from the GPS receiver clock offset and will therefore be biased. Since this will in general only result in a very slight time offset the impact of this effect on the accuracy of the final position is negligible, even for spaceborne GPS positioning applications where the GPS receiver in general moves faster than the GPS satellite. For completeness it has to be stated that constant phase channel biases can also not be separated from the carrier phase ambiguities. Again this has no direct consequence for the resulting position accuracy.

2.3.2 GPS satellite orbits and clocks

Any type of precise positioning application using GPS data requires an accurate knowledge of the GPS satellite positions and clock offsets. These GPS ephemerides are provided by the IGS, which began to provide precise GPS ephemerides information for geodetic users and surveyors as early as 1994 [*Kouba*, 2002] when GPS had almost reached its fully operational status. Within the IGS, various Analysis Centers derive their own, independent GPS orbit and clock solutions which are subsequently merged into combined IGS products applying proper weighting and quality control. Both the network of IGS ground stations and the quality of the resulting products have continuously increased over time.

The IGS provides three types of GPS ephemerides products: the final, rapid and ultra-rapid ephemerides. The final IGS ephemerides are released some 13 days after the end of a GPS week and have a reported position and clock accuracy of better than 5 cm [*IGSCB*, 2009]. The rapid products, in contrast, are available within 17 hours past the end of each day and, meanwhile, achieve an almost identical accuracy. The ultra-rapid orbit and clock products are made available four times per day and have a latency of 3 hours past the last GPS observations, with a similar accuracy for the orbit products and two times less accurate satellite clock estimates.

All types of IGS ephemerides products provide GPS orbit and clock offset data in the standard SP3 format [*Remondi*, 1991] on a regular 15 min grid. The positions and velocities in the SP3 format are provided in the Inertial Terrestrial Reference Frame (ITRF) [*McCarthy*, 1996] and relate to the center of mass of the GPS satellites. The regular grid point spacing allows for accurate polynomial interpolation of the GPS satellite position at the time of a measurement, which is accomplished using an 8^{th}-order Lagrange interpolation method. After interpolation to the epoch of interest the GPS satellite position is transferred to the transmission time, corrected for the Earth rotation during transmission and for the antenna phase center offset and variations. Another correction is added to account for the phase wind-up [*Wu et al.*, 1993], the phase shift due to a rotation of the transmitting antenna around its bore axis, which occurs when the GPS satellites' solar panels are oriented towards the Sun.

After the introduction of absolute antenna phase center corrections in the processing standards of the IGS in GPS week 1400 (November 2006), absolute GPS satellite-specific antenna offsets and variations became available [*Schmid et al.*, 2007]. Before that date, only fixed offsets per GPS satellite type were applied in the tools used throughout this dissertation. These were zero for Block IIR satellites and 0.279, 0 and 1.023 m for the Block II/IIA satellites in the GPS satellite body coordinate system, originating in the center of mass of the satellite.

In contrast to orbital data, high-order polynomial interpolation is not suitable for clock parameters due to the underlying random noise processes, and linear interpolation is therefore advisable. The errors resulting from the interpolation of clock data depend on the interval size and the Allan variance of the respective clock [*Kouba*, 2002] [*Zumberge and Gendt*, 2001]. Therefore, supplementary to the SP3 ephemerides products, clock offset data at 5 min intervals are made available as part of separate clock products. In response to the demand for even higher rate clock data, several IGS Analysis Centers, such as the Center for Orbit Determination in Europe (CODE) in Bern, Switzerland and the Jet Propulsion Laboratory (JPL) in Pasadena, CA, have made their clock solutions, now at 5 second intervals, and accompanying orbits publicly available. The high rate clock product is of particular relevance for the orbit determination of the GOCE spacecraft, which delivers RINEX data at 1 Hz. Throughout this dissertation, the use of a self-consistent product from a single IGS Analysis Center is preferred, therefore CODE high rate clocks and accompanying orbits are used [*Hugentobler et al.*, 2008]. When data are processed from before mid 2003, these high rate clocks were not yet available and IGS final products are applied.

Two relativistic corrections are considered following [*Hofmann-Wellenhof et al.*, 2001], one affecting the signal due to the space-time curvature, another affecting the satellite clock, as two clocks at different altitudes run at different rates in the vicinity of the gravitational field of the Earth. The latter also includes the special relativity term related to the varying spacecraft velocity.

2.4 Tracking performance of space borne GPS receivers

The quality of the GPS observations determines the achievable accuracy of GPS positioning applications. Ideally the data are only subject to random noise with zero mean and a small standard deviation. However, as discussed in the previous sections, GPS receivers are subject to channel biases, multipath and other types of systematic errors, all influencing the final position solution accuracy if not properly accounted for. Since for this research all these errors are neglected in the observation model, they have to be accounted for in the stochastic part. The combination of the unmodeled errors and the thermal measurement noise is still assumed to be uncorrelated and to have a zero mean, but with a higher variance than for thermal noise only. This section starts with the performance analyses of the BlackJack GPS receiver onboard the CHAMP and GRACE spacecraft, using data obtained from the main POD antennas in analogy with *Montenbruck and Kroes* [2003]. This provides an overview of the unmodeled errors and some background on the observation variances used for the CHAMP and GRACE orbit determination described in this dissertation. Next, the performance of the GRAS instrument on board of MetOp-A, launched in October 2006, is touched upon. Finally, a first analysis of the performance of Lagrange receiver on board of GOCE (launched in May 2009) is presented.

2.4.1 BlackJack receivers on board of CHAMP and GRACE

The BlackJack GPS receivers are developed specially for orbital applications and atmospheric profiling by radio occultation by NASA's JPL and are operational on several space missions, such as the altimeter mission Jason-1, the Earth observation ICESat (Ice, Cloud and land Elevation Satellite) and CHAMP and GRACE. The receivers on board of the latter spacecraft can track up to 10 satellites at the same epoch. Figure 2.1 presents a histogram of the useful GPS satellites per epoch for a day in 2005, derived from editing based on elevation angle, SNR value, the Position Dilution of Precision (PDOP) value and after removing outliers and cycle slips. Most of the time between six and ten observations can be used each epoch.

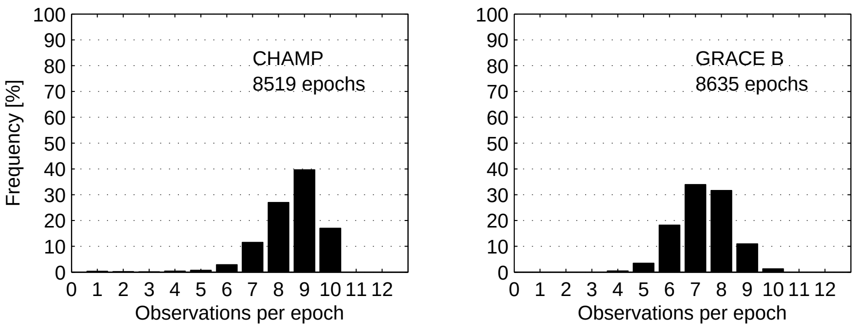

Figure 2.1 Histogram of the number of selected observations per epoch for the CHAMP and GRACE B satellites, for DOY 103 in 2005, with a 10 s time interval (maximum of 8640 epochs).

A pre-flight validation test of the BlackJack follow-up, the Integrated GPS Occultation Receiver (IGOR) flying on the German TerraSAR-X mission, gave insight on the receiver biases and correlations [*Montenbruck et al.*, 2005*b*]. Code biases resulted in displacements of 0.05 mm for the GPS satellites and 0.14 mm for a LEO spacecraft, values that can be neglected in POD applications. Inter-channel biases were small and around zero, and no evidence of correlation between the noise of the P_1 and P_2 code observations was found. Correlations between the noise of the carrier phase observations are expected, as show earlier for geodetic GPS receivers [*Tiberius et al.*, 1999], because the carrier phases of the encrypted codes cannot be properly tracked without the help of the C/A code phase and each other. A zero baseline test, required to find such correlations, was not carried out in the pre-flight validation test. Nevertheless all observations are treated as uncorrelated throughout this research.

Multipath, caused by the superposition of the direct signal with interfering signals, in case of spaceborne GPS exclusively caused by the satellite's surface reflections, is for the carrier phase confined to a quarter wavelength, while the maximum path delay for the code observations is of the order of the linear spacecraft dimension. Other types of systematic errors cannot be separated easily from multipath errors, because they mostly exhibit a similar pattern. Already shown in [*Montenbruck and Kroes*, 2003], the pseudorange data obtained from the CHAMP POD antenna are severely influenced by systematic errors, amounting to 0.6 m for low elevations. These errors were attributed to cross-talk interference between the GPS occultation and the POD antenna. As the occultation antenna on board of the GRACE spacecraft is only activated occasionally, systematic patterns for the individual code observations of the GRACE satellites were found to be on the sub-dm level in [*Kroes*, 2006]. The ionosphere free pseudorange systematic errors are slightly higher, around 2 dm. By collecting post-fit residuals of ionosphere free carrier phase observations the systematic errors on these measurements can be quantified. They are generally small and have maximum values of around 1 cm.

All GPS observations are subject to random thermal noise, with a level depending on the observation type and signal strength. Therefore the noise standard deviation is typically expressed as a function of the carrier to noise density ratio (C/N_0). The CHAMP and GRACE observation files contain the SNR value of all code and accompanying phase types, from which the carrier to noise density ratio can be derived. For the BlackJack receiver, following [*Montenbruck and Kroes*, 2003], this relationship is

$$C/N_0 = 20\log_{10}\left(\frac{\mathrm{SNR}}{\sqrt{2}}\right). \tag{2.24}$$

The noise level of the in-flight GPS code observations is assessed by grouping observation residuals of the multipath combination (2.18) in C/N_0 bins and calculating the standard deviation of each bin. Small systematic errors can still be present, so this value represents an upper limit of the code measurement noise standard deviation. The results of this analysis for a 20 day period in 2003 (DOY 201-220) are presented in Figure 2.2 for CHAMP and GRACE.

The low noise on the C/A code is caused by the fact that this observation can be tracked directly, whereas the P1 and P2 code observations are obtained using a form of semi-codeless tracking. The figure shows a large difference between the code noise for GRACE A and GRACE B, where the latter has the lower noise levels. The reason for the better performance of the receiver on board GRACE B remains unclear.

Some information on the carrier phase noise can be obtained from the difference between the carrier phase observations on the P1 and C/A code, L1 and LA. Since these are taken on the same frequency the ionospheric path delay and multipath

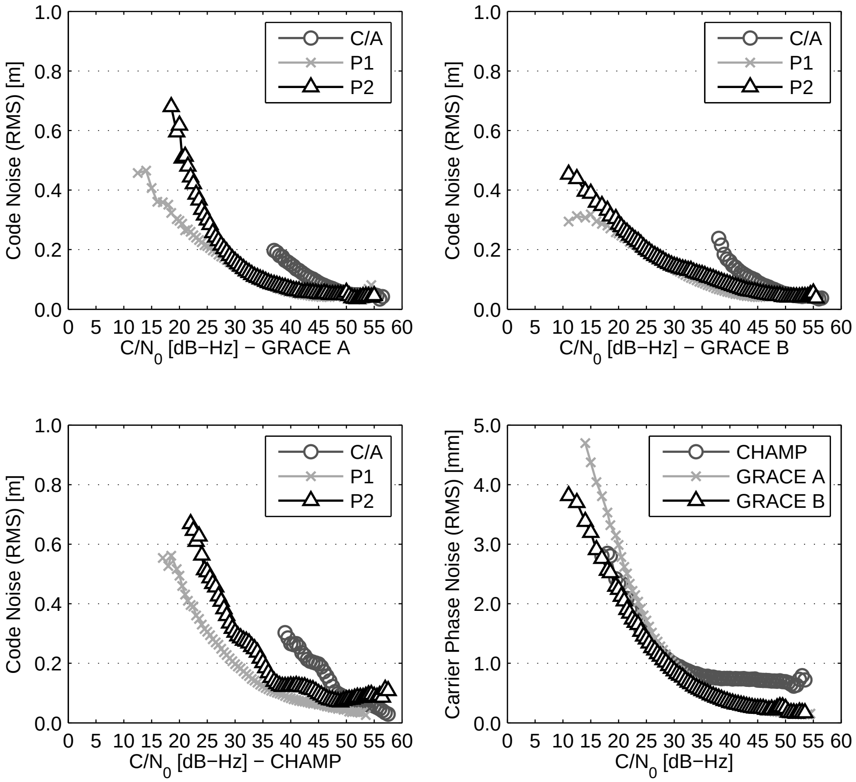

Figure 2.2 Code noise as function of the carrier to noise density ratio (C/N_0) for GRACE A and B (top) and CHAMP (bottom left) and upper limit for the phase noise on the L1 observation for the three satellites (bottom right).

and systematic errors are the same. When taking the difference of these observations the only parameters remaining are the difference between the (constant) carrier phase biases on each of the observations and the combined thermal noise. When again assuming no correlation, the combined noise

$$\sigma_{(L_1-L_A)} = \sqrt{\sigma_{L_1}^2 + \sigma_{L_A}^2} > \sigma_{L_1} > \sigma_{L_A}, \tag{2.25}$$

can now serve as an upper limit of the noise on L1, assuming this noise is larger than the one on the C/A code phase observable. For each continuous pass this carrier phase difference is constructed and corrected for its bias. The resulting carrier phase noise is then again grouped into C/N_0 data bins, from which a curve in analogy with the code noise is created. For all three satellites the carrier phase noise curves are presented in the bottom right plot in Figure 2.2, where again the noise of the GRACE A phase observation is slightly higher than of GRACE B.

Phase center variations of the receiver antenna remained for long an uncertainty for high precision orbit determination. A calibration of the Sensor Systems S67-1575-14 antenna, the main POD antenna on the satellites described here, has been conducted, triggered by the adoption of absolute phase patterns in the IGS processing standards. Nominal phase patterns were obtained and used in [*Montenbruck et al.*, 2008*a*] to asses the impact of the patterns on the positioning accuracy. Furthermore in-flight phase center distortions were obtained based on POD carrier phase residuals. It is shown that the combined ground and in-flight calibration improves the carrier phase modeling accuracy to a level of 4 mm, close to the receiver noise.

2.4.2 GRAS instrument on board of MetOp-A

The global navigation satellite system receiver for atmospheric sounding (GRAS) [*Loiselet et al.*, 2000] is the first European spaceborne GPS receiver providing dual-frequency navigation measurements on a routine basis. It flies on board of MetOp-A [*Edwards et al.*, 2006], launched in a near-polar orbit at 800 km altitude on 19 October 2006. The receiver is based on ESA's AGGA-2 correlator chip [*Silvestrin et al.*, 2000], which is also used in the Lagrange receiver [*Zin et al.*, 2007] flying on GOCE, and in new receivers under consideration for Swarm [*Reichinger et al.*, 2006] and Sentinel-3. MetOp is a joint project from ESA and Eumetsat, the European organisation for the exploitation of meteorological satellites. To asses the tracking performance of the GRAS instrument, a study has been performed by DLR, AUIB and DEOS on a 3-day data set for 26-28 December 2006. The results are presented in [*Montenbruck et al.*, 2008*b*] and are highlighted here. The receiver has an elevation limit of 10° and has eight channels available for tracking, with most of the time (98.7%) six or more GPS satellites tracked.

The ultrastable oscillator (USO) exhibits a frequency offset of about 3 ns/s, which results in an almost linear growth of the receiver time clock offset, accumulating to 0.5 ms over a 24 h arc, equal to a pseudorange offset of 150 km. A clock-offset correction prior to the use of the GRAS measurements is therefore desirable for POD applications. Because the oscillator is highly stable, the clock offset may be represented by a second order polynomial in receiver time. A frequency variation of $2\text{x}10^{-11}$/K was found, well within the specifications.

The carrier to noise density ratio has peak values of 57 dB-Hz for L1 C/A code tracking with a mean value of 40 dB-Hz at the 10° elevation limit. The variation of C/N_0 with elevation matches that of the receiver/antenna configurations on CHAMP and GRACE, despite different hardware design. For the semi-codeless P-code tracking on L1 and L2, the C/N_0 values vary between 50 dB-Hz at high elevations to a mean value of 19 dB-Hz at the low elevations. The semi-codeless

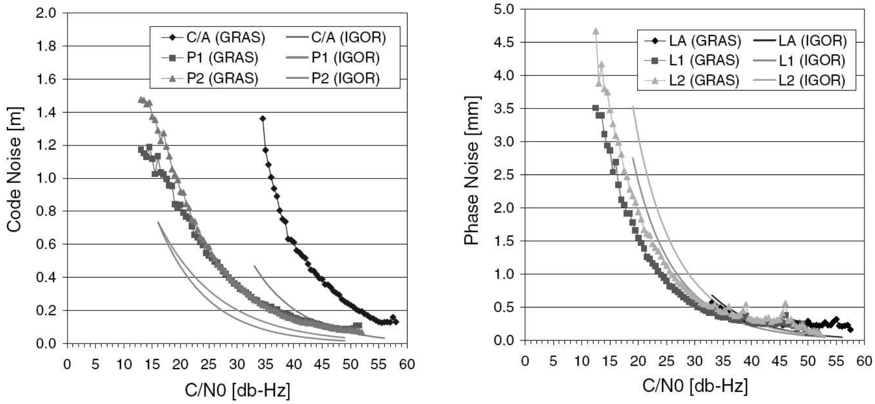

Figure 2.3 Code (left) and carrier phase (right) noise as function of the carrier to noise density ratio (C/N_0) of the GRAS and IGOR receivers [*Montenbruck et al.*, 2008*b*]

tracking losses grow linearly with decreasing signal strength, from about 12 dB at a C/A code C/N_0 value of 50 dB-Hz to 22 dB at 40 dB-Hz.

The pseudorange noise is assessed by forming the geometry and ionosphere-free multipath combination (2.19). The results are presented in Figure 2.3 (left) as a function of carrier to noise density ratio. As a comparison the values of the IGOR receiver are included in the figure [*Montenbruck et al.*, 2008*b*]. The C/A code noise is a bit smaller than the P1 and P2 code noise. P1 and P2 code noise are almost identical, only at the low C/N_0 range the P1 code noise is smaller. The noise values of the GRAS receiver are up to two times higher than the values of the IGOR receiver, which can be attributed to the more conservative tracking loop settings of the GRAS instrument.

At the right side of Figure 2.3 the phase noise is plotted with respect to the carrier to noise density ratio. The phase noise is retrieved from the scatter of 3 Hz raw measurement samples relative to a fourth order Savitzky-Golay smoothing polynomial [*Press et al.*, 1992] over a sliding 7 s interval. For the LA phase observations this results in noise values ranging from 0.2 to 0.5 mm, for the L1 and L2 phase the noise varies between 0.1 mm and 5 mm, where the L1 noise is smaller from a C/N0 value of 35 dBHz and below.

The combined effect of P1 and P2 code-multipath on the ionosphere-free combination is illustrated in Figure 2.4 (left). There is no evidence of cross-talk between the occultation and navigation antenna. In addition to the static multipath component, occasional strong reflections with C/N_0 variations up to 5 dB and multipath amplitudes up to 2 m were identified, an example of which is presented in Figure

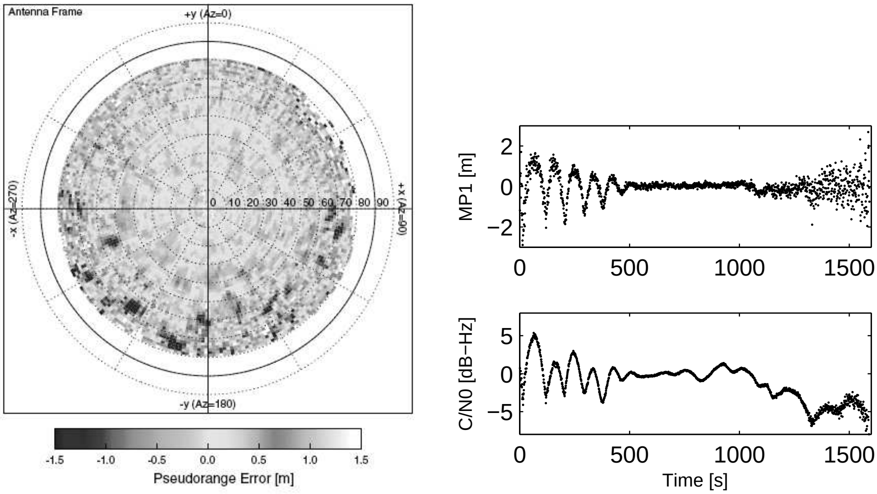

Figure 2.4 left: Multipath-map for the ionosphere-free P1/P2 pseudorange combination of the GRAS receiver, right: Multipath of the P1 code measurements of GRAS and associated C/N_0 in the course of a strong reflection event of PRN 6 (day 361/2006, 2:02 to 2:30 UTC). C/N_0 values have been detrended to remove the nominal elevation dependence.

2.4 (right). These do not show up in the average multipath map and are apparently dependent on the solar panel orientation.

Overall, the results confirm the high quality of the GRAS receiver which is comparable to the BlackJack/IGOR receiver. It shows a very similar sensitivity, where differences in measurement noise can be attributed to different tracking loop settings employed.

2.4.3 Lagrange receiver on board of GOCE

Because the orbit determination in this research is done solely with GPS observations, it is important to asses the quality of a GPS receiver before using its measurements for POD, after launch and commissioning. Such an assessment gives information on the tracking behaviour and noise level of the measurements, and supports the values for editing criteria and measurement weights applied in the orbit determination. A first analysis of the measurements of the Lagrange GPS receiver on board of the GOCE spacecraft indicates that the receiver meets its requirements. It is capable of tracking up to 12 satellites, which it does frequently, as is visible from Figure 2.5 showing the tracked GPS satellites during a typical day (DOY 201 in 2009). Around 95% of the time 10 or more satellites are tracked.

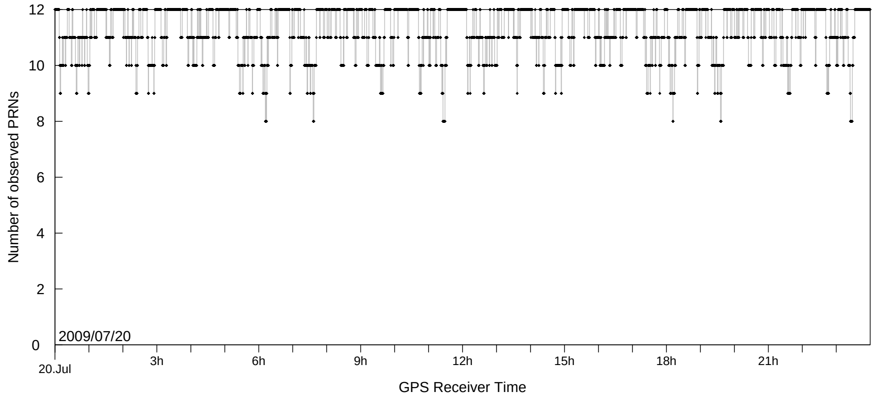

Figure 2.5 Number of satellites tracked by the GPS receiver on board of GOCE, DOY 201 of 2009

The noise level of the pseudorange observations is assessed by inspecting the residuals of the multipath combination (2.18). The residuals are grouped in carrier-to-noise density ratio (C/N_0) bins and the Root-Mean-Square (RMS) value of each bin is plotted in a graph. The result of a representative 3-day analysis is given in Figure 2.6. Comparing this plot with Figure 2.2 with the CHAMP and GRACE code noise and Figure 2.3 reveals some differences. The C/A code has the same noise characteristics as the GRAS receiver (and different from the BlackJack), while for the Lagrange receiver the P1 code has the same noise characteristics as the C/A code. The overall noise level of the code observations is also at least twice as high compared to the BlackJack code noise. It has to be noted that the GOCE GPS observations are delivered at 1 Hz, whereas the BlackJack RINEX files have preprocessed measurements at a rate of 0.1 Hz, obtained by fitting a polynomial through 1 Hz data points. The Lagrange receiver does not provide an independent L1 phase measurement, so the noise of the LA phase observation cannot be assessed by forming the L1-LA combination (2.25). An upper limit of the the phase noise of the ionospheric phase combination is obtained by inspecting the residuals of a reduced dynamic orbit determination, which fluctuate around 7.2 mm (for the period of DOY 20-29 in 2010), thus a noise level below 2.4 mm.

The clock offset of the Lagrange receiver drifts over time and can reach large values. This is illustrated in Figure 2.7, where daily mean clock offsets are plotted for a 10-day period, displaying a clear drift of about 0.3 ms/day.

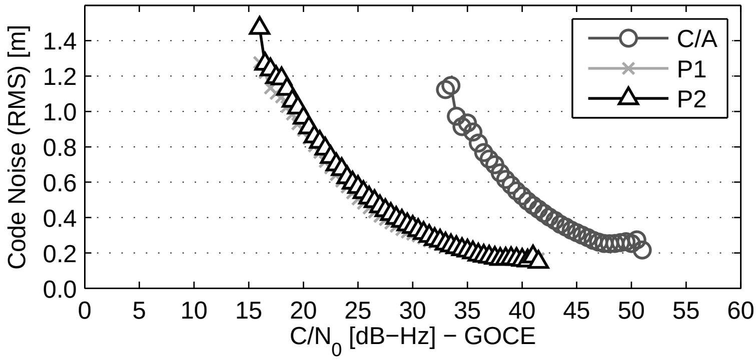

Figure 2.6 GOCE GPS receiver code noise, DOY 201-203 of 2009

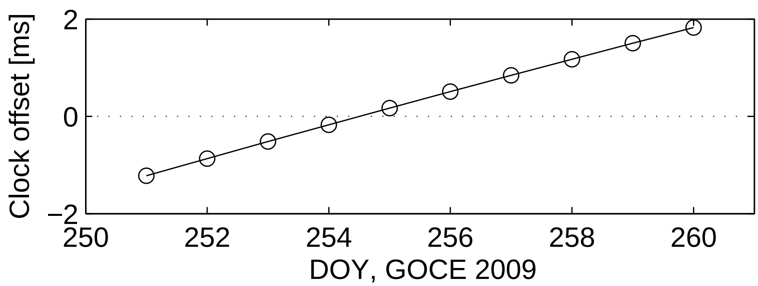

Figure 2.7 GOCE GPS receiver clock offset, DOY 251-260 of 2009

Chapter 3

Forces acting on a LEO satellite

Orbit determination of a satellite, from here on referring to an engineered vehicle, involves the propagation of the spacecraft's state, its position and velocity, from one epoch to the next by integrating the equation of motion, describing the accelerations experienced by the satellite. These accelerations are calculated from force models, which are inevitably an approximation of the real world. The different forces acting on a satellite orbiting the Earth are discussed in the first two sections of this chapter, divided in gravitational and non-gravitational forces, with a description of the modeling in the GHOST software, which is used throughout this dissertation, and in other software used for some analysis. The discussion of the different forces follows the standard literature on satellite orbit determination like [*Montenbruck and Gill*, 2000] and [*Tapley et al.*, 2004*a*].

An accelerometer placed in the center of mass of a satellite measures the non-gravitational forces acting on it. It's working principle and performance on board of CHAMP and GRACE are described in section 3.3. When applying the accelerometer data in precise orbit determination, the non-gravitational force models are replaced by the accelerometer measurements.

3.1 Gravitational forces

3.1.1 Gravity field of the Earth

The largest force acting on an Earth orbiting satellite is the gravitational force of the Earth. Because the mass of the Earth is not homogeneously distributed over the planet and the Earth itself is not a perfect sphere, the gravity field is described by the gravity potential U which results from summing up the contributions of individual mass elements $dm = \rho(\boldsymbol{s})d^3\boldsymbol{s}$ according to:

$$U = G \int \frac{\rho(\boldsymbol{s})d^3\boldsymbol{s}}{|\boldsymbol{r} - \boldsymbol{s}|} \tag{3.1}$$

Here G is the gravitational constant, $\boldsymbol{s}$ is the position of a point inside the Earth, $\rho(\boldsymbol{s})$ the density at that point and $\boldsymbol{r}$ the position of the satellite. The acceleration on an object due to the Earth's gravity field is given by the gradient of the potential:

$$\ddot{\boldsymbol{r}} = \nabla U \tag{3.2}$$

In order to evaluate the integral in (3.1) the inverse of the distance $|\boldsymbol{r} - \boldsymbol{s}|$ is expanded in series of Legendre polynomials. This leads to the expansion of the Earth's gravity potential into spherical harmonics:

$$U = \frac{GM_\oplus}{r} \sum_{n=0}^{\infty} \sum_{m=0}^{n} \frac{R_\oplus^n}{r^n} \bar{P}_{nm}(\sin(\phi))(\bar{C}_{nm} cos(m\lambda) + \bar{S}_{nm}\sin(m\lambda)) \tag{3.3}$$

Here $M_\oplus$ represents the Earth's mass and $R_\oplus$ the Earth's mean equatorial radius. The distance of the satellite to the Earth's center is given by r, the longitude by λ and the geocentric latitude by ϕ. $\bar{P}_{nm}$ stands for a normalized Legendre polynomial of degree n and order m. The normalized geopotential coefficients $\bar{C}_{nm}$ and $\bar{S}_{nm}$ in (3.3) describe the dependence of the gravity field on the Earth's internal mass distribution. Because the mass distribution is not known, these coefficients have to be determined indirectly from measurements like satellite tracking (observing the perturbations in satellite orbits), surface gravimetry (measuring the local gravitational acceleration) and altimeter data (relation between the mean sea surface and the equipotential surface). When the geopotential coefficients have been determined they are combined in a gravity field model.

The nominal gravity field model used throughout this dissertation is the GRACE Earth Gravity Model 02 (GGM02S), based on GRACE satellite data and computed by the Center for Space Research (CSR), Austin [*UT/CSR*, 2004]. When other gravity field models are applied, this is explicitly mentioned. The higher the considered degree n and order m, the more precise the model in general is. The accelerations on the satellite, equal to the gradient of U (3.3), are calculated directly by recurrence relations derived in [*Cunningham*, 1970].

3.1.2 Third body attractions

An Earth orbiting satellite is not only attracted by the Earth, but also by the other celestial bodies. Only the gravitational forces of the Sun and the Moon are considered, as the influence of other planets is much smaller and can be neglected. The perturbing acceleration of the Sun or the Moon on the satellite is given by the following relation of the third body induced acceleration:

$$\ddot{\boldsymbol{r}} = GM \left(\frac{\boldsymbol{s} - \boldsymbol{r}}{|\boldsymbol{s} - \boldsymbol{r}|^3} - \frac{\boldsymbol{s}}{|\boldsymbol{s}|^3} \right) \tag{3.4}$$

Here M is the mass of the perturbing body, $\boldsymbol{r}$ denotes the geocentric position of the satellite and $\boldsymbol{s}$ the geocentric position of the perturbing body. The first term in (3.4) is known as the direct effect, while the last term is referred to as the indirect effect, which is independent on the satellite (2^{nd} body) position and accounts for the inertial acceleration of the geocenter due to the third body, as (3.4) describes the motion with respect to the Earth's center of mass. The positions of the Sun and the Moon are calculated using analytical series expansions of luni-solar ephemerides [*Chapront-Touze and Chapront*, 1988], [*Francou et al.*, 1983] .

3.1.3 Tides

The gravitational force of the Sun and the Moon is also acting on the Earth itself, leading to a time-varying deformation of the Earth. The small periodic deformations of the solid body of the Earth are called solid Earth tides, while ocean tides describe the response of the oceans to the lunisolar attraction. As a consequence the Earth's gravity field shows small periodic variations, which affect the motion of a satellite. Both tides are modeled by an expansion of the tidal-induced gravity potential using spherical harmonics, similar to the expansion of the static gravity field of the Earth as described above. This leads to time-dependent corrections to the geopotential coefficients: $\Delta\bar{C}_{nm}$ and $\Delta\bar{S}_{nm}$, see equation (3.3). The practical computation of the solid Earth tides follows the IERS 2003 conventions [*McCarthy and Petit*, 2003] and a CSR ocean tide model based on TOPEX data is used [*UT/CSR*, 2006].

3.1.4 Overview of modeled gravitational accelerations

As a means to illustrate the magnitude of the gravitational forces, the accelerations acting on GRACE B are depicted in Figure 3.1 and 3.2 for two orbital revolutions in the RTN frame, with axes in the Radial direction, the associated perpendicular (almost Tangential) direction in the instantaneous orbital plane and the cross-track or Normal direction. The Earth's gravity has the largest effect in radial direction, where the satellite experiences a near constant attraction. The effect in tangential direction is three orders of magnitude smaller, and has a dominant twice per revolution period, the effect in normal direction is a magnitude smaller and has a dominant once per revolution period. The attraction of the Sun and Moon has a magnitude which is similar in radial and tangential direction, and a twice per revolution signature. In cross-track direction, a once per revolution period is observed, and the Moon has a ten times larger effect than the Sun. The solid Earth tides (Figure 3.2, top) have the largest effect in radial direction, and are two times smaller in the other directions. Again, in cross-track direction the period is once per revolution. Ocean tides have the most irregular pattern of all gravitational tides, were no dominant period is clearly visible. The ocean tide model presents

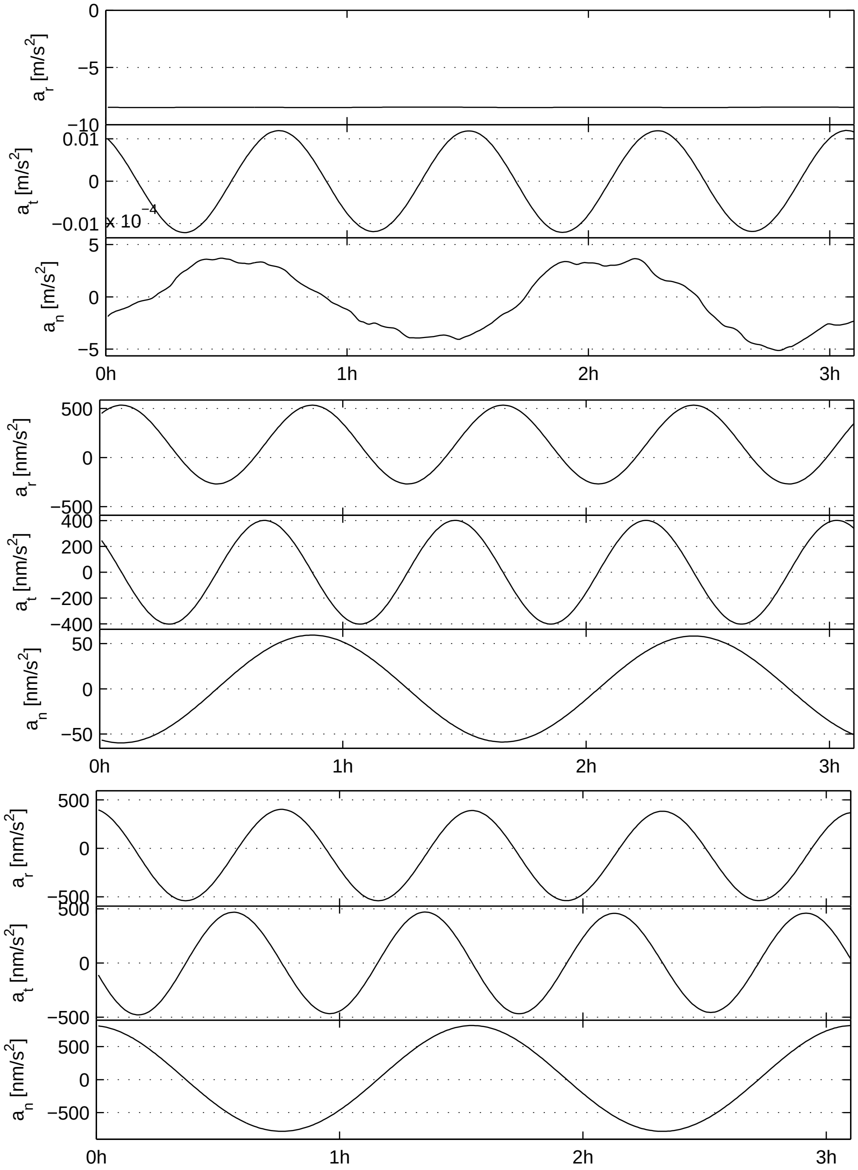

Figure 3.1 Earth gravitational acceleration (up), attraction of Sun (mid) and Moon (down) acting on GRACE B, DOY 103 in 2005, first 2 revolutions (note the difference in scale and units)

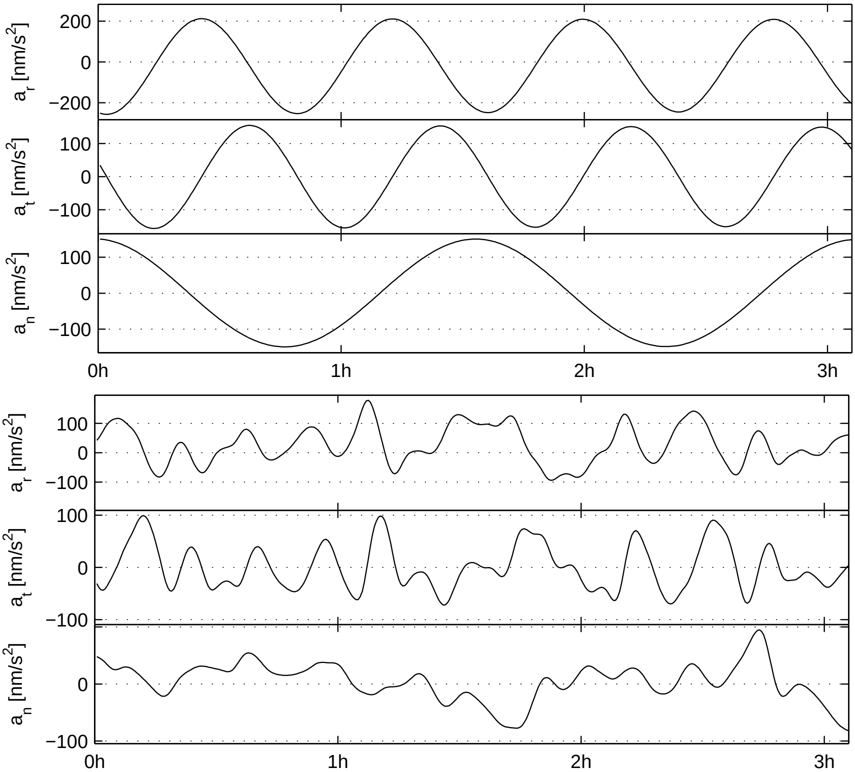

Figure 3.2 Solid Earth (up) and ocean tidal (down) acceleration acting on GRACE B, DOY 103 in 2005, first 2 revolutions

furthermore the biggest uncertainty of all gravitational forces (O. Montenbruck, priv. comm., 2008).

3.2 Non-gravitational forces

3.2.1 Atmospheric drag

The largest non-gravitational forces acting on a LEO satellite are atmospheric forces for altitudes below about 800 km. Accurate modeling of them is difficult because the physical properties and the concentration of the constituents of the atmosphere are not known very accurately, the interaction of neutral and charged particles with the satellite (surface) is complex and the attitude of the satellite with respect to the particle flux has to be taken into account and known precisely. For

LEO satellites charged particle drag can be neglected, a rigorous description of this type of drag can be found in [*Andrés*, 2007]. In GHOST, the atmospheric force is assumed to consist of drag solely, acting opposite to the velocity of the satellite with respect to the atmosphere, $\boldsymbol{v}_r$ (thus neglecting lift or binormal forces). The acceleration due to atmospheric drag is calculated with the following formula from aerodynamic theory, with A the satellite's cross sectional area, m the mass, $\boldsymbol{e}_v$ the unit vector of the velocity relative to the atmosphere, C_D the drag coefficient and ρ the atmospheric density at the location of the satellite:

$$\ddot{\boldsymbol{r}} = -\frac{1}{2} C_D \frac{A}{m} \rho v_r^2 \boldsymbol{e}_v \tag{3.5}$$

For the calculation of the relative velocity $\boldsymbol{v}_r$ the assumption is made that the atmosphere co-rotates with the Earth. This leads to:

$$\boldsymbol{v}_r = \boldsymbol{v} - \boldsymbol{\omega}_\oplus \times \boldsymbol{r} \tag{3.6}$$

with $\boldsymbol{v}$ the inertial velocity vector of the satellite, $\boldsymbol{r}$ the position vector and $\boldsymbol{\omega}_\oplus$ the Earth's angular velocity.

The two main difficulties associated with evaluating (3.5) are the determination of the exact values for the drag coefficient C_D and the upper atmosphere density ρ. The drag coefficient describes the interaction of the atmosphere's components with the satellite's surface and is not well known a priori because of the complex dependence on the satellite's surface material, the chemical constituents of the atmosphere, etc. Therefore this coefficient is estimated during the orbit determination process. Another bottleneck is the calculation of the density of the upper atmosphere, which depends in a complex way on a variety of parameters like altitude, distribution of the chemical constituents, temperature and solar and geomagnetic activity. Furthermore the temporal evolution of density and temperature of the neutral atmosphere depends on the 11 year solar cycle, the geomagnetic activity, local solar time and latitude variations and the semi-annual cycle. Luckily there exist relatively simple atmospheric models that provide a reasonable density prediction based on the just listed dependences [*Montenbruck and Gill*, 2000]. The Jacchia 1971 model has been implemented in the GHOST software. This model [*Jacchia*, 1971] is based upon the geodetic height and temperature and includes density variations as a function of time. The computation of the atmospheric densities is done in three steps. First the exospheric temperature T_∞ is computed from data on solar activity ($F_{10.7}$) and the geomagnetic index (K_p) and a model of the diurnal variation. When T_∞ is known the standard density is computed using coefficients of a bi-polynomial approximation of the Jacchia 1971 standard density model [*Gill*, 1996]. Finally time-dependent corrections are applied.

To illustrate, the drag acceleration calculated by the GHOST software on GRACE B for two orbital revolutions is plotted in the upper part of Figure 3.3. The biggest effect is in tangential direction, not surprising as drag is working opposite the satellite's (relative) velocity. The acceleration in radial direction is negligible, and in cross-track direction the magnitude is about 20 times smaller. A once per revolution signature is present in all directions.

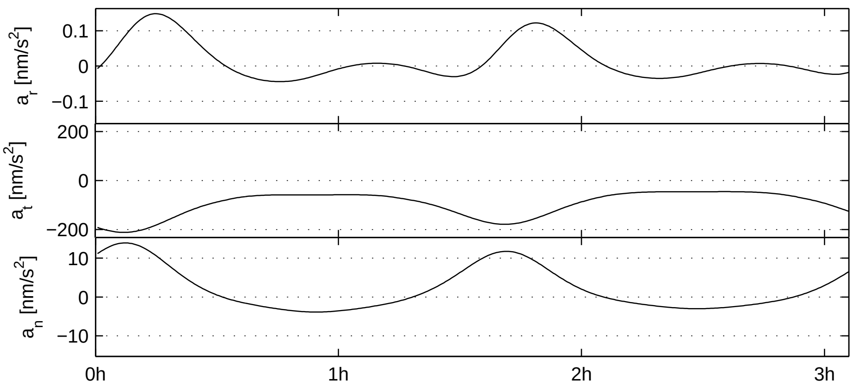

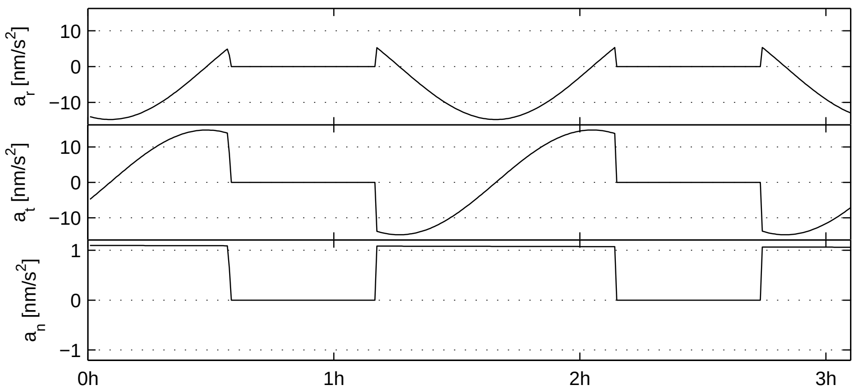

Figure 3.3 Modeled atmospheric drag (up) and direct solar radiation pressure (down) acting on GRACE B, DOY 103 in 2005, first 2 revolutions

3.2.2 Solar radiation pressure

A satellite exposed to radiation from the Sun experiences a small force arising from the absorption and reflection of emitted photons. This force is modeled by:

$$\ddot{\boldsymbol{r}} = \nu\, C_R P_\odot \frac{A}{m} AU^2 \frac{\boldsymbol{r} - \boldsymbol{r}_\odot}{|\boldsymbol{r} - \boldsymbol{r}_\odot|^3} \tag{3.7}$$

with A the cross sectional surface of the satellite perpendicular to the incoming radiation. C_R is the solar radiation pressure coefficient accounting for the reflectivity and absorption properties of the satellite and this parameter is estimated in the orbit determination. $P_\odot$ is the solar radiation pressure in the vicinity of the Earth, at 1 AU (Astronomical Unit), with a flux (pressure times speed of light) amounting to 1367 Wm^{-2}. $\boldsymbol{r}_\odot$ is the geocentric position vector of the Sun and m is the mass of the satellite. The shadow function ν is a value between 0 (in shadow) and 1 (fully illuminated), calculated with a shadow model with umbra and penumbra cones, ignoring atmosphere and flattening of the Earth.

The bottom part of Figure 3.3 presents the solar radiation pressure during the specific period already mentioned above. This force especially depends on the orientation of the orbital plane with respect to the Sun, influencing the occurrence of eclipses.

3.2.3 Earth radiation pressure

Besides the Sun, also the Earth emits radiation, which can be distinguished in optical and infrared radiation. The first is referred to as albedo radiation and is produced by reflection and scattering of solar radiation on the Earth's surface. The amplitude of the albedo acceleration for LEO satellites is around 10% to 35% [*Knocke et al.*, 1988] of the acceleration due to direct solar radiation, depending amongst others on cloud coverage and Earth surface characteristics. Typically an average albedo radiation of 460 Wm^{-2} is assumed. The second type is infrared radiation and consists of the reemission of the direct solar radiation absorbed by the Earth and its atmosphere. The effective radiation of this infrared emission of Earth surface elements is around 230 Wm^{-2}. As emitted by the Earth, both types of radiation result in (mainly) a radial acceleration on a LEO satellite. Because these forces results in small accelerations, neither effects are modeled in the GHOST software. The consequences of this are discussed in section 5.4.

3.2.4 Advanced modeling of non-gravitational forces

As the non-gravitational forces in the GHOST software are relatively simply modeled, or some not at all, more advanced external models are applied to analyze the accelerometer accelerations. In the orbit determination, the force modeling does not need to be perfect, as typically empirical accelerations are estimated which account for force model deficiencies, which is described in more detail in the next chapter. When the accelerometer data on the other hand are used to retrieve thermosphere density and winds, accurate models of the non-gravitational forces and the satellite itself are required. The models described here briefly are applied for that purpose and are also used in this dissertation for pre-processing and analysis of the accelerometer data.

The satellites are modeled with the so-called panel-method according to the satellite specifications in [*Bettadpur*, 2007]. The aerodynamic forces are modeled following Sentman [*Sentman*, 1961], with thermospheric densities from NRLMSISE-00 [*Picone et al.*, 2002] and winds from HWM-93 [*Hedin et al.*, 1996]. Eclipse transi-

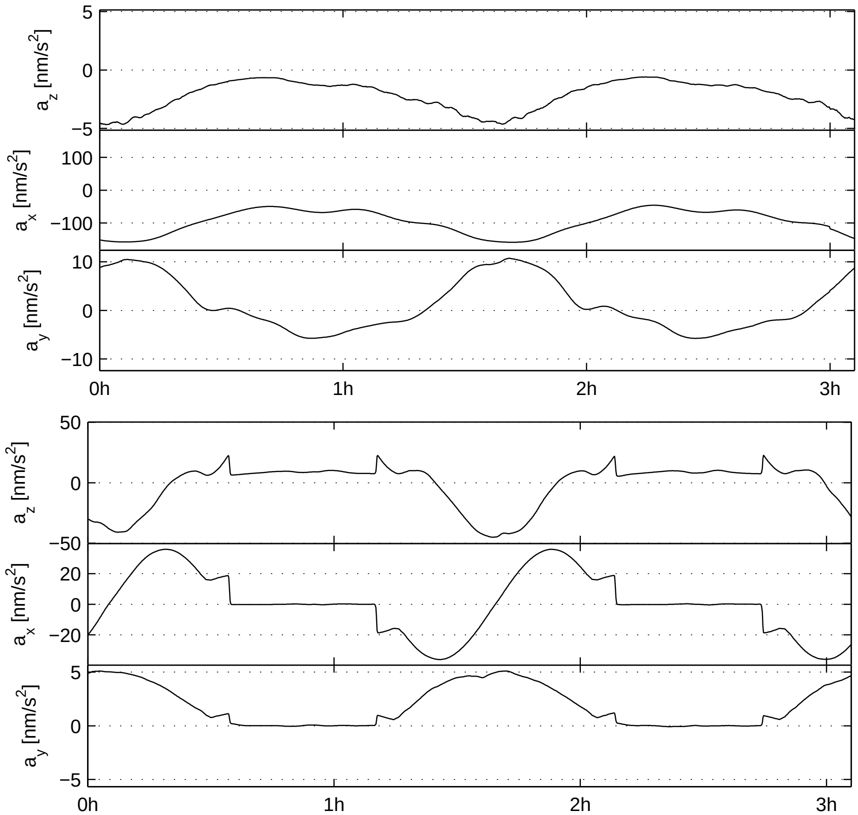

Figure 3.4 Advanced modeled atmospheric drag (up) and direct solar radiation pressure (down) acting on GRACE B, DOY 103 in 2005, first 2 revolutions

tions and the variable Earth albedo and infrared radiation are computed with the ANGARA software [*Fritsche et al.*, 1998].

The aerodynamic accelerations on GRACE B modeled as described above are plotted in the upper part of Figure 3.4, the radiation pressure accelerations in the bottom part, here in the Science Reference Frame (SRF), which agrees closely with the RTN frame for the GRACE spacecraft. Comparing these with the GHOST modeled non-gravitational accelerations in Figure 3.3 reveals that for the aerodynamic accelerations in radial direction a difference is visible. The radiation pressure acceleration is largely underestimated in the GHOST software, by a factor five in radial and cross-track direction, and two times in along-track direction, which can be attributed to the simple canon ball model and cross-sectional area applied.

3.3 Accelerometer performance

The STAR and SuperSTAR instruments, developed by ONERA/CNES (France), are placed in the center of mass of respectively CHAMP and GRACE and are extremely sensitive capacitive accelerometers with a designed accuracy of the sensitive axis of up to 10^{-9} m/s^2/Hz$^{1/2}$ (STAR, X_{SBF}- and Y_{SBF}-axis) and 10^{-10} m/s^2/Hz$^{1/2}$ (SuperSTAR, X_{SBF}- and Z_{SBF}-axis), with the X_{SBF}-axis of the Spacecraft Body Frame (SBF) nominally pointing in the direction of the orbital velocity, the Z-axis pointing towards the Earth and the Y-axis completing a right-handed orthogonal frame. The operation of the accelerometer is based on the levitation of a charged proof mass in the center of an electrostatic cage. The proof mass is kept in the center of the cage by adjusting the voltages of 6 pairs of electrodes, which are proportional to the surface forces acting on the satellite and provide the linear and angular accelerations after transformation. In the instrument transfer functions, biases and scale factors are introduced which are sensitive to instrument operations (on/off, reboot, calibration tests, degradation) and the satellite environment (temperature, attitude, maneuvers, etc.) [*Perosanz et al.*, 2005]. This leads to the necessity to estimate calibration parameters for the accelerometer measurements.

The STAR accelerometer on CHAMP is subject to jumps or spikes of up to 10^{-8} m/s^2, which partly have been correlated with events on board the spacecraft, and partly remain unexplained [*Perosanz et al.*, 2003]. Furthermore one electrode showed an anomalous behavior, affecting the radial linear acceleration (and roll and pitch angular accelerations). Therefore the Level 1B data (1 Hz sampling) are preprocessed to correct the anomalous data by filtering, identifying and correcting outliers and smoothing. Also the intervals of thruster pulses are cut out [*Förste and Choi*, 2005]. This results in Level 2 data products with a 0.1 Hz sampling. These products are used throughout this dissertation.

The SuperSTAR accelerometers are behaving closely to the specifications, where recently a noise level of 10^{-10} m/s^2/Hz$^{1/2}$ was verified [*Flury et al.*, 2008] for frequencies above 30 mHz. For lower frequencies, the accelerometer noise is buried in the signal of the non-gravitational accelerations, and accuracy information may be gained from the analysis of relative accelerations between both GRACE spacecraft [*Frommknecht et al.*, 2006], which revealed a performance up to 3 to 10 times above specifications. The GRACE accelerometer measurements are provided as Level 1B data with a 1 Hz sampling and are obtained from Level 1A data by applying a low-pass filter and a time correction [*Wu et al.*, 2006]. Thruster firings, which occur frequently to maintain the satellite attitude and pointing requirements, are not eliminated. Spikes with amplitudes between 10 and 70 nm/s^2 are observed in the Level 1A data [*Flury et al.*, 2008] and are related to heater switching, where the exact explanation is not yet found, although deformation of small parts in the satellite are a likely cause. Other observed effects, labelled twangs, are short and strongly damped oscillations, possible related to vibrations in the multi layer insulation of the satellite. Because the latter two effects occur at high-frequencies, they are almost completely removed through the application of a low-pass filter [*Frommknecht*, 2007]. Thruster effects remain visible, as these represent an actual acceleration of the satellite, which is not disadvantageous when using the accelerometer measurements for POD purposes. The accelerometer is assumed to be perfectly located in the center of mass of the satellite (on the GRACE spacecraft this is accomplished by a trim mechanism). However, still small misalignments errors can be present. The magnitude of these errors is believed to be small [*Kim and Tapley*, 2002].

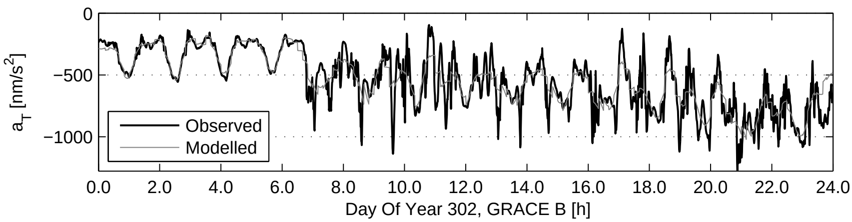

Figure 3.5 Comparison of observed and modeled non-gravitational accelerations on GRACE B in along-track direction for October 29, 2003 [*Van Helleputte and Visser*, 2008]

An interesting case to illustrate the accelerometer performance is the period of late October and early November 2003, when a series of violent solar eruptions took place with a broad impact on space weather [*Gopalswamy et al.*, 2005]. As the solar activity has a strong effect on the atmospheric drag acting on a spacecraft, these events are registered by the accelerometer. An example of the observed (corrected for the calibration parameters) and modeled accelerations on GRACE B in tangential direction during these days are presented in Figure 3.5 for October 29 in 2003. The modeled accelerations (GHOST) follow the same trend but cannot account for the high frequency fluctuations. This is clearly illustrated in Figure 3.6, where the frequency versus amplitude spectral density of the observed and modeled along-track accelerations is plotted for this day. In both cases a one revolution and half a revolution period is visible, whereas the accelerometer picks up the higher frequency part of the experienced accelerations in case of the strong solar events. For reference purposes, the same analysis is shown for a more quiet day. For both days the accelerometer signal is stronger for the half a revolution period, indicating that also for the low frequency part of the spectrum the accelerometer outperforms the model applied.

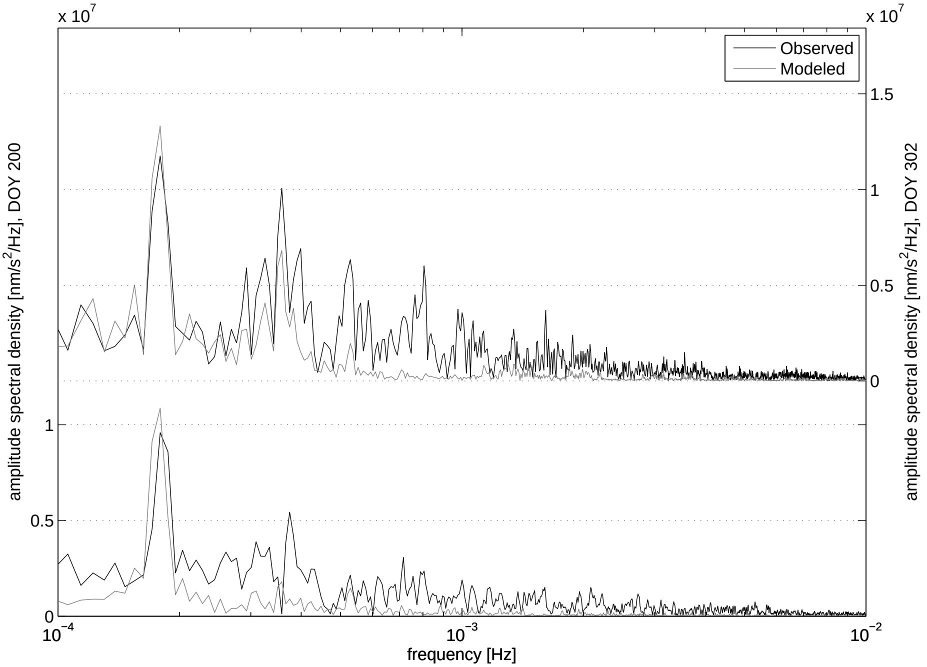

Figure 3.6 Spectral analysis of the observed and modeled along-track accelerations of GRACE B, for July 19 (DOY 200, bottom) and October 29 (DOY 302, top) 2003

Chapter 4

Precise orbit determination with accelerometer measurements

Many Earth observation missions have stringent requirements on the accuracy of the post-facto determined orbits in order to fulfill the scientific mission objectives, ranging from a few decimeters for past missions to the centimeter level for current and upcoming missions. Errors larger than the specified requirements affect the applications, e.g. the use of altimeter data for oceanography and glaciology, SAR interferometry, the recovery of the global Earth gravity field or spacecraft formation flying applications. Therefore these satellites are equipped with high-precision tracking systems like retro-reflectors for satellite laser ranging (SLR), DORIS or GPS receivers or a combination. In chapter 2 the benefits of GPS as precise tracking system was already highlighted and elaborated. In the sequel, only the use of GPS as tracking system will be considered, although SLR observations will be used to asses the quality of GPS-based orbit solutions. These solutions are based on undifferenced GPS observations with known GPS satellite clocks and ephemeris.

Precise orbit determination involves the computation of a spacecraft's position and velocity as accurately as possible based on tracking data. The three main techniques to determine the orbit of a satellite precisely are kinematic, dynamic and reduced dynamic orbit determination (OD).

Kinematic orbit determination [*Svehla and Rothacher*, 2003], also referred to as point positioning, is a geometric approach where each epoch the instantaneous position of the satellite is estimated directly from all the available observations, without considering any force on the LEO satellite or other trajectory information. The positions are generally determined by a least-squares or batch estimator, which tries to find the positions and observation model parameters (e.g. biases) for which the squared sum of the residuals between the actual and modeled observations is minimized. Each epoch the position components (Cartesian coordinates) and observation parameters (clocks, ambiguities, ...) are estimated. This method requires dense and continuous tracking providing a large number of geometrically well distributed observations, as the accuracy depends on the strength of the observing geometry. The quality further depends on the continuity and the precision of the observations, affected by systematic errors and data noise.

Dynamic orbit determination [*Schutz et al.*, 1994] relies on an accurate model of the forces acting on the satellite and the laws of motion, together referred to as the spacecraft dynamics. These models include force model parameters which are not exactly known like drag and solar radiation coefficients, density parameters, etc. The equations of motion are integrated from an initial state to the epoch of interest. The initial state together with the force model parameters have to be estimated using observations, mostly by a least-squares method. The residuals between the actual observations and the observations modeled on the integrated orbit are minimized in an iterative least-squares adjustment of the initial state, force model and observation parameters. This approach has a lower number of parameters to be estimated compared to the kinematic technique, which results in a decrease of the number of required observations. Dynamic orbit determination is the most traditional technique, already used in the first days of space exploration when only a sparse tracking network was available. The accuracy of the computed orbit depends heavily on the quality of the force models. Inaccurately modeled dynamics result in a solution with large systematic errors. In addition to the batch least squares method, the estimation of the different parameters can be carried out with a sequential estimator such as a Kalman filter. This approach allows a sequential update of the state information with each observation.

Because the kinematic orbit determination is highly sensitive to the continuously changing observation geometry and the quality of the observations, and in the dynamic approach any kind of mismodeling will be propagated along the orbit solution, the two techniques can be combined into *reduced dynamic* orbit determination [*Yunck et al.*, 1990]. In the reduced dynamic method a means to mitigate errors in the force models is implemented, by considering the satellite dynamics as the sum of the standard deterministic part (the applied force models) and a stochastic component [*Jäggi et al.*, 2006], the so-called empirical accelerations.

The reduced dynamic technique is used extensively for the research described in this thesis and is explained in detail in section 4.2 of this chapter. First, reference frame transformations applied in the orbit determination (OD) processing are described, allowing the connection of e.g. GPS ephemeris in an Earth fixed frame with orbit integration in an inertial frame. In section 4.3 the introduction of the accelerometer measurements in the OD is discussed, which are used instead of non-gravitational force models and allow for the calibration of the instrument by estimating scale factors and biases. In section 4.4 kinematic orbit determination is described, as this technique provides orbits independent of dynamic information which can be compared with the (reduced) dynamic ones to reveal systematic offsets and other differences. Finally, the implementation of all these techniques in the GHOST software and it's use for POD are discussed at the end of this chapter.

4.1 Reference frame transformations

In the orbit determination applications discussed in this chapter position, velocity and acceleration coordinates are expressed in different reference systems. First, the force models described in the previous chapter provide accelerations of the satellite in an inertial reference system, which is realized by the International Celestial Reference Frame (mean equator and equinox of J2000) [*McCarthy and Petit*, 2003]. The propagation of these accelerations results in a position and velocity vector in the ICRF. On the other hand, the coordinates of the GPS satellites in the IGS ephemerides file are given in an Earth-fixed, co-rotating reference system, the International Terrestrial Reference System, realized by the ITRF2005, the International Terrestrial Reference Frame (reference pole and Greenwich meridian). Therefore the GPS observations are modeled in the ITRF frame. As a consequence a transformation from ICRF coordinates to ITRF has to take place:

$$\boldsymbol{r}_{\mathrm{ITRF}} = \boldsymbol{U}_{\mathrm{ITRF}}^{\mathrm{ICRF}}(t)\, \boldsymbol{r}_{\mathrm{ICRF}} \tag{4.1}$$

Here the matrix $\boldsymbol{U}_{\mathrm{ITRF}}^{\mathrm{ICRF}}(t) = \boldsymbol{\Pi}(t)\boldsymbol{\Theta}(t)\boldsymbol{N}(t)\boldsymbol{P}(t)$ stands for the transformation matrix from ICRF to ITRF (reflecting IERS1996 standards [*McCarthy*, 1996]) and is built up from 4 rotation matrices describing coordinate changes due to precession $\boldsymbol{P}(t)$, nutation $\boldsymbol{N}(t)$, Earth rotation $\boldsymbol{\Theta}(t)$ and polar motion $\boldsymbol{\Pi}(t)$. A detailed description of these effects, the different reference systems in general and the derivation of the transformation matrices can be found in [*Montenbruck and Gill*, 2000]. The required input for these models, such as polar motion parameters or the UT1-UTC time offsets, are captured in the so called Earth rotation parameters, obtained from the IGS.

In the transformation of the velocity vector the rotation of the axis of the Earth-fixed reference frame has to be accounted for:

$$\boldsymbol{v}_{\mathrm{ITRF}} = \boldsymbol{U}_{\mathrm{ITRF}}^{\mathrm{ICRF}}(t)\, \boldsymbol{v}_{\mathrm{ICRF}} + \frac{d\boldsymbol{U}_{\mathrm{ITRF}}^{\mathrm{ICRF}}(t)}{dt} \boldsymbol{r}_{\mathrm{ICRF}} \tag{4.2}$$

The derivative of $\boldsymbol{U}(t)$ with respect to t is calculated using a second order symmetric difference quotient. The transformation from ITRF to ICRF is obtained by taking the transposed matrices of $\boldsymbol{U}(t)$ and the derivative matrix.

Another reference frame used frequently is the spacecraft body frame (SBF), which is defined in section 3.3 in the previous chapter. The 3×3 orthonormal matrix $\mathbf{C}(t)$ describes the transformation between coordinates in the spacecraft body frame

$\mathbf{r}_{\mathrm{SBF}}$ and in the ICRF as

$$\mathbf{r}_{\mathrm{ICRF}} = \mathbf{C}(t)\mathbf{r}_{\mathrm{SBF}} \tag{4.3}$$

This transformation matrix is constructed using precise spacecraft attitude data, which is obtained from star camera observations, and provided as quaternions. The exact definition of how the quaternions are handled for this research can be found in [*Montenbruck*, 2000]. When required, a transformation between the spacecraft body frame and the ITRF can now be simply handled by

$$\mathbf{r}_{\mathrm{ITRF}} = \mathbf{U}(t)\mathbf{C}(t)\mathbf{r}_{\mathrm{SBF}} \tag{4.4}$$

Because both $\mathbf{U}(t)$ and $\mathbf{C}(t)$ are orthonormal, their inverse, required for a transformation in the other direction, is simply given by their transpose and then the multiplication is reversed.

4.2 Reduced dynamic POD technique

Due to the limitations of both pure kinematic and pure dynamic orbit determination the concept of reduced dynamic orbit determination has been proposed and successfully demonstrated [*Wu et al.*, 1991] [*Yunck et al.*, 1990]. The first step in reduced-dynamic OD involves the propagation of the spacecraft's state from one epoch to the next by integrating the equations of motion. To this extent, the different forces acting on the satellite are modeled with respect to the variables they depend upon, which was described in the previous chapter. These models depend on several parameters which are estimated in the OD process. Due to the complexity and non-linearity of the models these parameters can hardly be solved directly from a given set of observations. Therefore the relation between the observables and the independent parameters is linearized and thus iteration is necessary. This requires a large number of partial derivatives, which are described in the next section. Next, the concept of empirical accelerations is introduced, followed in section 4.2.3 by the theory of batch least squares estimation and the specific set up of the normal equations in the GHOST software. At the end of this section the numerical integration method and the applied integrator are discussed.

4.2.1 Variational equations

In orbit determination, the prime parameter of interest is the satellite (initial) state vector

$$\mathbf{y}(t) = \begin{pmatrix} \mathbf{r}(t) \\ \mathbf{v}(t) \end{pmatrix} \tag{4.5}$$

consisting of its position $\mathbf{r}$ and velocity $\mathbf{v}$. This state vector is propagated over time to the observation epochs by means of numerical integration of the equation of motion, converted to a first order differential equation

$$\frac{d}{dt}\mathbf{y}(t) = \mathbf{f}(t, \mathbf{y}(t), \mathbf{p}) = \begin{pmatrix} \mathbf{v}(t) \\ \mathbf{a}(t, \mathbf{r}, \mathbf{v}, \mathbf{p}) \end{pmatrix} \tag{4.6}$$

The gravitational and non-gravitational dynamic force models are used to compute the accelerations $\mathbf{a}(t, \mathbf{r}, \mathbf{v}, \mathbf{p})$ acting on the spacecraft, which depend on the time t, position and velocity of the spacecraft as well as on force model parameters $\mathbf{p}$. Since $\mathbf{y}(t_0)$, the initial state vector at t_0, and the selected force model parameters are actually being estimated as part of the orbit determination process, the partial derivatives of the satellite state at an arbitrary time t with respect to these estimation parameters are required and the computation of these partial derivatives also requires the use of the dynamic force models. These dependencies are described below, following [*Montenbruck and Gill*, 2000].

In space-flight dynamics the state transition matrix $\mathbf{\Phi}(t, t_0)$ describes the first-order dependence of the state vector $\boldsymbol{y}$ at epoch t on the initial values at t_0:

$$\mathbf{\Phi}(t, t_0) = \frac{\partial \mathbf{y}(t)}{\partial \mathbf{y}(t_0)} \tag{4.7}$$

which is 6×6 dimensional and can be obtained by differentiating equation (4.6) to the initial state:

$$\frac{\partial}{\partial \mathbf{y}(t_0)} \frac{d}{dt}\mathbf{y}(t) = \frac{\partial \mathbf{f}(t, \mathbf{y}(t), \mathbf{p})}{\partial \mathbf{y}(t_0)} = \frac{\partial \mathbf{f}(t, \mathbf{y}(t), \mathbf{p})}{\partial \mathbf{y}(t)} \cdot \frac{\partial \mathbf{y}(t)}{\partial \mathbf{y}(t_0)} \tag{4.8}$$

This last equation can be rewritten to

$$\frac{d}{dt}\mathbf{\Phi}(t, t_0) = \frac{\partial \mathbf{f}(t, \mathbf{y}(t), \mathbf{p})}{\partial \mathbf{y}(t)} \cdot \mathbf{\Phi}(t, t_0) \tag{4.9}$$

or more specifically, by substituting the state vector:

$$\frac{d}{dt}\mathbf{\Phi}(t, t_0) = \begin{pmatrix} \mathbf{0}_{3\times3} & \mathbf{1}_{3\times3} \\ \frac{\partial \mathbf{a}(t, \mathbf{r}, \mathbf{v}, \mathbf{p})}{\partial \mathbf{r}(t)} & \frac{\partial \mathbf{a}(t, \mathbf{r}, \mathbf{v}, \mathbf{p})}{\partial \mathbf{v}(t)} \end{pmatrix}_{6\times6} \cdot \mathbf{\Phi}(t, t_0) \tag{4.10}$$

which is a first order differential equation with the identity matrix as the initial value, $\mathbf{\Phi}(t_0, t_0) = \mathbf{1}_{6\times6}$.

In a similar way the partials of the state vector with respect to the force model parameters are captured in the $6 \times n_p$ dimensional sensitivity matrix, with n_p the number of estimated force model parameters:

$$\mathbf{S}(t) = \frac{\partial \mathbf{y}(t)}{\partial \mathbf{p}} \tag{4.11}$$

When differentiating equation (4.6) to the force model parameters,

$$\frac{d}{dt}\frac{\partial \mathbf{y}(t)}{\partial \mathbf{p}} = \frac{\partial \mathbf{f}(t,\mathbf{y}(t),\mathbf{p})}{\partial \mathbf{y}(t)} \cdot \frac{\partial \mathbf{y}(t)}{\partial \mathbf{p}} + \frac{\partial \mathbf{f}(t,\mathbf{y}(t),\mathbf{p})}{\partial \mathbf{p}} \tag{4.12}$$

a first order differential equation is again obtained:

$$\begin{aligned} &\frac{d}{dt}\mathbf{S}(t)_{6\times n_p} = \\ &\begin{pmatrix} \mathbf{0}_{3\times 3} & \mathbf{1}_{3\times 3} \\ \dfrac{\partial \mathbf{a}(t,\mathbf{r},\mathbf{v},\mathbf{p})}{\partial \mathbf{r}(t)} & \dfrac{\partial \mathbf{a}(t,\mathbf{r},\mathbf{v},\mathbf{p})}{\partial \mathbf{v}(t)} \end{pmatrix}_{6\times 6} \cdot \mathbf{S}(t) + \begin{pmatrix} \mathbf{0}_{3\times n_p} \\ \dfrac{\partial \mathbf{a}(t,\mathbf{r},\mathbf{v},\mathbf{p})}{\partial \mathbf{p}} \end{pmatrix}_{6\times n_p} \end{aligned} \tag{4.13}$$

Since the initial satellite state does not depend on any of the force model parameters the initial value of the sensitivity matrix yields $\mathbf{S}(t_0) = \mathbf{0}_{6\times n_p}$.

The derived expressions for both the state transition and sensitivity matrix can now be combined into the following first order differential equation, also referred to as the *variational equations*:

$$\frac{d}{dt}(\mathbf{\Phi},\mathbf{S}) = \begin{pmatrix} \mathbf{0}_{3\times 3} & \mathbf{1}_{3\times 3} \\ \dfrac{\partial \mathbf{a}}{\partial \mathbf{r}} & \dfrac{\partial \mathbf{a}}{\partial \mathbf{v}} \end{pmatrix}_{6\times 6} \cdot (\mathbf{\Phi},\mathbf{S}) + \begin{pmatrix} \mathbf{0}_{3\times 6} & \mathbf{0}_{3\times n_p} \\ \mathbf{0}_{3\times 6} & \dfrac{\partial \mathbf{a}}{\partial \mathbf{p}} \end{pmatrix}_{6\times(6+n_p)} \tag{4.14}$$

These equations are integrated simultaneously with the state vector, because the position and velocity of the satellite are required to evaluate $\left(\frac{\partial \boldsymbol{a}}{\partial \boldsymbol{r}}\right)$ and $\left(\frac{\partial \boldsymbol{a}}{\partial \boldsymbol{v}}\right)$ in (4.14). By computing the partial derivatives along with the acceleration itself using common subexpressions, the computing effort is reduced considerably. Furthermore, in solving the variational equations some simplifications can be made in the force modeling without losing much accuracy of the state transition and sensitivity matrix.

For solving the variational equations, in the GHOST software the gravitational force is simplified to the central and J_2 terms of the gravitational potential only, and the attraction of the Sun and Moon and tides is further neglected. Because in the simultaneous integration of the state vector and the variational equations for solving equation (4.14) consistent models have to be used [*May*, 1980], the equation of motion is once integrated with the full force model and once along with the variational equations using the simplified force model just described. For the computation of the partial derivative of the acceleration with respect to the position $\partial \boldsymbol{a}/\partial \boldsymbol{r}$, only the gravitational attraction of the Earth is considered, as this derivative has a much larger magnitude compared to the derivative of other accelerations with respect to the position. A difference quotient approximation is used for it's computation, with Δd a position increment of e.g. 1 m:

$$\frac{\partial \boldsymbol{a}}{\partial x} = \frac{\boldsymbol{a}_{\text{grav}}(x,y,z) - \boldsymbol{a}_{\text{grav}}(x+\Delta d,y,z)}{\Delta d} \tag{4.15}$$

with a similar expression for the y and z component of the position vector. Approximation errors are eliminated due to the iterative nature of the POD process. The partial derivatives of the acceleration with respect to the velocity are neglected, $\frac{\partial \boldsymbol{a}}{\partial \boldsymbol{v}} = 0$. The partials with respect to the drag and solar radiation pressure coefficients, C_D and C_R, follow out of equations (3.5) and (3.7) by deriving these expressions with respect to the respective coefficients. The empirical accelerations, described in the next subsection, are defined in a RTN-frame, therefore the derivatives of the inertial acceleration with respect to these empirical accelerations are equal to the unit vectors of the RTN-frame:

$$\frac{\partial \boldsymbol{a}}{\partial \boldsymbol{a}_{\mathrm{emp}}} = (\boldsymbol{e}_{\mathrm{R}}, \boldsymbol{e}_{\mathrm{T}}, \boldsymbol{e}_{\mathrm{N}}) \tag{4.16}$$

4.2.2 Empirical accelerations

To compensate for any deficiencies in the employed dynamical models, empirical accelerations are considered, also referred to as pseudo-stochastic parameters. These are defined in the RTN frame and are estimated as part of the orbit determination process.

Following [*Bierman*, 1977], the theory of random processes with exponentially correlated (or 'colored') process noise provides a suitable mathematical framework for the description of these unmodeled accelerations. A first-order Gauss-Markov process $p(t)$ [*Brown and Hwang*, 1997] exhibits an exponential autocorrelation

$$R(\Delta t) = E\left[p(t)p(t+\Delta t)\right] = \sigma^2 \mathrm{e}^{-|\Delta t|/\tau} \tag{4.17}$$

where σ^2 denotes the steady-state variance of the process and τ is the correlation time scale. In a time-discrete form, the process satisfies the first-order difference equation

$$p(t_{i+1}) = m_i p(t_i) + w_i \tag{4.18}$$

with mapping factor

$$m_i = \mathrm{e}^{-|t_{i+1}-t_i|/\tau} \tag{4.19}$$

where the process noise w_i is an uncorrelated random sequence with zero mean and variance

$$E(w_i^2) = \sigma^2(1 - m_i^2) \tag{4.20}$$

In the GHOST software, for practical purposes the empirical accelerations are considered to be piecewise constant in pre-defined sub-intervals, which facilitates both the trajectory propagation and the overall parameter adjustment. Other parameterizations such as instantaneous velocity changes or piecewise linear and continuous accelerations are considered in [*Jäggi et al.*, 2006]. In case of a batch least-squares estimator, the entire data arc is divided into n intervals of equal duration τ and an independent set of empirical acceleration parameters (a_R, a_T, a_N) is estimated each interval. A priori information is used in the normal equations to constrain the individual parameters to a nominal value of zero with a predefined weight. The choice of an adequate interval length reflects a compromise between observability, computational effort and the capability to resolve time varying phenomena. Given an orbital period of roughly 6000 s for LEO satellites and a representative measurement interval of 30 s, intervals of 600 s duration have been found to be suitable [*Montenbruck et al.*, 2005*a*] and are adopted throughout this research. While shorter intervals provide a smoother variation of the estimated accelerations, no significant improvement of the overall orbit determination accuracy has been observed that would justify an associated increase in computation time. Longer intervals, in contrast, appeared insufficient to sample the characteristic time scales of dynamic force model errors.

In a sequential filter, as shown in [*Lichten*, 1990] and [*Van Helleputte*, 2004], the mapping factor (4.19) can be directly inserted into the state transition matrix and the process noise added to the propagated covariance matrix. In this approach, the choice of steady state variance and autocorrelation time determines the relative weighting between the dynamics and observations, hence the expression reduced dynamic OD.

4.2.3 Batch least-squares estimation

The least-squares OD technique comprises the iterative adjustment of dynamical trajectory and measurement model parameters from a set of observations. The spacecraft trajectory is integrated from a priori conditions across the entire data arc and residuals are formed as the difference between the observation and modeled measurements. Making use of the partial derivatives of the modeled observations with respect to the parameters of interest, corrections to the a priori parameters are obtained from the least-squares solution of an overdetermined linear set of equations. This is done in such a way that the squares of the measurement residuals are minimized. Aside from the following brief overview, the fundamental concept of weighted linearized least-squares is extensively covered in literature, such as [*Teunissen*, 2000] and [*Montenbruck and Gill*, 2000], where in the latter the problem is discussed in the context of satellite orbit adjustment. The brief overview here focusses on those aspects of relevance for GPS based orbit determination and follows the discussion in [*Kroes*, 2006].

When considering a linearization of the modeled GPS measurements $\mathbf{h}(\mathbf{y})$ around an initial value $\mathbf{y}_0$ of the estimation parameters $\mathbf{y}$, the least-squares update of this initial value is given by

$$\Delta\mathbf{y} = (\mathbf{H}^T\mathbf{W}\mathbf{H})^{-1}\mathbf{H}^T\mathbf{W}(\mathbf{z} - \mathbf{h}(\mathbf{y}_0)), \tag{4.21}$$

resulting in the updated estimation parameters $\mathbf{y}_0 + \Delta\mathbf{y}$. Here, $\mathbf{z}$ is the vector containing the actual GPS observations and $\mathbf{W} = \mathbf{Q}_{\mathbf{z}}^{-1}$ is the accompanying weighting matrix, given by the inverse of the covariance matrix, introduced in section 2.1.3. Furthermore, the design matrix $\mathbf{H} = (\partial\mathbf{h}(\mathbf{y}_0)/\partial\mathbf{y}_0)$ contains the linearized partial derivatives of the modeled measurements with respect to the estimation parameters. The part requiring inversion, $\mathbf{N} = \mathbf{H}^T\mathbf{W}\mathbf{H}$, is also referred to as the normal matrix. Non-linear estimation problems, such as GPS positioning applications, can be coped with by means of multiple iterations, where the updated estimation parameters are used as the initial values for the next iteration. The parameterization of the pseudorange and carrier phase observations is done according to the undifferenced ionosphere free GPS observation model (2.15), and the linearization from equation (2.22).

In the reduced dynamic OD technique implemented in GHOST, the estimation parameter vector comprises the following dynamic unknowns: the 6-dimensional initial spacecraft state vector $\mathbf{y}_0 = \mathbf{y}(t_0)$ at a reference epoch t_0, relating to the spacecraft center of mass expressed in the ICRF, a solar radiation pressure coefficient C_R that acts as an adjustable scaling factor for the surface reflectivity in the modeling of solar radiation pressure forces, a drag coefficient C_D that acts as an adjustable scaling factor in the modeling of drag forces and the empirical accelerations $\mathbf{a} = (a_R, a_T, a_N)$ in consecutive time intervals. Besides these, the GPS observation parameters added to the estimation vector are the receiver clock offset $c\delta t_r$ at each measurement epoch and an ionosphere free carrier phase ambiguity $b = \lambda_{\mathrm{IF}} A_{\mathrm{IF}}$ for each arc (or pass) of a continuously tracked GPS satellite.

These estimation parameters are grouped in separate vectors, which eases the formulation of the least-squares system. These contain the receiver clock offsets in the n_T-dimensional vector

$$\mathbf{T} = \left(c\delta t_0; \ldots; c\delta t_{n_T-1}\right) \tag{4.22}$$

the dynamic estimation parameters in the $n_Y = 8 + 3n_a$ dimensional vector concerning the satellite trajectory modeling

$$\mathbf{Y} = \left(\mathbf{y}_0; C_R; C_D; \mathbf{a}_0; \ldots; \mathbf{a}_{n_a-1}\right) \tag{4.23}$$

and the carrier phase biases in the n_B-dimensional vector

$$\mathbf{B} = \left(b_0; \ldots; b_{n_B-1}\right) \tag{4.24}$$

Considering a 24 hour data arc in which the measurements are processed in 30 second steps, this results in a total of 2880 clock offsets. Due to the fast changing viewing geometry for LEO spacecraft GPS satellites are observed for a maximum of about 40 minutes resulting in typically 15 (phase connected) passes with constant ambiguities for a single GPS satellite. Most of the time the total number of independent ambiguity parameters over 24 hours is approximately 450 to 500 for space-borne scenarios. In addition, when using 600 second intervals for the empirical accelerations this results in 432 dynamical estimation parameters. The total number of estimation parameters now becomes approximately 3800.

The GPS observation model is linearized around initial values of the estimation parameters $(\mathbf{T}_0, \mathbf{Y}_0, \mathbf{B}_0)$

$$\begin{aligned}\mathbf{T} &= \mathbf{T}_0 + \Delta\mathbf{T}\\ \mathbf{Y} &= \mathbf{Y}_0 + \Delta\mathbf{Y}\\ \mathbf{B} &= \mathbf{B}_0 + \Delta\mathbf{B}\end{aligned} \tag{4.25}$$

for which updates $(\Delta\mathbf{T};\Delta\mathbf{Y};\Delta\mathbf{B})$ are computed by solving the least-squares system.

The construction and solution of the least-squares problem is greatly simplified by the specific structure of the normal equations associated with the above division of estimation parameters:

$$\begin{aligned}&\left(\frac{\partial\mathbf{h}}{\partial(\mathbf{T}_0, \mathbf{Y}_0, \mathbf{B}_0)}\right)^T \mathbf{W} \left(\frac{\partial\mathbf{h}}{\partial(\mathbf{T}_0, \mathbf{Y}_0, \mathbf{B}_0)}\right) \begin{pmatrix}\Delta\mathbf{T}\\ \Delta\mathbf{Y}\\ \Delta\mathbf{B}\end{pmatrix}\\ &= \left(\frac{\partial\mathbf{h}}{\partial(\mathbf{T}_0, \mathbf{Y}_0, \mathbf{B}_0)}\right)^T \mathbf{W}\big(\mathbf{z} - \mathbf{h}(\mathbf{T}_0, \mathbf{Y}_0, \mathbf{B}_0)\big)\end{aligned} \tag{4.26}$$

These are used to compute the corrections $(\Delta\mathbf{T};\Delta\mathbf{Y};\Delta\mathbf{B})$ of a priori parameter values from the vector of modeled observations $\mathbf{h}(\mathbf{T}_0, \mathbf{Y}_0, \mathbf{B}_0)$, the vector of measurements $\mathbf{z}$ and the weighting matrix or the inverse of the measurement covariance, $\mathbf{W} = \mathbf{Q}_{\mathbf{z}}^{-1}$.

The overall design matrix

$$\left(\frac{\partial\mathbf{h}}{\partial(\mathbf{T}_0, \mathbf{Y}_0, \mathbf{B}_0)}\right) = \begin{pmatrix}\mathbf{H}_T & \mathbf{H}_Y & \mathbf{H}_B\end{pmatrix} \tag{4.27}$$

is constructed from the three partitioned ones and contains the partial derivatives of the modeled GPS observations $\mathbf{h}$ with respect to the estimation vector parameters. This results for the partials of the modeled GPS observation h^s of GPS satellite s with respect to the clock offset vector in

$$\frac{\partial h^s}{\partial\mathbf{T}} = \big(0_{(0)}, \ldots, 0_{(i-1)}, 1_{(i)}, 0_{(i+1)}, \ldots, 0_{(n_T-1)}\big) \tag{4.28}$$

which are only set for the epoch, t_i the measurement was taken. The same is true for the partials with respect to the carrier phase ambiguities. In this case only the partial of the concerning bias parameter of a carrier phase observation of a pass k is set

$$\frac{\partial h^s}{\partial\mathbf{B}} = \big(0_{(0)}, \ldots, 0_{(k-1)}, 1_{(k)}, 0_{(k+1)}, \ldots, 0_{(n_B-1)}\big) \tag{4.29}$$

For pseudorange observations these partials are always zero. Finally, the partials with respect to the dynamic estimation parameters refer to the point in the trajectory at which the measurement was taken:

$$\frac{\partial h^s}{\partial\mathbf{Y}} = \left(\frac{\partial h^s}{\partial\mathbf{y}_0}, \frac{\partial h^s}{\partial C_R}, \frac{\partial h^s}{\partial C_D}, \frac{\partial h^s}{\partial\mathbf{a}_0}, \cdots, \frac{\partial h^s}{\partial\mathbf{a}_{j-1}}, \frac{\partial h^s}{\partial\mathbf{a}_j}, \mathbf{0}^T_{(j+i)}, \cdots, \mathbf{0}^T_{(n_a-1)}\right) \tag{4.30}$$

meaning that if the measurement at epoch t_i falls within the j^{th} interval of empirical acceleration parameters, the partials up to this point are set accordingly. This follows from the physical explanation that the empirical accelerations in the past contributed to the trajectory shape in the present and the future. No fading characteristics as for e.g. a Gauss-Markov process have been applied. A more generic expression for this last set of partials is given by

$$\frac{\partial h^s}{\partial \mathbf{Y}} = \begin{pmatrix} \frac{\partial h^s}{\partial \mathbf{y}_0} & \frac{\partial h^s}{\partial \mathbf{p}} \end{pmatrix} \tag{4.31}$$

where the dynamic estimation parameters are divided into the initial state vector and the estimated force model parameters, $\mathbf{p} = (C_R; C_D; \mathbf{a}_0; \ldots; \mathbf{a}_j; \ldots; \mathbf{a}_n)$. In addition, the partials of the measurement with respect to the current satellite state are given by

$$\frac{\partial h^s}{\partial \mathbf{y}_i} = \begin{pmatrix} -(\mathbf{U}^T(t_i)\mathbf{e}^s(t_i))^T & \mathbf{0}_{1\times 3} \end{pmatrix} \tag{4.32}$$

where the line of sight vector $\mathbf{e}^s(t_i)$ from equation (2.23) is transformed to the inertial reference frame using the transformation matrix $\mathbf{U}(t_i)$ described in section 4.1. Combining the last two equations leads to an expression for the partials with respect to the dynamic estimation parameters, introducing the state transition and sensitivity matrix:

$$\frac{\partial h^s}{\partial \mathbf{Y}} = \begin{pmatrix} \frac{\partial h^s}{\partial \mathbf{y}_i}\frac{\partial \mathbf{y}_i}{\partial \mathbf{y}_0} & \frac{\partial h^s}{\partial \mathbf{y}_i}\frac{\partial \mathbf{y}_i}{\partial \mathbf{p}_i} \end{pmatrix} = \begin{pmatrix} \frac{\partial h^s_i}{\partial \mathbf{y}_i}\mathbf{\Phi}(t_i, t_0) & \frac{\partial h^s}{\partial \mathbf{y}_i}\mathbf{S}(t_i) \end{pmatrix} \tag{4.33}$$

In practice the construction of these partials and the accompanying measurement residual, $z - h(c\delta t_r(t_i), \mathbf{y}(t_i), b_k)$, are not so trivial anymore, since they require the numerical integration of the spacecraft trajectory along with the variational equations. The integration over the entire batch of observation data, with a restart at every new interval of empirical accelerations, is accomplished using the variable order variable step-size multi-step numerical integration method DE [*Shampine and Gordon*, 1975], which is described in more detail in the next subsection. Furthermore, it must be noted that the modeling of the GPS observations is done in the ITRF, using the GPS receiver antenna phase center position. This is internally handled by the appropriate transformations and corrections in the calculation of the modeled measurements.

As the above discussion has made clear, the normal equations matrix is not fully populated, which is illustrated in Figure 4.1 for a 3 hour data arc, processed in 30 second steps and a 600 second interval for the empirical accelerations. Sparse matrix techniques are applied in storing and handling the individual matrix elements. When substituting the partitioned notation of the design matrix (4.27) in

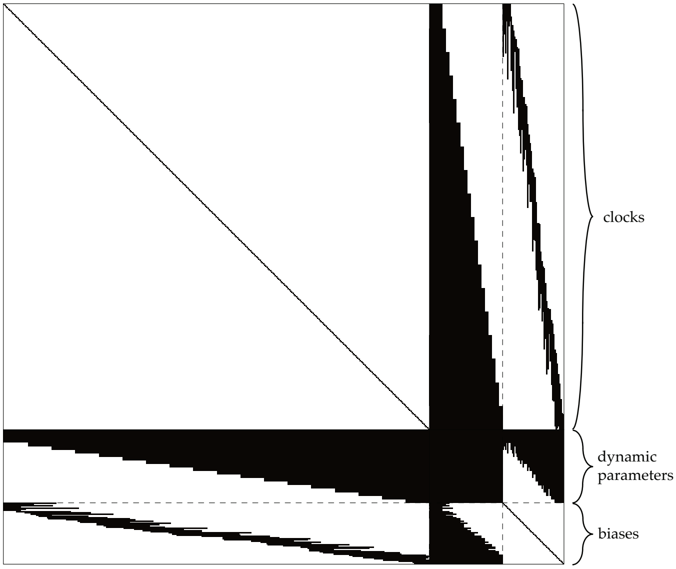

Figure 4.1 Structure of the normal equations for least-squares batch estimation of epoch-wise clock corrections, dynamic orbit parameters and carrier phase biases over continuous tracking arcs (3 hour data arc).

the least-squares system (4.26), this is rewritten as

$$\begin{pmatrix} \mathbf{H}_T^T\mathbf{W}\mathbf{H}_T & \mathbf{H}_T^T\mathbf{W}\mathbf{H}_Y & \mathbf{H}_T^T\mathbf{W}\mathbf{H}_B \\ \mathbf{H}_Y^T\mathbf{W}\mathbf{H}_T & \mathbf{H}_Y^T\mathbf{W}\mathbf{H}_Y & \mathbf{H}_Y^T\mathbf{W}\mathbf{H}_B \\ \mathbf{H}_B^T\mathbf{W}\mathbf{H}_T & \mathbf{H}_B^T\mathbf{W}\mathbf{H}_Y & \mathbf{H}_B^T\mathbf{W}\mathbf{H}_B \end{pmatrix} \begin{pmatrix} \Delta\mathbf{T} \\ \Delta\mathbf{Y} \\ \Delta\mathbf{B} \end{pmatrix} = \begin{pmatrix} \mathbf{H}_T^T\mathbf{W}(\mathbf{z}-\mathbf{h}(\mathbf{T}_0,\mathbf{Y}_0,\mathbf{B}_0)) \\ \mathbf{H}_Y^T\mathbf{W}(\mathbf{z}-\mathbf{h}(\mathbf{T}_0,\mathbf{Y}_0,\mathbf{B}_0)) \\ \mathbf{H}_B^T\mathbf{W}(\mathbf{z}-\mathbf{h}(\mathbf{T}_0,\mathbf{Y}_0,\mathbf{B}_0)) \end{pmatrix} \quad (4.34)$$

which can furthermore be reduced to

$$\begin{pmatrix} \mathbf{N}_{TT} & \mathbf{N}_{TY} & \mathbf{N}_{TB} \\ \mathbf{N}_{YT} & \mathbf{N}_{YY} & \mathbf{N}_{YB} \\ \mathbf{N}_{BT} & \mathbf{N}_{BY} & \mathbf{N}_{BB} \end{pmatrix} \begin{pmatrix} \Delta\mathbf{T} \\ \Delta\mathbf{Y} \\ \Delta\mathbf{B} \end{pmatrix} = \begin{pmatrix} \mathbf{n}_T \\ \mathbf{n}_Y \\ \mathbf{n}_B \end{pmatrix} \quad (4.35)$$

From this structure of the partitioned normal equations it may be recognized that only $\mathbf{N}_{YY}$ is a full matrix. In contrast to the dynamic parameters $\mathbf{Y}$ the partials with respect to $\mathbf{T}$ and $\mathbf{B}$ result in a large number of zero elements and sparsely filled matrix blocks. $\mathbf{N}_{TT}$, in particular, is a purely diagonal matrix since measurements only depend on one clock offset parameter at each epoch. Likewise $\mathbf{N}_{TB}$ and its transpose exhibit a narrow band structure (assuming a proper ordering of the bias parameters), since measurements at a specific epoch depend only on a limited number of bias parameters. The number of non-zero elements in each row of this sub-matrix is always limited to the number of active tracking channels. Finally, $\mathbf{N}_{TY}$ exhibits a triangular structure, reflecting the fact that the number of empirical acceleration parameters, on which the measurements at a particular epoch depend, increases continuously towards the end of the data arc.

To solve the normal equations, the dynamic and bias parameters are combined in a common vector $\mathbf{X} = (\mathbf{Y}, \mathbf{B})$, which allows the redefinition of the normal equations to the following system:

$$\begin{pmatrix} \mathbf{N}_{TT} & \mathbf{N}_{TX} \\ \mathbf{N}_{XT} & \mathbf{N}_{XX} \end{pmatrix} \begin{pmatrix} \Delta\mathbf{T} \\ \Delta\mathbf{X} \end{pmatrix} = \begin{pmatrix} \mathbf{n}_T \\ \mathbf{n}_X \end{pmatrix} \tag{4.36}$$

Thanks to the purely diagonal form of $\mathbf{N}_{TT}$, its inverse can easily be computed, which is then substituted in the updated equation of the dynamic and bias parameters:

$$\Delta\mathbf{X} = \left(\mathbf{N}_{XX} - \mathbf{N}_{XT}\mathbf{N}_{TT}^{-1}\mathbf{N}_{TX}\right)^{-1}\left(\mathbf{n}_X - \mathbf{N}_{XT}\mathbf{N}_{TT}^{-1}\mathbf{n}_T\right) \tag{4.37}$$

These updates $\Delta\mathbf{X}$ are subsequently back-substituted to obtain the updates for the clock offsets

$$\Delta\mathbf{T} = \mathbf{N}_{TT}^{-1}\left(\mathbf{n}_T - \mathbf{N}_{TX}\Delta\mathbf{X}\right) \tag{4.38}$$

After having obtained the updates for the estimation parameters the initial estimates are corrected for, and the newly obtained values are now used as initial values for a second run. Multiple iterations of this kind are required to cope with the non-linearity of the reduced dynamic estimation problem, and convergence is typically achieved within 3 to 4 iterations.

The formal covariances of the estimation parameters are given by

$$\mathbf{Q}_{XX} = \left(\mathbf{N}_{XX} - \mathbf{N}_{XT}\mathbf{N}_{TT}^{-1}\mathbf{N}_{TX}\right)^{-1} \tag{4.39}$$

which were already computed when solving for the dynamic estimation and bias parameter updates, and by

$$\mathbf{Q}_{TT} = \mathbf{N}_{TT}^{-1} + \left(\mathbf{N}_{TT}^{-1}\mathbf{N}_{TX}\right)\mathbf{Q}_{XX}\left(\mathbf{N}_{TT}^{-1}\mathbf{N}_{TX}\right)^T \tag{4.40}$$

Although the normal equations are generally not singular when both code and carrier phase observations are processed, and can thus be inverted, a stable estimation is in general not possible due to high correlations between estimated parameters. In order to prevent divergence of the satellite trajectory, uncorrelated a-priori information $\mathbf{Y}_{apr}$ with a predefined weight $\mathbf{\Lambda}_Y$ is added to the concerning part of the normal equations to constrain the dynamic estimation parameters. A priori information must also be added to the carrier phase biases $\mathbf{B}_{apr}$ and $\mathbf{\Lambda}_B$ if pseudorange observations are not processed. Ideally, this a-priori information only concerns one bias parameter for each carrier phase interconnected data arc. When incorporating the a-priori information the normal equations read

$$\begin{pmatrix} \mathbf{N}_{TT} & \mathbf{N}_{TY} & \mathbf{N}_{TB} \\ \mathbf{N}_{YT} & \mathbf{N}_{YY} + \mathbf{\Lambda}_Y & \mathbf{N}_{YB} \\ \mathbf{N}_{BT} & \mathbf{N}_{BY} & \mathbf{N}_{BB} + \mathbf{\Lambda}_B \end{pmatrix} \begin{pmatrix} \Delta\mathbf{T} \\ \Delta\mathbf{Y} \\ \Delta\mathbf{B} \end{pmatrix} = \begin{pmatrix} \mathbf{n}_T \\ \mathbf{n}_Y + \mathbf{\Lambda}_Y\mathbf{Y}_{apr} \\ \mathbf{n}_B + \mathbf{\Lambda}_B\mathbf{B}_{apr} \end{pmatrix} \tag{4.41}$$

where $\mathbf{\Lambda}_B$ is zero if both code and carrier phase observations are processed. The incorporation of a priori information leaves the fundamental structure of the normal equations unchanged, and the block elimination technique described above can still be used.

4.2.4 Numerical integration

As stated in the previous subsection, the integrator used to integrate the differential equations (4.6) and (4.14), the equation of motion and the variational equations, is the variable order and variable stepsize multistep DE integrator, described in detail in [*Shampine and Gordon*, 1975].

Generally formulated, the following first order differential equation has to be integrated over time

$$\frac{d}{dt}\mathbf{y}(t) = \mathbf{f}(t, \mathbf{y}) \tag{4.42}$$

The DE integrator is a predictor-corrector (PECE) algorithm with an Adams-Bashforth method as predictor and an Adams-Moulton method as corrector. The Adams-Bashforth multistep method makes use of already obtained solutions of the differential equation at previous time steps. Because the function in (4.42) depends itself on the unknown solution $\mathbf{y}$, the function is replaced by a polynomial interpolating m function values of previous steps up to t_i: $\boldsymbol{f}_i = \boldsymbol{f}(t_i, \boldsymbol{\eta}_i)$, with m the order of the method. This leads to:

$$\boldsymbol{\eta}_{i+1} = \boldsymbol{\eta}_i + h\mathbf{\Phi}_{\mathrm{AB}} \tag{4.43}$$

Here h is the time step and $\mathbf{\Phi}_{\mathrm{AB}}$ the increment function where the polynomial is integrated of the interval (t_i, t_{i+1}). The mth order Adams-Moulton method uses a polynomial which interpolates m function values at time steps t_{i-m+2} to t_{i+1}. This yields a better approximation of the function value at that point compared to the polynomial up to the previous point of the Adams-Bashforth method. Since the function value at t_{i+1} depends on the solution at this time step, $\boldsymbol{f}_{i+1} = \boldsymbol{f}(t_{i+1}, \boldsymbol{\eta}_{i+1})$, this is an implicit method which makes it impossible to calculate an explicit solution as is done in (4.43). Therefore the Adams-Moulton method is combined with an Adams-Bashforth method in a PECE-algorithm. This algorithm consists of four steps. In the first step a prediction of the solution at t_{i+1} is calculated with the Adams-Bashforth method (4.43):

$$\boldsymbol{\eta}^{\mathrm{p}}_{i+1} = \boldsymbol{\eta}_i + h\mathbf{\Phi}_{\mathrm{AB}} \tag{4.44}$$

In the next evaluation step the corresponding function value is calculated:

$$\boldsymbol{f}^{\mathrm{p}}_{i+1} = \boldsymbol{f}(t_{i+1}, \boldsymbol{\eta}^{\mathrm{p}}_{i+1}) \tag{4.45}$$

In the third step, the corrector, an improved value of the solution at the current time is calculated with the Adams-Moulton method:

$$\boldsymbol{\eta}_{i+1} = \boldsymbol{\eta}_i + h\boldsymbol{\Phi}_{\mathrm{AM}}(\boldsymbol{f}^{\mathrm{p}}_{i+1}) \tag{4.46}$$

In the final step the function value is updated which can then be used at the start of the next step. The solution at the time of interest is obtained by interpolating neighboring computed values.

The DE integrator is self-starting. It starts with order one and a very small initial stepsize, then both order and stepsize are increased to reach an optimal value within a few steps. The selection of the order and stepsize for the next integration step is determined by comparing the local truncation error for the order currently in use with the expected errors of higher or lower orders. The order is lowered when the predictor step was unsuccessful and raised when the corrector step was successful and the higher order leads to a smaller expected error. When the order is set, the appropriate step size is determined by checking if the predicted error gets smaller. Since changes in stepsize require an increased computational effort the stepsize is only changed by a factor of at least two. The maximum order is restricted to seven, because it was found in the course of this research that in the POD implementation with empirical acceleration intervals of 600 seconds and observations each 30 seconds a higher maximum order did not result in large stepsizes and associated higher orders. The average stepsize (for the state vector integration of a LEO) amounts to 6 seconds, with a maximum of around 16 seconds.

4.3 Using accelerometer data

The focus of this dissertation is the fusion of accelerometer data with the reduced dynamic orbit determination, in an effort to calibrate the accelerometer measurements and to improve the orbit accuracy. To this end, these measurements replace the non-gravitational accelerations, computed from force models, in the batch least-squares technique described above. As already stated in section 3.3, the application of the accelerometer data requires a correction for a scale factor and bias. These parameters are in this approach estimated during the OD, for each instrument axis. The applied accelerometer measurement model and the changes in the batch least-squares setup, are described here.

The calibration equation applied in this research is formulated as

$$\boldsymbol{a}_{cal} = \boldsymbol{S} \cdot \boldsymbol{a}_{obs} + \boldsymbol{b} \tag{4.47}$$

with $\boldsymbol{a}_{obs}$ being a three-dimensional vector with the accelerometer observations and $\boldsymbol{a}_{cal}$ the calibrated observations in the instrument frame, which coincides with the Spacecraft Body Frame (SBF), $\boldsymbol{S}$ being a 3×3 diagonal matrix containing a scale factor in each direction and $\boldsymbol{b}$ the bias vector. The bias parameter refers the measurements to the correct offset while the scale factor adjusts the amplitude of the variations. The calibrated accelerometer measurements are directly inserted as error-free into the equation of motion and the scale and bias factors are estimated in the least-squares adjustment procedure. This results in the augmentation of the estimation parameter vector with six parameters, three scale factors and three biases (with the drag and solar radiation coefficients removed). Although the GRACE Level 1B accelerometer data are delivered at a 1 Hz sampling, as stated in section 3.3, 10 second samples are used and linearly interpolated in between to the integration times to limit computational time and to match the GPS observation time interval. The CHAMP Level 2B accelerometer data are provided at 0.1 Hz.

Because the spacecraft equation of motion is defined and integrated in an inertial reference frame the measured accelerations have to be transformed from the SBF to the inertial reference frame according to equation (4.3), with the transformation matrix $\mathbf{C}(t)$, based on the quaternion attitude information. When no attitude data are available, no accelerometer measurements are used, also the corresponding GPS observation is not applied in the OD process, resulting in a data gap over which the trajectory is integrated (considering the GRACE data, quaternion data gaps occurs rarely, for CHAMP, a reprocessed interpolated data set is used). The entries in the sensitivity matrix are updated accordingly taking into account the transformation from SBF to the inertial frame. The derivative of the inertial accelerations with respect to the scale vector (grouping the three scale factors) is equal to the transformation matrix $\mathbf{C}(t)$ times a diagonal matrix with the measured accelerations on the diagonal. The derivative with respect to the biases (again grouped in a vector) equals the transformation matrix $\mathbf{C}(t)$ times the three dimensional identity matrix.

For the estimation of the biases, a good estimate of the a priori value proved to be necessary to guarantee and accelerate convergence. As the bias is a shift of the measurements to the (unknown) true value, the determination of an a priori bias is analogously composed of two steps. First the mean value of the accelerometer measurements is determined, and subtracted from the observations, which shifts them to fluctuate around zero. These reduced measurements are used in the POD process. Second, the mean value of the non-gravitational accelerations, modeled in the GHOST software or using the more advanced models described in section 3.2.4, is determined. The a priori bias is set to this value. This shifts the reduced accelerometer measurements to a magnitude which is expected to be close to the correct value. Summarizing, the a priori bias value is determined by the difference between the mean of modeled non-gravitational accelerations and the mean of the accelerometer measurements.

The results of the calibration efforts with this technique are described extensively in the next chapter, together with the numerical values of all OD setup parameters.

4.4 Kinematic orbit determination

As stated in the introduction to this chapter, kinematic orbit determination involves the reconstruction of the spacecraft trajectory based solely on the GPS observations and assumed known GPS ephemeris and clocks. At any given measurement epoch t_i both pseudorange and carrier phase observation types are parameterized with the phase center position of the GPS receiver antenna and the GPS receiver clock offset, $\mathbf{x}_i = (x_i; y_i; z_i; c\delta t_i)$. Since the spacecraft is continuously moving, a new position (in the ITRF) and clock offset have to be determined at every epoch. In addition, the carrier phase observations also contain the ionosphere free bias parameter $b_j = (\lambda_{\mathrm{IF}} A_{\mathrm{IF}})_j$, which remains constant over time until a cycle slip or phase break occurs. A typical 24 hour data arc counts a total of $n_X = 8640$ epochs to be processed, when the measurements are processed at 10 second intervals. Most of the time the total number of independent ambiguity parameters over 24 hours is approximately $n_B \approx 450 - 500$ for space-borne scenarios. Together this results in a total number of roughly $4n_X + n_B \approx 35000$ estimation parameters that need to be adjusted for a single day.

Although the total number of estimation parameters is quite large, they can be efficiently solved for when grouped into the $4n_X$ dimensional position and clock offset vector

$$\mathbf{X} = \left(\mathbf{x}_0; \cdots; \mathbf{x}_i; \cdots; \mathbf{x}_{n_X-1}\right) \tag{4.48}$$

and the n_B dimensional carrier phase ambiguity vector

$$\mathbf{B} = \left(b_0; \cdots; b_j; \cdots; b_{n_B-1}\right) \tag{4.49}$$

allowing a partitioned solution of the normal equations similar to the partitioning described above for the batch least-squares orbit determination, which here becomes

$$\begin{pmatrix} \mathbf{N}_{XX} & \mathbf{N}_{XB} \\ \mathbf{N}_{BX} & \mathbf{N}_{BB} \end{pmatrix} \begin{pmatrix} \Delta\mathbf{X} \\ \Delta\mathbf{B} \end{pmatrix} = \begin{pmatrix} \mathbf{n}_X \\ \mathbf{n}_B \end{pmatrix} \tag{4.50}$$

The entry in the design matrix related to the partials of a modeled measurement of GPS satellite s with respect to the position and clock offset only relate to the epoch t_i the measurement was taken, where the position partials equals the line of sight vector

$$\frac{\partial h_i^s}{\partial \mathbf{X}} = \left(\mathbf{0}^T_{(0)}, \ldots, \mathbf{0}^T_{(i-1)}, \left(\,\mathbf{e}^s(t_i)\,;\,1\,\right)^T_{(i)}, \mathbf{0}^T_{(i+1)}, \ldots, \mathbf{0}^T_{(n_X-1)}\right) \tag{4.51}$$

The partials of the modeled carrier phase measurement of GPS satellite s with respect to the ambiguity parameters equals equation (4.29).

Thanks to the partitioned formulation, the normal equations can be solved more efficiently than by direct inversion of the full matrix. The part relating to the positions and clock offsets, $\mathbf{N}_{XX}$, is a block diagonal matrix with 4×4 elements.

Inversion of this matrix ($\mathbf{N}_{XX}^{-1}$) is easily accomplished by a simple inversion of the individual 4×4 diagonal sub-matrices. Therefore, first the bias parameter updates are solved for

$$\Delta\mathbf{B} = \left(\mathbf{N}_{BB} - \mathbf{N}_{BX}\mathbf{N}_{XX}^{-1}\mathbf{N}_{XB}\right)^{-1}\left(\mathbf{n}_B - \mathbf{N}_{BX}\mathbf{N}_{XX}^{-1}\mathbf{n}_X\right) \tag{4.52}$$

which are subsequently back-substituted to find the updates for the positions and clock offsets,

$$\Delta\mathbf{X} = \mathbf{N}_{XX}^{-1}\left(\mathbf{n}_X - \mathbf{N}_{XB}\Delta\mathbf{B}\right) \tag{4.53}$$

Due to the fact that both GPS pseudorange and carrier phase observations are processed the normal equations can readily be inverted. It is however also possible to process solely ionosphere free carrier phase data, which could be more accurate. This requires the same parameters to be adjusted, but with roughly half of the observation data available. The resulting system however is no longer overdetermined since a singularity is now introduced. A common shift in the carrier phase bias parameters can no longer be separated from a common shift in all receiver clock offsets and vice versa. A solution to this is adding (uncorrelated) a-priori information to e.g. the bias parameters. The a-priori bias values $\mathbf{B}_{apr}$, derived from pseudoranges, and their accompanying data weights, or information matrix, $\mathbf{\Lambda}_B$ are added to the normal equations as

$$\begin{pmatrix} \mathbf{N}_{XX} & \mathbf{N}_{XB} \\ \mathbf{N}_{BX} & \mathbf{N}_{BB} + \mathbf{\Lambda}_B \end{pmatrix} \begin{pmatrix} \Delta\mathbf{X} \\ \Delta\mathbf{B} \end{pmatrix} = \begin{pmatrix} \mathbf{n}_X \\ \mathbf{n}_B + \mathbf{\Lambda}_B\mathbf{B}_{apr} \end{pmatrix} \tag{4.54}$$

which can still be solved in the same way as before, since the general structure has not changed.

4.5 GHOST processing

Within GHOST, precise orbit determination based on undifferenced GPS observations is a three step process, illustrated in Figure 4.2, which is fully self-contained. The first step is the generation of kinematic single point position solutions at discrete (measurement) epochs using only ionosphere free GPS pseudoranges, implemented in the *Single Point Positioning for LEO satellites* (SPPLEO) program. The second step involves the dynamical filtering of these kinematic positions using a reduced-dynamic batch least-squares approach, where the SPPLEO position estimates, instead of GPS observations, are used as measurements. This is done in the so-called *Position Fit* (PosFit) program. The output of this second step is a continuous and smooth orbit with medium precision (15-25 cm, 3-dimensional), provided in the SP3 format [*Spofford and Remondi*, 2009]. The third and final step of the process consists of the actual precise orbit determination where the just derived coarse a-priori orbit is used for GPS data editing, as described at the end of this section. The reduced dynamic batch least-squares technique described in section 4.2 is implemented in the tool called *Reduced Dynamic Orbit Determination* (RDOD). Kinematic orbit determination as described in the previous section, is performed by the *Kinematic Point Positioning* (KIPP) program, and an extended Kalman filter, implemented in the *Filter for Adjustment of Satellite Trajectories* (FAST) tool, is also able of computing reduced dynamic orbits. The latter tool is not considered for the research in this dissertation, as the use of accelerometer data implies estimating a scale and bias which remain constant over the considered data arc, where typically a Kalman filter is useful to estimate epoch-varying parameters. The KIPP program is used to determine the GOCE rapid science kinematic orbits [*Visser et al.*, 2008].

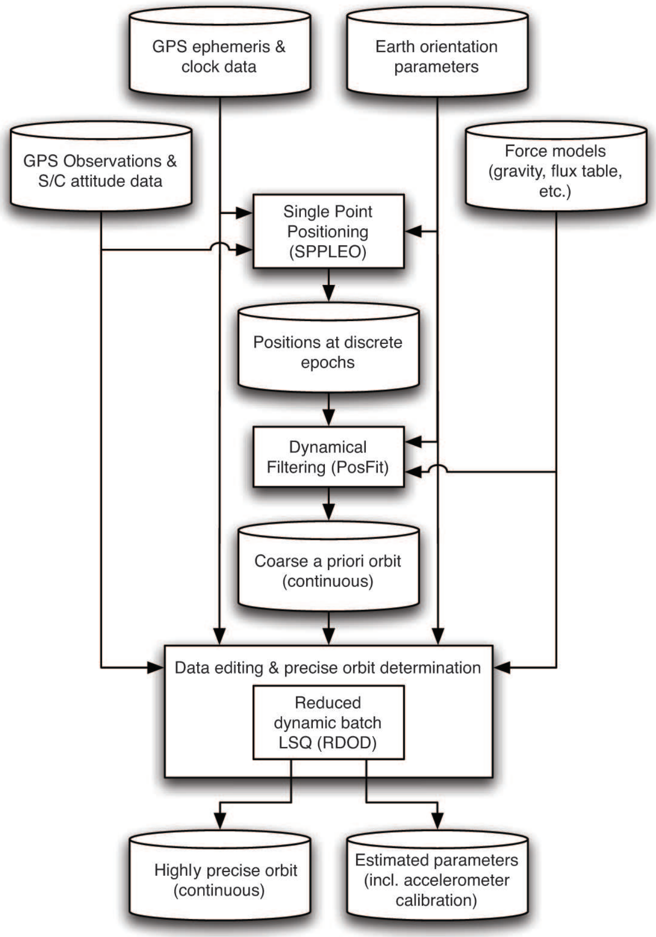

Figure 4.2 Processing scheme for GPS-based batch least squares precise orbit determination of LEO satellites using the GHOST toolkit

A crucial factor of GPS based precise orbit determination is the quality of the data used. Therefore proper methods for data screening have to be applied in order to detect outliers and bad measurements, which are regularly encountered. The three POD programs within the GHOST toolkit validate the GPS measurements prior to the actual orbit determination process using a combination of different statistical tests and simple limit checks. For example, user configurable thresholds are used to discard any observations taken below a certain elevation or below a minimum SNR ratio. Also the presence of GPS satellite orbit and clock data is verified since this is required for processing the observations.

In addition to these simple limit checks the quality of the GPS code and carrier-phase measurements is assessed more thoroughly by comparison with modeled observations with respect to the a-priori coarse orbit determined in the second step of the GHOST processing scheme. At each epoch these modeled geometric ranges are used in conjunction with the observed ionosphere free pseudoranges to determine the GPS receiver clock offset value. From the set of n $\geq$ 2 observations at epoch t_j an estimate

$$c\delta t_r(t_j) = \frac{1}{n}\sum_{i=1}^{n}\Big(P^i_{\mathrm{IF}}(t_j) - \big(\rho^i_r(t_j) - c\delta t^i(t_j)\big)\Big) \tag{4.55}$$

of the receiver clock offset and the associated residuals

$$res^i(t_j) = P^i_{\mathrm{IF}}(t_j) - \big(\rho^i_r(t_j) + c\delta t_r(t_j) - c\delta t^i(t_j)\big) \tag{4.56}$$

are now obtained. Whenever the standard deviation of these residuals exceeds a predefined threshold, the code observation that contributes the dominating error is identified through subset solutions and removed from the set of observations. If necessary, the process is repeated to reject multiple outliers at the same epoch. The GPS receiver clock offsets determined in this way can be used as a-priori values in the orbit determination process later on. This approach to pseudorange editing provides a safe and robust way to identify outliers. Although the receiver position from the a-priori orbit also exhibits an error, this is largely absorbed by the receiver clock offset. The small remaining contribution as well as pseudorange multipath, systematic errors and noise not absorbed can be accounted for by the size of the standard deviation threshold.

Whereas the code observations are subject to outliers, which need to be detected, the carrier phases have to be accurately screened for cycle slips, i.e. sudden jumps in the carrier phase bias. Since the carrier phase biases are constant over time a sudden jump can be detected by examining time differenced carrier phase measurements between two consecutive measurement epochs, t_{j-1} and t_j, in a similar process as for the code observations. Instead of the receiver clock offset the time difference of two consecutive clock offsets is determined. From the set of n $\geq$ 2 observations an estimate

$$c\delta t_r(t_{j-1}, t_j) = \frac{1}{n}\sum_{i=1}^{n}\Big(L^i_{\mathrm{IF}}(t_{j-1}, t_j) - \big(\rho^i_r(t_{j-1}, t_j) - c\delta t^i(t_{j-1}, t_j)\big)\Big) \tag{4.57}$$

of the time differenced receiver clock offset between the measurement epochs t_j and t_{j-i} and the associated residuals

$$\begin{aligned} res^i(t_{j-1}, t_j) = \; & L^i_{\mathrm{IF}}(t_{j-1}, t_j) - \big(\rho^i_r(t_{j-1}, t_j) + c\delta t_r(t_{j-1}, t_j) \\ & - c\delta t^i(t_{j-1}, t_j)\big) \end{aligned} \tag{4.58}$$

of the time differenced carrier phase observations is determined. Again, whenever the standard deviation of these residuals exceeds a predefined threshold, the carrier phase observation that contributes the dominating error is assumed to have experienced a cycle slip and is removed from the set of observations. If necessary, the process is repeated to identify multiple cycle slips. The threshold for this process however must be set small enough in order to guarantee no undetected cycle slips. This is possible due to the low noise level in the carrier phase data and the fact that errors in the a-priori positions used almost cancel completely over short time spans.

Chapter 5

Accelerometer calibration: CHAMP & GRACE results

After the description of the GPS observations, the forces acting on a LEO satellite and the detailed explanation of the applied estimation technique in the previous chapters, here the analysis of the calibration of the accelerometer measurements of board the CHAMP and GRACE spacecraft is given ([*Van Helleputte and Visser*, 2008], [*Van Helleputte et al.*, 2009]).

In the first section, the a priori settings applied in the orbit determination are introduced and the different cases which are treated in the continuation of this chapter are summarized. After that, the estimated calibration parameters are presented. First the results of an unconstrained estimation are given, where the calibration parameters are estimated freely from the observations. The discussion in the consecutive sections is divided into two parts, section 5.3 (flight axis) and 5.4 (radial and cross-track axes). First, in section 5.3, the results in flight direction are discussed. In this direction, the estimation of the calibration parameters by the technique of GPS-based orbit determination is the most stable because of the large non-gravitational acceleration level in this direction. In the other two directions, radial and cross-track, the estimation of the accelerometer scale factor and bias values is more challenging, which is treated in more detail in section 5.4. For the GRACE satellites, the accelerometer measurements are defined in the Spacecraft Body Fixed frame (SBF) [*Bettadpur*, 2007], which is depicted for the trailing GRACE satellite in Figure 5.1. The SBF has the X_{SBF}-axis nominally pointing in the direction of the orbital velocity. The attitude of the satellite is kept aligned to within one degree of the orbit frame (RTN). The leading GRACE satellite has the X_{SBF}-axis pointing towards the trailing spacecraft. CHAMP has the same general alignment of the SBF and RTN frame as the trailing GRACE satellite, although this alignment is kept within a more tolerant two degrees.

Following the discussion on the estimated calibration parameters, in section 5.5

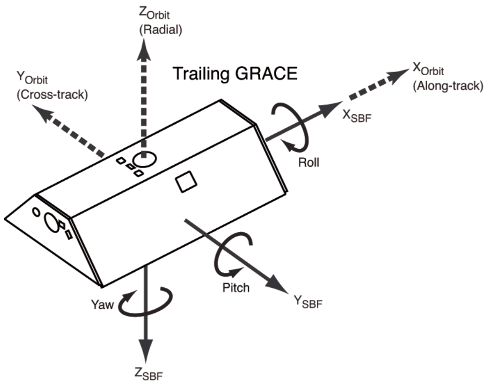

Figure 5.1 SBF and RTN frame definitions for the trailing GRACE spacecraft

some special topics are covered, namely the estimation of empirical accelerations and the variation of the estimation arc length. Next, in section 5.6, an assessment of the quality of the orbit solutions obtained when using and calibrating the accelerometer measurements is given. After that an alternative technique, the stacked normal matrices approach (i.e. multi-arc technique), is introduced in section 5.7 and the results of this technique are presented. At the end of this chapter two methods of validating the calibration results are outlined in section 5.8.

5.1 Selected cases: force models and estimated parameters

To start with, the force models used in generating the results described in this chapter are summarized. The nature of these forces and the references for the models applied have already been discussed in chapter 3. As the accelerometer measurements are introduced in the orbit determination to replace the non-gravitational forces, no non-gravitational models are used in the estimation. The applied gravitational force models are listed in Table 5.1. The GRACE GGM02S model is used for all the processing described in this chapter, and although more recent (and thus possibly more accurate) gravity field models have become available after the research described in this dissertation, this model proved useful enough for the analysis presented here. According to a calibrated gravity field covariance matrix kindly provided by the NASA Goddard Space Flight Center (priv. comm., Dave Rowlands), the gravity field induced orbit error for satellites flying orbits similar to CHAMP and GRACE is equal to 3, 50 and 4 mm for the radial, along-track and cross-track direction, respectively. These are in fact conservative numbers, assuming a fully dynamic orbit propagation.

Item	Description
Static gravity field	GRACE GGM02S model, 100×100
Tidal perturbations	Solid Earth tide (4×4, diurnal)
	Polar tide (IERS/IGS)
	Ocean tides (TOPEX 4.0)
3rd body gravity	Analytical series expansions of luni-solar coordinates

Table 5.1 Overview of the gravitational dynamical models applied in the processing of the accelerometer measurements

A-priori standard deviation	
$\sigma_{\mathbf{r}}$ [m]	100.0
$\sigma_{\mathbf{v}}$ [m/s]	100.0
σ_{a_R} [nm/s^2]	5.0
σ_{a_T} [nm/s^2]	10.0
σ_{a_N} [nm/s^2]	10.0
$\sigma_{bias_{CP}}$ [m]	1.0
Auto-correlation time	
$\tau_{a_{(R,T,N)}}$ [s]	600.0
Observation weight	
σ_{PR} [m]	0.7
σ_{CP} [m]	0.03

Table 5.2 A-priori constraints and observation weights used for the processing of the accelerometer measurements. Identical values are applied to the GRACE and CHAMP spacecraft.

	CHAMP	GRACE A	GRACE B
S_X	0.833	0.96	0.96
S_Y	0.875	0.98	0.97
S_Z	1.0	0.94	0.92

Table 5.3 A priori scale factors in the Spacecraft Body Frame, obtained from [*Bettadpur*, 2003; *Förste*, 2002]

This covariance matrix was derived from only 1 month of GRACE data for a spherical harmonic expansion complete to degree and order 60. GGM02S is based on about one year of GRACE observations. The truncation to degree and order 100 gives a reduction in processing time. Including higher degrees does not result in significantly different orbits. The other gravitational models were already used in generating reduced dynamic orbits in [*Montenbruck et al.*, 2005*a*].

Table 5.2 gives an overview of the a priori settings which are common for all cases described later on. These include the standard deviation of the position and velocity vectors, $\sigma_{\mathbf{r}}$ and $\sigma_{\mathbf{v}}$, the a priori stand deviation of the empirical accelerations in Radial, Tangential and Normal direction, σ_{a_R}, σ_{a_T} and σ_{a_N}, the auto-correlation time $\tau_{a_{(R,T,N)}}$ of these parameters and the a priori standard deviation of the carrier phase bias, $\sigma_{bias_{CP}}$. The observation weights of the pseudorange and carrier phase observations, σ_{PR} and σ_{CP}, are given and stem from the analysis in section 2.4, where here more relaxed values are applied, to reflect the noise and systematic errors and to scale the formal errors.

The empirical accelerations were introduced in section 4.2. Because drag and solar radiation pressure models imply a higher amount of uncertainty compared to the direct observation by an accelerometer, the a priori standard deviation of the along-track empirical accelerations is reduced to a value of 10 nm/s^2, compared to a higher value of about 30 nm/s^2 in a standard reduced dynamic orbit determination.

The a priori scale factor values listed in Table 5.3 for the CHAMP and both GRACE spacecraft are used throughout the analysis described in this chapter, unless stated otherwise. They are based on advertised values [*Bettadpur*, 2003; *Förste*, 2002].

To conclude this introductory section, Table 5.4 gives an overview of the different cases which are treated in this chapter, where in general complexity is increased in the sequence of cases. The table includes a notion of the characteristic of each case,

case	emp acc	section(s)	figure(s) & table(s)
unconstrained estimation	no	5.2	Fig.5.2, Fig. 5.3, Tab.5.5
unconstrained estimation	yes	5.2	Tab.5.5
varying scale factor	yes	5.3.1	Fig.5.4
constant scale factor	yes	5.3.2, 5.4	Fig.5.5, Fig.5.7, Fig. 5.8, Tab.5.6
constant scale factor & different a priori biases	yes	5.4	Fig.5.9
constant scale factor	no	5.5.1	Tab.5.8

Table 5.4 Overview of the different cases treated in this chapter with a reference to the section where the case is discussed, the related figures and tables, and an indication whether empirical accelerations are estimated (yes) or not (no)

the section where the case is discussed and a list of the tables and figures which relate to the specific case. First, only six state parameters are estimated together with three scale and bias parameters, where no constraints are put on the calibration parameters. This is a first step to analyze how well these parameters can be determined from the GPS observations. It turned out that only the scale in flight direction can be estimated reliable, therefore in the other directions constraints are necessary, which is done in the other cases. A further division is then made in the estimation of the scale factor in flight direction, first it is estimated on an arc by arc basis, next it is kept constant (as well as the scale factors in the other two directions). Furthermore in the table it is indicated whether or not empirical accelerations are estimated as well, as some tests were done without. A more thorough explanation of all cases is given in the corresponding sections.

5.2 Unconstrained estimation

As a first test the calibration parameters are estimated without constraints. The results of such an unconstrained estimation are presented in Table 5.5 for a 30 day test period for GRACE B, where the two columns represent an estimation with (1) and without (2) empirical accelerations. Without applying empirical accelerations (or so-called pseudo-stochastic parameters), the estimation is close to a purely dynamic orbit determination. In a standard reduced dynamic POD technique the addition of empirical accelerations gives better results, therefore also a test is done with empirical accelerations. For an unconstrained estimation, the most stable results in flight direction are obtained when no empirical accelerations are applied. When they are estimated, the extra degrees of freedom apparently give an incorrect distribution of information in this case, although the orbit fit (defined as the RMS of orbit coordinate differences) improves in the latter case from about 10 cm to 6 cm.

Without empirical accelerations, the scale factor in along-track direction is stable, showing a small variation of 0.015 and a value of 0.95, close to the advertised value. In radial direction, the scale can not be determined reliably with this method. In cross-track direction, the scale factor is about 1.05, with a variation of about 0.15, which is slightly lower when empirical accelerations are estimated. When a 5 year period (2003-2007) is analyzed in this manner, see Figure 5.2, it becomes apparent that only during periods with a strong signal this method gives a stable (along-track) scale factor. Over the whole period the variation increases, while at the same time the variation of the non-gravitational signal decreases (as depicted at the bottom of Figure 5.4 in section 5.3.1). The mean value of 0.95 is the same as for the short test period. Results for the scale factor in flight direction of the GRACE A satellite for the same 30 day test period are 0.96 ± 0.014 and 0.85 ± 0.024 for CHAMP.

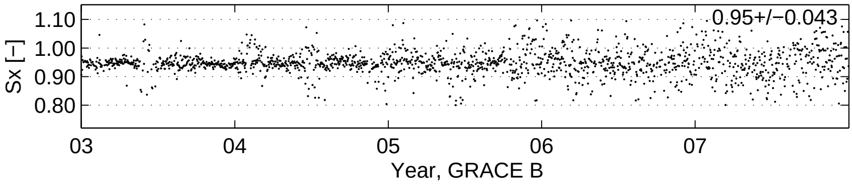

Figure 5.2 Scale in X-direction for GRACE B determined by an unconstrained estimation (without empirical accelerations)

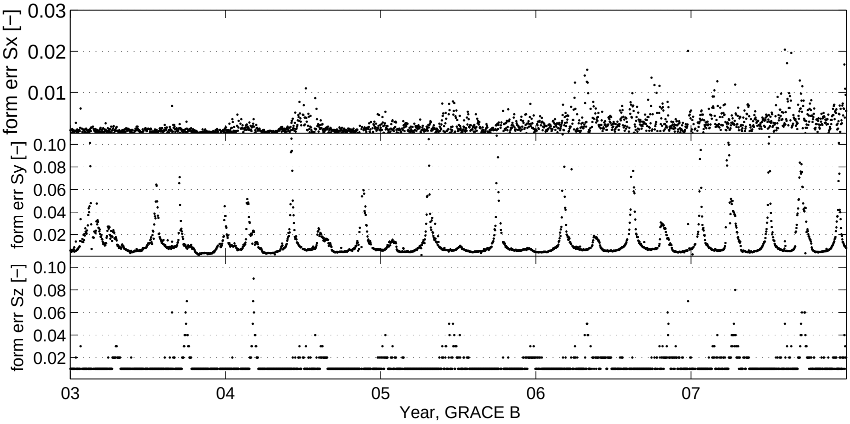

Figure 5.3 Formal errors of scale parameters for GRACE B determined by an unconstrained estimation (without empirical accelerations)

	(1)	(2)
S_X [-]	0.97 $\pm$ 0.024	0.95 $\pm$ 0.015
S_Y [-]	1.04 $\pm$ 0.138	1.05 $\pm$ 0.149
S_Z [-]	1.47 $\pm$ 1.07	1.0 $\pm$ 0.536
B_X [nm/s^2]	-569 $\pm$ 11	-559 $\pm$ 7
B_Y [nm/s^2]	9800 $\pm$ 1301	9904 $\pm$ 1408
B_Z [nm/s^2]	-1105 $\pm$ 927	-702 $\pm$ 462
3D RMS [cm]	5.81	9.39

Table 5.5 Scale and bias parameters for GRACE B of DOY 270-300 in 2003, with (1) σ_S = 10, σ_B = 500 nm/s^2 (2) idem, no empirical accelerations

In Figure 5.3 the formal errors of the scale factors for GRACE B are plotted for an unconstrained estimation. Clearly, only in X-direction very small values are reached, while in Y- and Z-direction the lowest value obtained is about 0.01.

Near the end of the five year period, also the formal error in X-direction increases, which is also caused by the gradually decreasing signal strength, as depicted at the bottom of Figure 5.4, included in the next section.

5.3 Calibration parameters in flight direction

In this section, dealing with the calibration parameters in flight direction (along the X_{SBF}-axis), two different approaches are discussed. The first one is referred to as varying scale factor (section 5.3.1), where the scale factor in this direction is estimated for each orbital arc. In the second approach (section 5.3.2) the scale factor is kept constant to assess the stability of the bias estimation.

5.3.1 Varying scale factor

Five years (2003-2007) of CHAMP and GRACE data were processed, computing daily calibration parameters. As was shown in the previous section, an unconstrained estimation of the scale factor in radial and cross-tack direction results in a large variation. Therefore these parameters are tighter constrained in these directions. The a priori standard deviation of the scale and bias parameter in flight direction are 0.1 and 100 nm/s^2, and 0.01 and 1 nm/s^2 in radial and cross-track direction. The reason for the tighter constraints on the bias parameters is elaborated in more detail in section 5.4. The a priori standard deviation of the other estimation parameters, including the empirical accelerations which are here estimated as well, were listed in Table 5.2. These settings are used for the whole period and resulted from tuning towards small ionospheric-free carrier phase residuals (around 9 mm) and an orbit fit of about 3.5 cm in 3D RMS sense with respect to JPL reference orbits [*Case et al.*, 2002] for GRACE orbits, and around 6 cm for CHAMP orbits with respect to DEOS reference orbits [*Van den IJssel et al.*, 2003]. All reference orbits are computed with different software and without accelerometer data. The good fit is supported by computing Satellite Laser Ranging (SLR) residuals, which are presented in a more detailed orbit quality analysis in section 5.6.

In Figure 5.4 the bias (B_x) and scale factor (S_x) in X-direction are presented for the GRACE B satellite. What is immediately apparent when inspecting the figure is the strong anti-correlation between scale and bias parameters. This makes it not straightforward to assess instrument behavior. The standard deviation of the scale factor amounts to 0.028. With this approach, the total non-gravitational acceleration of the spacecraft is calibrated, rather than the scale and bias parameters separately.

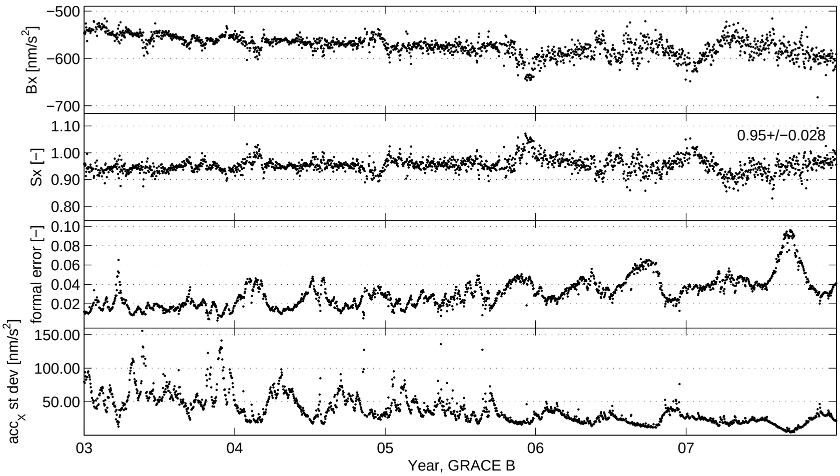

Figure 5.4 Bias and scale in X-direction for GRACE B, combined with formal error of the scale factor and RMS about mean (standard deviation) of the accelerometer measurements

To investigate the large variation of the scale in flight direction more closely, Figure 5.4 groups the scale factor with the formal error of this parameter and the RMS about the mean of the accelerometer measurements (acc_x), which is a measure for the signal strength. The formal error of the scale factor is an order of magnitude smaller than the constraint (0.1), meaning that the scale is determined largely by the observations (as it preferably would be). Inspecting the bottom two plots confirms that the formal error is strongly anti-correlated with the signal strength. With a reducing acceleration strength, due to a decreasing solar activity, the formal error increases, as well as the variation of the estimated parameter. Reversely, a stable estimation of the scale factor, showing a small variation, occurs when the signal strength is large.

The influence of the quality and availability of the GPS observations and attitude data was also investigated, but no correlation between these two data sets and the variation of the estimated scale factor could be found. The same holds for the orbit geometry, where the shadow periods and variation of β-prime, the angle between the orbital plane and the sun vector, did not reveal apparent correlations.

5.3.2 Constant scale factor

Because of the strong correlation between scale and bias, and because a comparison of the data with non-gravitational force models (e.g. eclipse transitions, E. Doornbos, DEOS, private communication) indicates that the scale is not expected

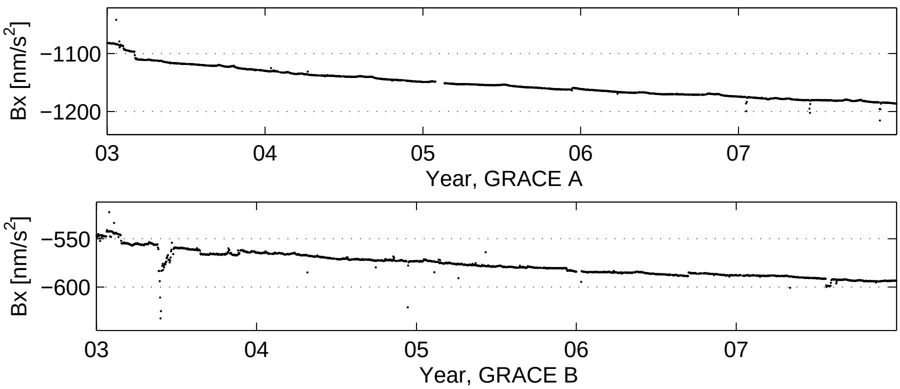

Figure 5.5 Bias in X-direction for GRACE A and B, estimated with a constant scale factor

to show large variations, another approach is proposed, where the scale factor in all three directions is kept constant. The scale factors are set equal to the values listed in Table 5.3. The a priori standard deviation of the bias parameters is the same as described above, so the value in X-direction is a hundred times larger than in the other two directions. The resulting bias values are now much smoother, illustrated in Figure 5.5 with the bias parameter in flight direction for the GRACE spacecraft. All sequences show a clear trend, and distinct jumps in the bias values are now visible. The outlier points can be attributed to maneuvers or data gaps in the GPS or attitude data. For CHAMP, the bias in X-direction is presented in Figure 5.6, where marks are inserted which are related to events onboard the satellite, and more specific to the accelerometer. These events were provided by the CHAMP team (H. Lühr, GFZ, private communication) and consist of resets, software updates an switches of the redundant electronics. The large jumps in the bias can be related to such events (start of 2003 and 2004) and were recognized by the CHAMP project team, who needed to include these in their bias function to get reasonable results. Furthermore lots of events can be observed in the start of the mission, which are mentioned in [*Perosanz*, 2003].

It can be concluded that the calibration benefits from a sequential procedure, where first daily biases and scale factors are estimated, for example as described in the previous section, after which the average of the scale factor is determined. Another possibility is the use of a multi-arc technique, where a constant value for a longer period is estimated. This is described at the end of this chapter. In the next step the scale factor is kept constant and new daily biases are estimated.

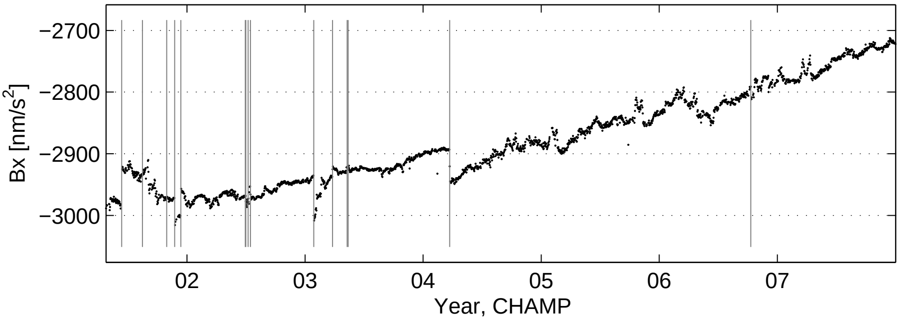

Figure 5.6 CHAMP bias in X-direction with grey lines indicating known satellite (acceleromter) events, such as rests and switches of redundant electronics

5.4 Calibration parameters in radial and cross-track direction

After the discussion of the calibration parameters in flight direction in the previous section, here the results of the estimation in radial and cross-track direction are discussed. In Figure 5.7 the bias parameters in Y- and Z-direction (B_y and B_z) are presented for the GRACE B satellite. The scales in these two directions are not included because they show little variation with respect to the a priori values, because of the applied constraints (an a priori standard deviation of 0.01 as stated in section 5.3.1). The solid lines show the advertised values [*Bettadpur*, 2003], where it has to be mentioned that their period of applicability is stated to be limited until November 1st, 2003. However, it is clear that the user of the accelerometer data has to calibrate the accelerometer measurements. The jumps in the bias parameter in Z-direction in 2003 are already visible in the accelerometer data.

Figure 5.8 shows the signal strength, computed as the RMS about mean (standard deviation) of each day, for the two directions described here (acc_y and acc_z). In both directions the signal is rather small, below 25 nm/s^2, and there is little variation over the years, compared to the accelerometer signal in flight direction, which was shown at the bottom of Figure 5.4.

When estimating the calibration parameters, the scale and bias factors in Y_{SBF} and Z_{SBF} direction are tightly constrained to their a priori values. It was found that the formal errors of an unconstrained estimation are about 100 and 30 times larger for the scale factors in Y and Z direction, and 30 and 100 times larger for the biases in these directions, compared to the formal errors in X direction, which indicates that unconstrained estimation of these parameters is unstable, as was shown in section 5.2. As mentioned earlier, the estimation of the bias parameter in Y- and Z-direction is tightly constrained to the a priori values, because of a strong correlation between these parameters and the initial state. This is supported by the statistics in Table 5.6, where σ represents the a priori standard deviation of the scale and bias parameters. In case (2) the constraints on the bias are relaxed to 100 nm/s^2 and a mean offset with respect to the reference trajectory in radial and cross-track direction is visible. The GPS-based orbits are also confronted with SLR observations, and a big shift in the bias value and in the SLR residuals mean and RMS value can be seen. This indicates that the bias values in radial and cross-track direction, estimated in case (2), are less reliable. The difference in the bias values in Y- and Z-direction and the corresponding shift of the orbit can be attributed for a large part to coupling with the central term of the gravity field.

The a priori bias parameter consists of the mean of modeled non-gravitational forces, computed with the GHOST software, which does not include albedo radiation and has a canonball solar radiation pressure model. To check the effect of neglecting albedo radiation and the simple radiation pressure model, another set of a priori biases for the GRACE satellites were computed with the more accurate

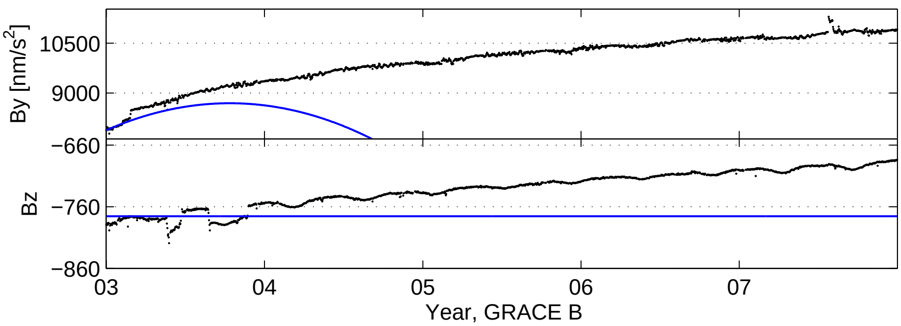

Figure 5.7 Bias parameters in Y- and Z- direction of the SBF for GRACE B, compared to advertised values (solid line)

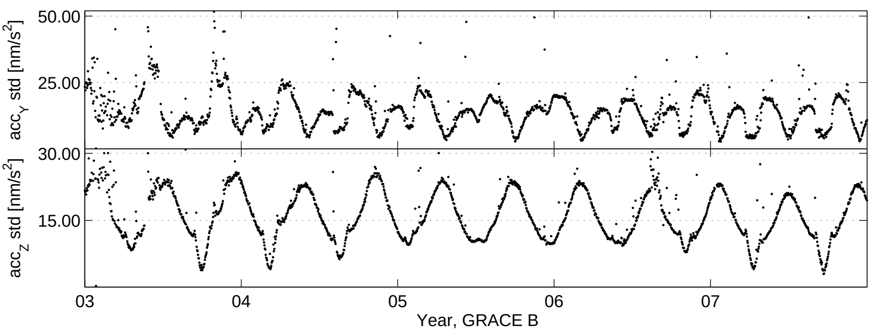

Figure 5.8 Accelerometer signal strength in Y- and Z- direction of the SBF for GRACE B

	(1)	(2)
B_X [nm/s^2]	-566 ± 0.5	-564 ± 0.5
B_Y [nm/s^2]	9214 ± 15	9164 ± 22
B_Z [nm/s^2]	-786 ± 2	-633 ± 4
mean R [cm]	-1.02	3.12
mean T [cm]	0.02	-0.19
mean N [cm]	-0.50	3.49
3D RMS [cm]	3.35	5.75
mean SLR [cm]	-0.80	-3.12
RMS SLR [cm]	1.79	4.00

Table 5.6 Bias values (mean and standard deviation) for GRACE B of DOY 270-300 in 2003, with (1) σ_S = 0.001, $\sigma_{B_{Y,Z}}$ = 1 nm/s^2 (2) σ_S = 0.001, $\sigma_{B_{Y,Z}}$ = 100 nm/s^2 , mean offset wrt JPL reference orbits and SLR residual statistics

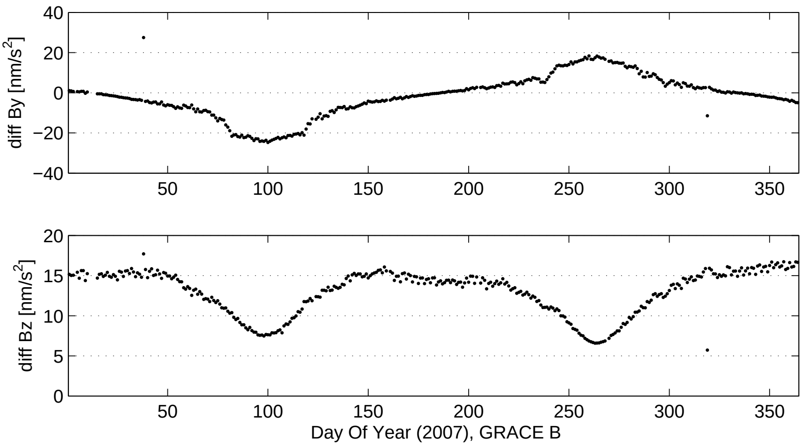

Figure 5.9 Differences in bias values for GRACE B in 2007 in Y- and Z-direction, estimated with a priori values determined with a different force modeling

non-gravitational force models described in section 3.2.4. There is no difference in flight-direction, the calibration parameters in this direction are estimated almost freely, without tight constraints to an a priori value. The difference in the resulting bias values in Y- and Z-direction for GRACE B are presented in Figure 5.9 for 2007. As the bias in these directions is constrained to 1 nm/s^2 to the a priori value, this reflects mainly the difference in the non-gravitational force models used to determine the a priori bias. The effect on the bias in Z-direction is a small varying offset, where the difference in Y-direction builds up when the orbital plane is more perpendicular to the sun vector, which is further discussed in section 5.6 about the orbit quality analysis. This illustrates that in Y- and Z-direction the bias parameters can not be determined very precisely from the GPS observations with this method.

		mean [nm/s^2]	RMS about mean [nm/s^2]
CHAMP	along-track	0.06 ± 0.1	10.9± 2.4
	cross-track	0.35 ± 0.6	28.0 ± 2.3
GRACE A	along-track	0.04 ± 0	4.4± 1.4
	cross-track	-1.04 ± 0.2	7.3 ± 1.5
GRACE A	along-track	0.79 ± 3.4	27.2± 11.2
(no acc data)	cross-track	-0.97 ± 0.2	7.5 ± 1.4

Table 5.7 Variation of the estimated empirical accelerations, for a period of one year (2003) for CHAMP, GRACE A, and GRACE A without applying accelerometer data (standard reduced dynamic technique)

5.5 Special topics: empirical accelerations and arc length

5.5.1 The influence of the estimation of empirical accelerations

In the standard processing, with the input parameters listed in Table 5.2, empirical accelerations are estimated to account for deficiencies in the gravitational force models and in the case of CHAMP to account for accelerations due to maneuver events, which are not included in the accelerometer data (whereas these are present in the GRACE accelerometer data). When using accelerometer measurements, the estimated empirical accelerations in along-track direction are small, where in cross-track direction the pattern remains largely unaffected (comparing the case with and without accelerometer data), which is an indication that the applied gravitational force models, specially in cross-track direction, can be further improved. The estimated empirical accelerations do not show a significant mean value, which indicates that their estimation does not affect the estimation of the accelerometer bias parameter. Table 5.7 summarizes the mean and standard deviation of the empirical accelerations for CHAMP and GRACE A (for the year 2003), for the case with constant scale factors. The difference in magnitude of the empirical accelerations between the two spacecraft is clearly visible. Also the statistical information of the empirical accelerations for the standard reduced dynamic technique for GRACE A is included at the bottom of the table. This illustrates again a larger variation in along-track direction and almost no difference in cross-track direction. The formal errors of the empirical accelerations are about 4.97, 8.5 and 9 nm/s^2 in radial, along-track and cross-track direction for GRACE B, which indicates that these parameters are dominated by the constraints.

To check the influence of estimating empirical accelerations, a test is done without them, for CHAMP and GRACE A during the same period (2003), where only the initial state vector and bias and scale factors in three directions are estimated, with the scale factors tightly constrained. The resulting calibration parameters are

	CHAMP	GRACE A
S_X [-]	0.84 ± 0.03	0.96 ± 0.015
S_Y [-]	0.52 ± 0.19	0.95 ± 0.093
S_Z [-]	1.05 ± 0.38	0.95 ± 0.047
B_X [nm/s^2]	-2964 ± 95	-1113 ± 22
B_Y [nm/s^2]	135 ± 68	26948 ± 2644
B_Z [nm/s^2]	11 ± 61	-504 ± 26

Table 5.8 Calibration parameters for CHAMP and GRACE A without estimating empirical accelerations (2003)

presented in Table 5.8. The values in X-direction show little variation compared to the case including empirical accelerations, which are the advertised values of 0.83 and 0.96 for CHAMP and GRACE A, where the parameters in Y- and Z-direction show a larger variation. In the case of CHAMP this variation becomes high. The resulting orbit precision with respect to reference orbits now amounts to about 10 cm for GRACE orbits and around 30 cm for CHAMP orbits. All this supports the difference in magnitude of the estimated empirical accelerations presented in Table 5.7, and consequently the fact that maneuvers, which occur frequently, are not included in the CHAMP accelerometer data.

5.5.2 The variation of the arc length

The length of the arc over which observations are used also has an influence on the estimated parameters. A shorter arc has less observations available to determine the solution, but has a smaller effect of force model errors, which build up over time. The opposite holds for a longer arc. Three tests with different arc lengths are conducted with CHAMP data for the second half of 2003 (DOY 200-365): an arc length of half a day, 2 days, and equal to an integer number of orbital revolutions closest to a full day. The last test resulted in no significant differences in estimated scale and bias parameters compared to the standard one day processing. An arc length equal to half a day or two days has a bigger impact on the calibration parameters. The tests are compared in Table 5.9. A shorter arc results in a larger deviation in X-direction, and a smaller deviation for a longer arc, where also the formal errors get smaller. On the other hand systematic errors have a higher impact for a longer arc. In Y direction, the estimated scale factor deviates less from the a priori value for a short arc, where for a longer arc the estimated value deviates more from the a priori scale factor values. As described in the introduction, the calibrated accelerations were used in [*Doornbos et al.*, 2009] for thermospheric density and wind modeling. During this study, wind speed calculations for the CHAMP satellite, derived from the accelerometer measurements, suggested a lower cross-track scale factor than the advertised values. Together with the (slightly) more stable estimation in X-direction this pleads in favor of the longer arc estimation.

	1/2 day	1 day	2 days
S_X [-]	0.85 ± 0.03	0.85 ± 0.02	0.85± 0.02
S_Y [-]	0.83 ± 0.02	0.78 ± 0.03	0.73 ± 0.05
S_Z [-]	1.0	1.0	1.0
B_X [nm/s^2]	-2979 ± 84	-2982 ± 75	-2980 ± 62
B_Y [nm/s^2]	239 ± 18	225 ± 18	208 ± 20
B_Z [nm/s^2]	9 ± 5	7 ± 5	4 ± 4

Table 5.9 Calibration parameters for varying orbit arc lengths (CHAMP)

However, because of the small impact in flight direction, the remaining uncertainty in cross-track direction and the longer run-time, this approach is not applied to a larger data set. In the stacked normal approach however, which is discussed at the end of this chapter, one scale factor is estimated for a longer period based on a multi-arc technique.

5.6 Orbit quality analysis

The quality of the orbits can be assessed by a comparison with externally computed orbits. For the GRACE satellites these are determined by the Jet Propulsion Laboratory (JPL), using the reduced-dynamic technique (without accelerometer data) [*Case et al.*, 2002], which have a claimed accuracy of better than half a decimeter. This is confirmed by computing SLR residuals, which are included for the GRACE B JPL orbits in Table 5.10. The SLR observations were not used to compute the orbits.

Figure 5.10 shows the 3D RMS values with respect to the reference orbits for the 5 year period analyzed, where the total RMS amounts to 3.42 cm for GRACE B and 3.68 cm for GRACE A. The first half of 2003 has higher RMS values, which is due to the absence of high-rate GPS satellite clock information, which the Center for Orbit Determination (CODE) in Bern, Switzerland, started producing from mid 2003 on.

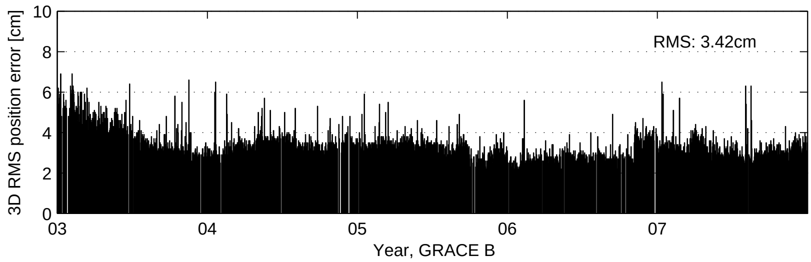

Figure 5.10 3D RMS of the GRACE B orbits with respect to the JPL reference trajectories

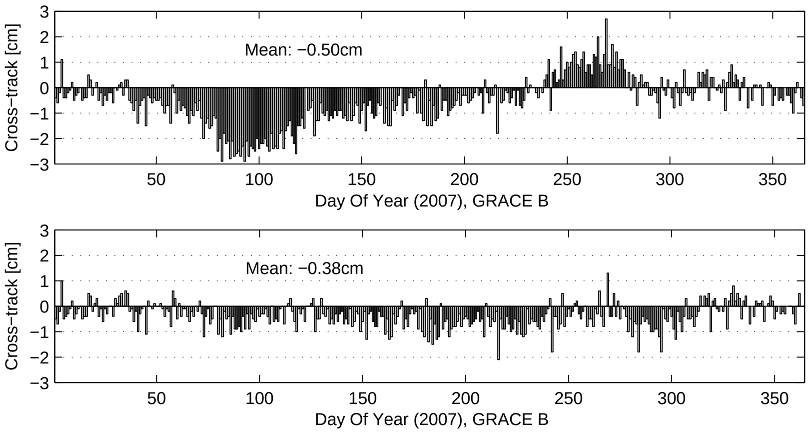

Figure 5.11 Cross-track mean offsets of the 2007 GRACE B orbits with respect to JPL reference trajectories, with different a priori bias values (top: determined with the GHOST models, bottom: determined with the more accurate models, see chapter 3)

Before that time, IGS 5 minute clock products were interpolated. Figure 5.11 shows the mean cross-track offset of GRACE B orbits for the year 2007, obtained with different sets of a priori bias values, where in the bottom figure the more accurate non-gravitational force models, described in section 5.4, are applied. This cross-track offset shows a pattern which follows β-prime, the angle between the orbital plane and the sun vector, and was already observed in [*Kroes*, 2006], where solar radiation pressure mismodeling was the prime suspect for this behavior. Now this can be attributed with certainty, as a test with a priori bias values based on more accurate force models removes the pattern from the mean cross-track offset. As stated in the previous section, the bias in Y-direction (cross-track) is tightly constrained to the a priori value, derived from the mean value of the modeled non-gravitational forces in the GHOST software, which is a simple canonball solar radiation pressure model.

From Figure 5.9 it is clear that this model is inaccurate when the angle between orbital plane and sun vector increases. All this indicates that the estimation of dynamic parameters from GPS observations in cross-track direction lacks sensitivity, as the bias can not be estimated reliably and the empirical accelerations in this direction do not counteract the mismodeling properly.

The SLR residual statistics for all satellites are summarized in Table 5.10. The values for GRACE B are somewhat smaller than for GRACE A, and the CHAMP residuals are slightly higher. The mean offset can partly be attributed to the absence of albedo modeling in the GHOST software, as the mean offset for the 2007 test of GRACE B with different a priori bias values shows a reduction from -0.43 cm to -0.25 cm. The residuals of the JPL orbits for GRACE A and B, and of two

	Mean [cm]	RMS [cm]	# points
GRACE A	-0.83	2.33	163850
GRACE A (JPL orbits)	-1.13	2.40	166944
GRACE B	-0.56	2.15	154176
GRACE B (JPL orbits)	-0.87	2.17	158251
CHAMP	-0.54	2.80	167012
CHAMP (DEOS orbits, 03-04)	-1.04	3.26	68430

Table 5.10 SLR residual statistics for the 5 year period (2003-2007)

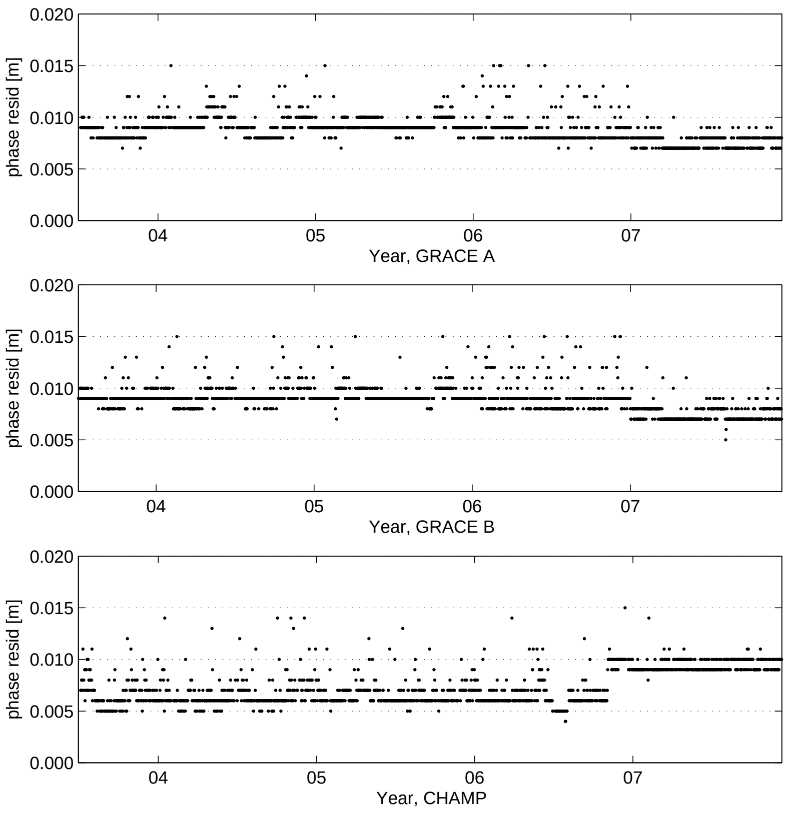

Figure 5.12 Daily RMS of phase residuals of the ionospheric free combination for the GRACE satellites and CHAMP

years of DEOS orbits for CHAMP are also included in the table, to demonstrate that all the orbits have a similar quality, where the GHOST computed orbits seem to be slightly more precise, which might be due to the fact that the same software (GHOST) was used to compute the SLR residuals.

Another indication for the quality of the estimated orbits are the phase residuals.

These are plotted in Figure 5.12, where the distinct lines are due to a 3 digit output of the values (1 mm round-off). The residuals for GRACE fluctuate around 9 mm. The scatter increases in 2006. From the end of 2006, an improvement is visible, which can be attributed to the incorporation of nominal phase center variations [*Montenbruck et al.*, 2008*a*], after the adoption of absolute phase centers by the IGS. The CHAMP residuals are consistent over the period until the end of 2006, where the values increase. A possible explanation can be that the same phase center variations were used as for the GRACE satellites, without changing the antenna center offset. The increase in phase residual values indicates that when applying phase center variations for CHAMP, a different offset should be used. The applied phase center offsets used amount to 0.0, 0.0 and -0.414 m for the GRACE satellites in the SBF and -1.488, 0.0 and -0.393 for the CHAMP satellite.

A last means to check the quality of the GRACE orbits is a comparison with the K-band range (KBR) measurements. To this end, KBR residuals are plotted for the whole period in Figure 5.13. No significant improvement in KBR fit is observed when using accelerometer measurements. The presented residuals show a strong correlation with the β-prime angle. This pattern also shows up when the a priori bias values based on more accurate non-gravitational force models are used and with standard reduced-dynamic orbits determined without accelerometer data. The mean RMS value of 1.7 cm is in agreement with the KBR residuals of the JPL reference trajectories, which show a smaller variation (3 mm in stead of 5 mm), and no periodic pattern. The outliers in the first half of 2004 are present in both sequences. The observed pattern is also visible in KBR residuals presented in [*Jäggi et al.*, 2009] and a probable cause is the use of observations of eclipsing Block IIA satellites (A. Jäggi, priv. comm., 2010). These Block IIA satellites have

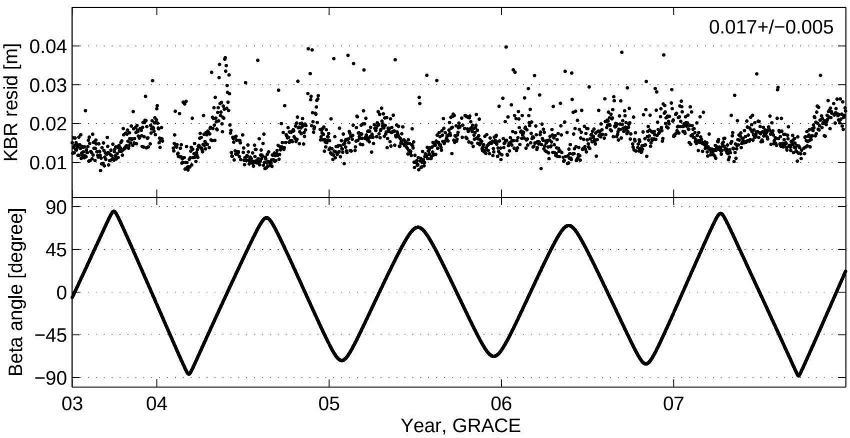

Figure 5.13 GRACE KBR range residuals (daily RMS) and β-prime angle

horizontal antenna offsets and introduce systematic errors in the LEO orbits due to the GPS satellite attitude motion during eclipse phases and after shadow exit.

5.7 Stacked normal matrices approach

An additional method is implemented as well, where one scale factor is estimated for a longer period (here one year). This multi-arc method has the benefit that all observations taken during this period are used for one estimate of the scale factor which gives the best consistency over the whole period. In this manner, days with a stronger signal contribute more to the solution than days with a lower accelerometer signal level.

First, the bias parameters are determined by the nominal daily estimation technique where the scale factor is kept fixed (section 5.3.2), after which the part of the normal matrix related to the scale factors, without constraints, is stored and stacked for the defined period. After stacking, one scale factor is determined in each direction for the whole period. The precise implementation is described next, followed by a discussion of the results.

5.7.1 Method and implementation

After convergence of the bias parameters, with the scale factors fixed at the predefined values listed in Table 5.3, the normal equations are partitioned. The part for the scale factors, $\mathbf{x}_2$, is unconstrained. The part indicated by $\mathbf{x}_1$ contains all other parameters (state, bias parameters and GPS receiver clock and ambiguities). In this approach no empirical accelerations are estimated.

$$\begin{pmatrix} \mathbf{N}_{11} & \mathbf{N}_{12} \\ \mathbf{N}_{21} & \mathbf{N}_{22} \end{pmatrix} \begin{pmatrix} \mathbf{x}_1 \\ \mathbf{x}_2 \end{pmatrix} = \begin{pmatrix} \mathbf{b}_1 \\ \mathbf{b}_2 \end{pmatrix} \tag{5.1}$$

The three-dimensional vector containing the scale factors can be factored out, resulting in:

$$(\mathbf{N}_{22} - \mathbf{N}_{21}\mathbf{N}_{11}^{-1}\mathbf{N}_{12})\mathbf{x}_2 = (\mathbf{b}_2 - \mathbf{N}_{21}\mathbf{N}_{11}^{-1}\mathbf{b}_1) \tag{5.2}$$

The left and right hand sides of this equation are subsequently stored for each day and summed up, according to:

$$\sum_{i=1}^{nday} \mathbf{N}_i \mathbf{x}_{SF} = \sum_{i=1}^{nday} \mathbf{r}_i \tag{5.3}$$

	GRACE B			CHAMP		
	ΔS_x	ΔS_y	ΔS_z	ΔS_x	ΔS_y	ΔS_z
2004	-0.014	-0.066	0.028	0.010	-0.040	-0.183
2005	-0.015	-0.109	0.067	0.011	-0.026	-0.105
2006	-0.012	-0.125	0.059	0.013	-0.032	-0.096
2007	-0.014	-0.059	0.042	0.011	-0.032	-0.186

Table 5.11 Corrections to the scale factors for a one year period for the GRACE B and CHAMP satellites

after which one set of scale factors can be determined for the whole period, with $nday$ the number of days (or e.g orbital arcs).

5.7.2 Results

With the stacked normal matrices approach, one set of accelerometer scale factors is obtained. The corrections to the a priori scale factors for one year periods for GRACE B and CHAMP are summarized in Table 5.11, for the years 2004 to 2007. From these values it is clear that especially in flight direction, the determined scale factor is extremely stable, which supports the assumption that the scale factor in reality is constant. The small negative correction of about 0.014 in X-direction to the advertised value of 0.96, agrees with the value found in section 5.3.1, where the scale factor was estimated as a daily value and averaged afterwards, resulting in a value of 0.95. In Y-direction, the corrections are larger, while the variations are relatively small. These values however are considerably smaller than when computed with the standard technique described above, where daily values are computed. A test during the period DOY 270-300 in 2003 with an unconstrained daily estimation of the scale factor (and a constrained bias in Y- and Z-direction) resulted in variations of the scale of 0.01, 0.15 and 0.45 in the respective SBF-directions.

Applying a higher order gravity field model, a different ocean tides model or the modeled non-gravitational accelerations in the a priori bias determination, did not result in smaller variations, which suggests that the low accelerometer signal in this direction is probably the cause for these values, and the larger variations over time.

The results in Z-direction, for GRACE B, also show a larger variation over time, caused by the small signal strength. However the variation is considerable smaller than the 30 day test described above or the completely unconstrained estimation presented in section 5.2. For CHAMP, modeled accelerations were used in this direction (and an a priori scale factor of 1), the corrections determined here indicate that these modeled accelerations are (scaled) too high.

Besides the values covering a long period, also the daily scale factor corrections offer some insight in the evolution over time of these parameters. The daily scale factor corrections for GRACE B in 2004 are presented in Figure 5.14. This figure

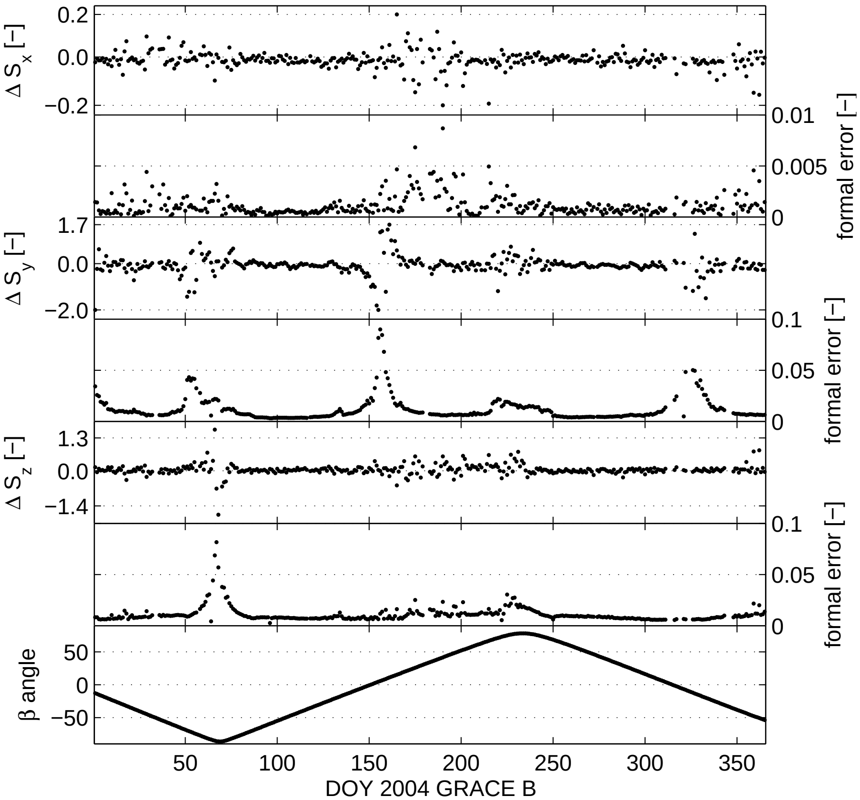

Figure 5.14 Daily corrections to the scale factor and the associated formal errors for GRACE B in 2004. At the bottom the β-angle is plotted

again shows that the estimation in X-direction has the highest certainty (a small formal error). Furthermore, when the β-angle becomes large, the formal error in all directions increases, and as a consequence the contribution of these values in the long period solution becomes smaller. In Y-direction, there are also large excursions when the β-angle crosses zero. In between these periods, in all directions the daily corrections to the scale factors remain more or less stable (note the different scale in the figures). This supports that the stacked matrices approach can be applied to determine the scale factor reliably, over a long period.

5.8 Validation

In this section, two methods are briefly outlined that validate with independent data the calibration parameter results presented in this chapter. For CHAMP, a first validation was already given with the discussion of the bias and instrument events plotted in Figure 5.6. The two methods described here are a comparison of the calibrated accelerations with modeled non-gravitational accelerations, and second the retrieval of thermosphere density and winds from the calibrated accelerometer measurements.

5.8.1 Comparison with non-gravitational force models

For this validation method, the calibrated measurements are compared with the non-gravitational (and empirical) accelerations as modeled in the GHOST software, which is discussed in section 3.2. The correlation coefficient ρ is determined between the calibrated (x) and modeled accelerations (y) in radial, along track and normal direction (both in this reference system), according to:

$$\rho = \frac{\sum_{i=1}^{n}(x_i - \bar{x})(y_i - \bar{y})}{\sqrt{\sum_{i=1}^{n}(x_i - \bar{x})^2}\sqrt{\sum_{i=1}^{n}(y_i - \bar{y})^2}} \tag{5.4}$$

with $\bar{x}$ and $\bar{y}$ the mean of the number n values.

This is illustrated for GRACE B for the second half of 2003 in Figure 5.15 and for CHAMP for the same period in Figure 5.16.

For GRACE B, the mean value of the correlation coefficients is 0.88 in radial direction, 0.94 in along-track and 0.85 in cross-track direction. For GRACE A similar values are found. These numbers reflect the quality of the determined calibration parameters and the applied force models. The higher value in along-track direction supports the result that the estimation of the calibration parameters and empirical accelerations in this direction, using the respective techniques, is the best determined. Days with a decreasing value have in most cases attitude maneuvers experienced by spacecraft, which is clearly visible in cross-track direction. These maneuvers are measured by the GRACE accelerometer, but not picked up by the empirical accelerations. The values in radial direction between DOY 260 and 290 are lower. A possible explanation is that during that period the satellite was in eclipse free conditions, resulting in a larger albedo force acting on the satellite, which is not modeled in the GHOST software.

For CHAMP, the comparison in radial direction can not be done because of the malfunctioning of the accelerometer in Z-direction. The other directions show a good agreement, where the cross-track mean value is higher compared to GRACE. This is because in the CHAMP accelerometer data the manoeuvers are excluded in the pre-processing, which is beneficial when comparing force models and ac-

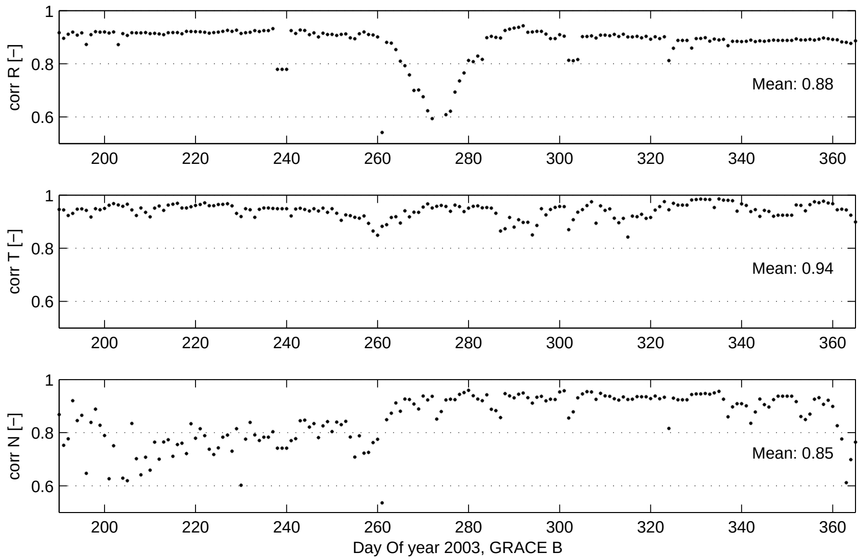

Figure 5.15 Correlation coefficient between GRACE B calibrated accelerometer measurements and modeled non-gravitational (and empirical) accelerations in the GHOST software

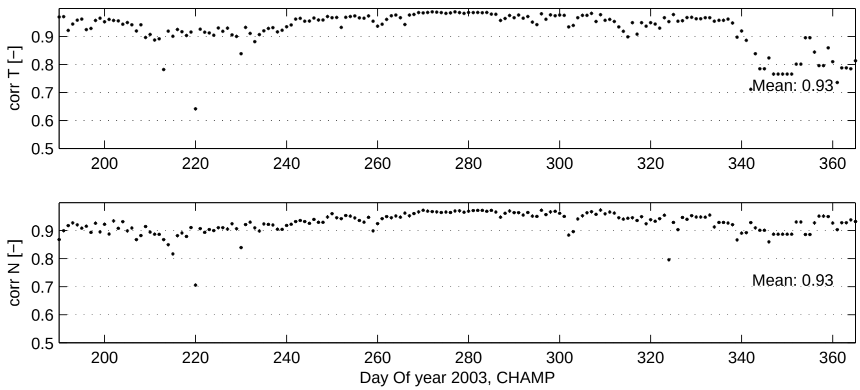

Figure 5.16 Correlation coefficient between CHAMP calibrated accelerometer measurements and modeled non-gravitational (and empirical) accelerations by the GHOST software

celerometer measurements. At the end of the period, the GPS and attitude data are of lower quality (lots of gaps), which is reflected in the lower agreement.

5.8.2 Density retrieved from accelerometer measurements

As mentioned earlier, the retrieval of thermosphere density and winds [*Doornbos et al.*, 2009] was a driver for the research presented here. The purpose of the study was to investigate the optimal derivation, calibration and use of density and wind data derived from the combination of instruments on CHAMP, GRACE, Swarm and other (future) accelerometer missions. The processing methodology and the results of the study can be found in the final report [*Doornbos et al.*, 2009].

The calibration parameters presented in section 5.3.2 were applied in the study. A statistical comparison of the retrieved density and empirical models resulted in mean offsets of the data/model ratios deviating up to around 30% and standard deviations between about 15% and 30% for CHAMP and between about 24% and 45% for GRACE which is consistent with the expected quality of the underlying models. Also the consistency of the retrieved densities with the calibrated HASDM model, based on contemporaneous satellite data, is better compared to the empirical models, which proves that the calibration of the accelerometer measurements as done in this research helps. The better agreement for the CHAMP derived densities probably stems from the lower flying altitude, as errors in calibration and solar radiation modeling are relatively smaller with respect to the higher density at the lower altitude, compared to GRACE.

Furthermore, the outcome of the study helped to formulate recommendations for the Swarm mission (also equipped with accelerometers), to enhance the retrieval of thermospheric density and winds from this future data set. Current and future accelerometer missions will provide together a level of temporal and spatial detail on density variations in the thermosphere, which is beyond the capabilities of existing global models.

Chapter 6

Processing of GOCE data

Results presented in the previous chapters were all stemming from data of satellites flying already some time in orbit (CHAMP was launched in 2000, GRACE in 2002), meaning that the data are well known and extensively researched. In this chapter, results of the relatively recently (March 2009) launched GOCE satellite are presented. GOCE is the first of ESA's core Earth explorer missions, measuring the Earth gravity field with unpreceded precision by applying the gradiometer technique for the first time in space. GOCE differs from the CHAMP and GRACE missions on different levels. The flying altitude of GOCE is much lower, resulting in higher aerodynamic forces acting on the satellite, which are compensated by the drag-free control system, resulting in a small net acceleration in along-track direction. Furthermore the satellite experiences a yaw motion, caused by the aerodynamic torques (the spacecraft has its nose in the wind) and stabilized by magnetic torquers, where the attitude of CHAMP and GRACE is steered according to the flight direction and Earth pointing and kept within a narrow band. Finally the gradiometer, consisting of six accelerometers with the common-mode accelerations used to represent the non-gravitational accelerations (explained in section 6.3), is the biggest difference, compared to the single accelerometers on board CHAMP and GRACE. All this makes it interesting to test the developed accelerometer calibration method on the GOCE data, which is done in this chapter.

In the first section an overview of the satellite is presented, describing the main scientific instruments and the High-level Processing Facility (HPF), which processes the Level 1 data to Level 2 products. In section 6.2 the results of GOCE precise orbit determination are discussed. In the last section of this chapter, the calibration of the common-mode accelerations by including them in the precise orbit determination is discussed, covering three cases. First, the case when the satellite is not yet in drag-free mode is analyzed, which is the most similar to the CHAMP and GRACE accelerometer calibration, because the drag-free control is not active and the accelerometer measurements give the total uncompensated non-gravitational accelerations experienced by the spacecraft. The second case deals with the satellite flying in drag-free mode, which is the operational mode. In this case, there is only a small acceleration signal in along-track direction, which is expected to make the determination of the scale factor in this direction difficult. A last case analyses a day with manoeuvers, which are also measured by the accelerometers. After establishing the baseline calibration setup for GOCE, two months of data are analyzed, covering periods before and after drag-free activation.

6.1 Satellite overview and data processing

The overview presented in this section is a summary of the more detailed introduction of the GOCE mission in [*Drinkwater et al.*, 2003]. The mission was selected for phase A development in 1996 with an expected launch date in 2006. The gradiometer measurement principle was already long before introduced, and well analyzed in preparatory studies for GOCE's predecessor mission concepts SESAME and ARISTOTELES. The GOCE satellite was built by an industrial consortium led by Thales Alenia Space (Turin, Italy), and eventually launched on March 17 in 2009 from Plezetsk, Russia with a Rockot launcher with a Breeze upper stage. The nominal measurement altitude is 254 km and the satellite flies in a dawn-dusk sun-synchronous orbit with an inclination of 96.7°.

The primary mission objectives are to determine the Earth's gravity field with an accuracy of 1 mGal ($10^{-5}m/s^2$) and determine the geoid, the equipotential surface for a hypothetical ocean at rest, with an accuracy of 1 cm, both achieved at length scales down to 100 km. These objectives serve scientific research in oceanography, solid Earth physics, geodesy and glaciology, all enhancing the understanding of the Earth interior and the climate system.

The main instrument on board of GOCE is the electrostatic gravity gradiometer, measuring the components of the gravity-gradient tensor. It is designed and developed by ONERA (Châtillon, France) and consists of three pairs of three-axes servo-controlled capacitive accelerometers mounted on an ultra-stable carbon structure. The accelerometers have a design measurement bandwidth (MBW) of 5x10^{-3} to $10^{-1}Hz$ and a noise level in the MBW of $10^{-12}m/s^2Hz^{-1/2}$ for the most sensitive axes (2 out of 3 for each accelerometer). A pair of accelerometers is mounted on a platform 50 cm apart, forming a gradiometer arm. Three identical arms are mounted orthogonally to one another. The difference between the accelerations measured by each of the arm's accelerometers provides the gradiometric measurement, half the sum of each pair forms the common-mode measurement, the non-gravitational accelerations acting on the spacecraft (Figure 6.1).

A second indispensable instrument is the Satellite to Satellite Tracking Instrument (SSTI), the Lagrange GPS receiver, which was newly developed by Laben for this mission. It is a dual-frequency receiver connected to a helix antenna, capable of tracking 12 channels and delivering pseudorange and carrier phase measurements

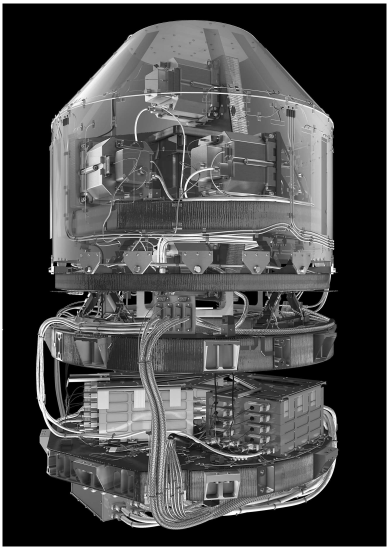

Figure 6.1 GOCE gradiometer, three accelerometers are visible at the top of the instrument, source: ESA - AOES Medialab

with a sampling rate of 1 Hz. The measurements are used for gravity field recovery in the SST-hl mode (explained in introductory section 1.1), thus complementing the gradiometer measurements. In addition, the SSTI data are used for precise orbit determination, real-time on board navigation and time tagging and precise geolocation of the gradiometer observations.

Another important instrument is the Ion Thruster Assembly (ITA), developed by QinetiQ (Farnborough, United Kingdom). This thruster has already flown on board the EURECA-1 and ARTEMIS spacecraft. However, the ITA on board of GOCE is an advanced development and can provide variable thrust levels. It is coupled with the common-mode gradiometer measurements to enable a drag-free control of the satellite. Furthermore the spacecraft carries a Laser Retro Refractor for SLR observations, and three star camera's for precise attitude determination, with two always observing simultaneously.

The raw instrument data stemming from the instruments described above are processed by the Payload Data Segment (PDS) located at ESRIN (Frascati, Italy). The PDS is responsible for the mission performance assessment, the calibration and verification of the measurements and monitoring of the performance of the space and ground segment.

The level 1 data are processed to level 2 products by the High-level Processing Facility (HPF) [*Koop et al.*, 2006], operated by the European GOCE Gravity-

Consortium (EGG-C). EGG-C is a group consisting of the following ten European institutes:

- Astronomical Institute of the University of Bern (AIUB), Switzerland
- Centre d'Etudes Spatiales (CNES), Toulouse, France
- Astrodynamics and Space Missions (AS), Faculty of Aerospace Engineering, Delft, The Netherlands
- Helmhotz Center Potsdam (GFZ), Germany
- Institute for Astronomical and Physical Geodesy (IAPG), Technical University of Munich, Germany
- Institute for Theoretical Geodesy (ITG), University of Bonn, Germany
- Politechnico di Milano (POLIMI), Italy
- National Institute for Space Research (SRON), Utrecht, The Netherlands
- Institute of Navigation and Satellite Geodesy, University of Technology (TUG), Graz, Austria
- Department of Geophysics, University of Copenhagen (UCPH), Denmark

HPF tasks comprise the pre-processing, external calibration and validation of the level 1b data and the determination of quick-look and precise level 2 orbit and gravity field products. IAPG hosts the principal investigator and HPF management. The latter is done together with SRON, which also hosts the Central Processing Facility (CPF), responsible for the scientific pre-processing and distribution of the data. Rapid GOCE science orbits (RSO) with a 1 day latency are determined at AS, while AIUB provides the precise science orbits (PSO, latency of 2 weeks) [*Visser et al.*, 2008]. Results of the orbit determination are presented in the next section. For gravity field processing three techniques are implemented: the classical direct method based on orbit perturbation theory for the GPS STT observations (GFZ, CNES), the time-wise approach, based on an epoch-wise processing of the SST and gradiometer observations (TUG, ITG) and the space-wise method, where the data are interpreted as gravity functional of location in space (POLIMI, UCPH). A final step is the validation of the gravity field products by internal and external comparison with independent data sets (IAPG, AS).

6.2 Kinematic and reduced dynamic POD results

The auxiliary products used to generate the results presented in this section are identical to the ones used in the processing of the GOCE RSO kinematic orbits: rapid CODE GPS ephemeris with high-rate (5 second) clock products and rapid Earth orientation parameters. The applied GPS antenna offsets are 0.6944, -0.0069 and -1.1697 m in the spacecraft body frame, defined with the X-axis aligned with the long axis of the satellite, the Z-axis perpendicular to the X-axis and zenith pointing, and the Y-axis completing a right-handed orthonormal frame. The GOCE satellite is not perfectly Earth pointing, as the attitude changes because of aerodynamic torques and because of torques induced by magneto-torquers, resulting in yaw, roll and pitch angles of a few degrees. In the orbit determination an empirically derived phase center variation (PCV) map is applied, as described in [*Jäggi et al.*, 2009] and generated by AIUB in the framework of the PSO processing.

In the framework of the HPF-processing chain, the kinematic RSO products are generated daily with a latency of 1 day. Measurement weight values are set to 2 cm for the phase observations (to capture noise and systematic effects) and 6 m for the code measurements (the code observations serve to stabilize the solution as explained in section 4.4).

Thanks to the quality of the applied rapid GPS ephemeris and clock products, generated by the CODE IGS analysis center of the AIUB, a precision of around 3.8 cm (3D) is achieved compared to the reduced dynamic precise science orbits, also produced at AIUB [*Bock et al.*, 2007]. Because of the high quality of these rapid products, no re-computation was done with the final IGS products. In Table 6.1 the statistics of the fit of the kinematic RSO products are listed for a ten day period. No systematic offset is present and the standard deviation varies from about 2.6 cm in radial direction to 1.5 cm in cross-track direction.

Next to the kinematic orbits also reduced dynamic orbits are computed with the GHOST software for this period, using the same CODE ephemeris and clock products and observations weights as described above. The gravity field model applied is the EIGEN-5S model [*Foerste et al.*, 2008] to degree and order 120, and no drag and solar radiation coefficients are estimated (the satellite is in operational mode during this period, thus flying drag-free). The standard deviation of the empirical accelerations is set to 20 nm/s^2 in radial direction and 50 nm/s^2 in tangential and normal direction. The statistics of the fit of the reduced dynamic orbits with the PSO products is given in Table 6.2. The 3D RMS is about 2.4 cm, with no clear offset in any direction. The standard deviation varies between 1.0 cm and 1.6 cm in all directions. The estimated empirical accelerations have a mean and variation of 60 $nm/s^2 \pm 50$ in radial direction (with a formal error of 15 nm/s^2) , -2 $nm/s^2 \pm$ 40 in tangential direction (10 nm/s^2 formal error) and -100 $nm/s^2 \pm 100$ in normal direction (10 nm/s^2 formal error). As expected, the largest acceleration is working in normal direction and includes the effect of direct solar radiation pressure (GOCE is flying in a sun-synchronous dawn-dusk orbit).

	mean			stand dev			RMS
	R [cm]	T [cm]	N [cm]	R [cm]	T [cm]	N [cm]	3D [cm]
20	0.1	0.6	-0.9	3.8	2.5	2.2	5.2
21	0.2	0.4	-0.7	2.4	1.8	1.7	3.6
22	0.2	0.6	-0.6	3.4	2.6	1.5	4.6
23	0.0	0.4	-0.6	2.8	2.4	1.8	4.2
24	0.0	0.3	-0.9	2.1	1.8	1.7	3.4
25	-0.1	0.4	-0.3	2.1	1.9	1.1	3.1
26	-0.2	0.5	-0.1	2.5	2.1	1.4	3.5
27	-0.1	0.5	-0.3	2.3	1.7	1.1	3.1
28	0.5	-0.6	1.4	2.5	1.9	1.6	3.9
29	0.7	-0.8	1.2	2.2	2.0	1.3	3.6
mean	0.1	0.2	-0.2	2.6	2.1	1.5	3.8

Table 6.1 Orbit fit statistics in the RTN-frame (mean, standard deviation and root-mean square of the position differences) of GHOST kinematic RSO products compared to AIUB reduced dynamic precise science orbits, for the period DOY 20-29 2010.

	mean			stand dev			RMS
	R [cm]	T [cm]	N [cm]	R [cm]	T [cm]	N [cm]	3D [cm]
20	0.3	0.5	-0.1	1.0	1.3	1.1	2.1
21	0.3	0.4	0.0	1.5	1.4	1.1	2.4
22	0.2	0.5	0.0	1.3	1.3	1.3	2.4
23	0.1	0.7	0.5	1.0	1.5	1.0	2.3
24	0.1	0.4	0.0	1.0	1.4	0.9	2.0
25	0.1	0.4	0.1	1.1	1.5	1.0	2.1
26	0.2	0.8	0.8	1.2	1.9	1.2	2.8
27	0.1	0.5	0.0	1.2	1.3	0.8	2.0
28	0.7	-0.7	1.8	1.3	1.4	1.1	3.0
29	0.8	-0.9	1.6	1.1	1.6	0.8	2.9
mean	0.3	0.3	0.5	1.2	1.5	1.0	2.4

Table 6.2 Orbit fit statistics in the RTN-frame (mean, standard deviation and root-mean square of the position differences) of GHOST reduced dynamic orbits compared to AIUB reduced dynamic precise science orbits, for the period DOY 20-29 2010.

6.3 Calibration of the common-mode accelerations by POD

Although on board of GOCE the non-gravitational forces acting on the spacecraft are measured as well, this mission differs greatly from the CHAMP and GRACE missions. First the flight altitude is considerably lower, around 250 km for GOCE compared to an initial altitude of 485 km for GRACE and 454 km for CHAMP. This results in larger aerodynamics forces acting on the spacecraft, as atmospheric density decreases exponentially with altitude. The aerodynamic accelerations experienced by GOCE are compensated by the ion engine thrust, thus nominally the satellite is flying in a drag-free mode, resulting in a small (non-gravitational acceleration) signal in along-track direction. The drag-free control especially compensates atmospheric drag in the along-track direction and causes parasitic accelerations in the radial and cross-track direction. Another difference is the gradiometer measurement principle and the combination of accelerometer measurements.

With the center of the gradiometer almost coinciding with the GOCE center of mass (the c.o.m. offset is around a few cm), the common-mode accelerations are defined as half of the sum of two accelerometers along a gradiometer arm and closely represent the non-gravitational accelerations experienced by the spacecraft including the propulsive acceleration of the ion engine. The accelerations observed by the i-th accelerometer (with i = 1 to 6) can be written as [*Visser*, 2008]:

$$\boldsymbol{a}_{obs,i} = \boldsymbol{S}_i[\boldsymbol{M}_i(\boldsymbol{\Gamma} + \boldsymbol{R})\boldsymbol{x}_i + \boldsymbol{a}_{non-grav}] + \boldsymbol{b}_i + \epsilon_i \tag{6.1}$$

with $\boldsymbol{S}_i$ the diagonal matrix of accelerometer scale factors (along the three accelerometer axes) and $\boldsymbol{M}_i$ the accelerometer orientation matrix in the Gradiometer Reference Frame (GRF). Ideally $\boldsymbol{M}_i$ is the identity matrix, but includes possible misalignments. These misalignments are due to instrument imperfections and are represented by rotations around the individual accelerometer axes. It is assumed that these errors are small, and in the following, they are ignored. $\boldsymbol{\Gamma}$ is the gravity gradient matrix containing the second order derivatives of the gravity field potential at the satellite location. The matrix $\boldsymbol{R}$ contains the rotational terms, consisting of centrifugal accelerations and angular acceleration rates around the accelerometer axis, the effect of taking measurements in a moving reference system (fixed to the satellite). $\boldsymbol{a}_{non-grav}$ contains the non-gravitational accelerations working on the spacecraft, which are the combination of the accelerations due to non-gravitational forces including thruster firing. $\boldsymbol{b}_i$ represents the accelerometer bias and ϵ_i the observation noise for the three accelerometer axes. Finally, $\boldsymbol{x}_i$ is the vector containing the coordinates of the accelerometer with respect to the spacecraft center of mass in the GRF. Besides the misalignment errors mentioned above, the accelerometers are also affected by non-orthogonalities, coupling and quadratic terms [*Cesare and Catastini*, 2005]. These effects are all assumed to be corrected for by the in-flight calibration and neglected in the analysis described here.

Because the accelerometers are positioned symmetrical with respect to the center of the gradiometer and this center is located closely to the center of mass of the satellite, the gravity gradient and rotational terms cancel out when taking the sum of the observations of two accelerometers along a gradiometer arm, resulting in two times the non-gravitational accelerations $\boldsymbol{a}_{non-grav}$, and only one scale factor and bias for the combined accelerometer observations can be determined, which is a mix of the bias and scale factors for the two individual accelerometers. Half of this sum is defined as the common-mode acceleration and is a measure of the non-gravitational forces working on the spacecraft. Each common-mode combination has measurements along the three accelerometer axis, however, only the combination along the gradiometer arm where the two accelerometers are mounted on are considered here, which are per definition along the accelerometer most sensitive axes.

The common-mode accelerations introduced above are applied in the precise orbit determination, after proper transformations and as described earlier in chapter 4. It has to be noted that because of the attitude motion of the spacecraft, the SRF axes do not align perfectly with the radial, along-track and cross-track directions, as mentioned before. The analysis presented here covers three different cases: one when the drag-free control was not yet active, which resembles the most the CHAMP and GRACE situation, where GOCE experiences higher aerodynamic accelerations. Another case has the drag-free control active, which results in a small (non-gravitational acceleration) signal in along-track direction. The last case has manoeuvres executed by the spacecraft, which are also measured by the accelerometers. The empirical accelerations determined in a standard batch reduced dynamic orbit determination (with no drag or solar radiation coefficient estimated) and the common-mode accelerations are presented in Figure 6.2 for three days, representing the different cases. The radial direction is not included, because the acceleration signal in this direction is small (less than 30 $\mathrm{nm/s^2}$). The different parts of this figure are described in more detail in the following sections.

In the remainder of this chapter, the estimation of the calibration parameters for each case is described, where different approaches are followed. First the scale and bias parameters are estimated without constraints and without empirical accelerations. This results, as expected, in a weak estimation of the scale factor in Z-direction (because of the small signal). Next the scale factor is kept constant at 1.0 in the directions with a small signal (along the Z-axis in all cases and along the X-axis when in drag-free mode). The latter case is repeated with empirical accelerations estimated as well, to account for deficiencies in the applied gravitational force models. A final approach has the bias values in these directions fixed to a priori values, and the scale factor in all directions constant. The estimated calibration parameters and resulting orbit fit are grouped in Table 6.3 according to the approaches described here, to enable comparison between the different cases.

The test cases described earlier serve to establish a good setup to process two longer periods, presented in section 6.3.4. The calibration parameters for two different months are determined: July 2009, when GOCE was not yet flying drag free, and December 2009, when the drag-free mode was active. For these two months of data, also the multi-arc technique is applied, introduced at the end of the previous chapter.

6.3.1 Case with the drag-free mode not active

A day when GOCE was not flying in drag-free mode is July 7, 2009 (DOY 200), depicted in the upper part of Figure 6.2. The large acceleration in flight direction is immediately apparent and the estimated empirical accelerations agree well with the common-mode accelerations.

From the calibration parameters in Table 6.3 (top part) it can be concluded that the unconstrained estimation of a scale factor in Z-direction is unreliable. In the other two directions the scale parameter is close to one, indicating the measurements are properly calibrated. Constraining the scale in Z-direction (to a value of 1.0) has little effect on the other parameters. A bigger change occurs when empirical accelerations are estimated as well, where this can be explained by the fact that the estimation of the calibration parameters weakens because of the extra estimated parameters, which is also reflected by a higher formal error of these parameters (the formal error of the scale factor increases from less than 0.0001 to five times that value). The 3D RMS (compared to the reduced dynamic PSO) of about 5 cm in the latter approach is composed for a large part of a cross-track offset (up to 3 cm). This is similar to the results obtained for the CHAMP and GRACE calibration in cross-track direction, as described in the previous chapter and caused by correlations with the initial state.

Constraining the bias in Y- and Z-direction (to an a priori value obtained with the standard reduced dynamic technique, taking the mean of the empirical accelerations) results in a better fit and no offset. The values listed in the last column of Table 6.3 are obtained with a scale factor constant and equal to 1 in all directions. The standard deviation of the empirical accelerations is set to 3 nm/s^2 in each direction. The estimated accelerations amount to 0 nm/s^2 $\pm$ 13, -3 nm/s^2 $\pm$ 21 and -8 nm/s^2 $\pm$ 38 in radial, along-track and cross-track direction. The estimated values have a much higher variance than the a priori standard deviation, indicating that GOCE orbit resonances are probably not very well represented by the a priori gravity field model (EIGEN-5S) and thus improvements can be anticipated when GOCE gravity field models are used.

A higher value of the empirical acceleration standard deviation in cross-track direction (10 nm/s^2) resulted in a large offset of the empirical accelerations in this direction, of about 100 nm/s^2. When estimating one constant empirical acceleration in cross-track direction (the time interval τ set equal to 24 hours) and checking the correlations of the covariance matrix, a high correlation of this parameter with the state vector was found. In the case of CHAMP and GRACE such an offset was not observed. For GOCE the uncertainty of the force models (gravity) is larger than for CHAMP and GRACE and due to the high correlations between estimated parameters such errors have a strong impact. Consequently for GOCE a proper tuning of the empirical accelerations has to be applied.

6.3.2 Case with the drag-free mode active

In September 21, 2009, (DOY 264) GOCE was flying in drag-free mode, as is visible in the middle part of Figure 6.2. In along-track direction the common-mode signal is small, while the still present, albeit small empirical accelerations mainly account for deficiencies in the gravitational force models or residual non-gravitational accelerations.

In this case both the unconstrained estimation of the scale factor in X- and Z-direction is unreliable, as can bee seen in the middle part of Table 6.3. This also affects the estimation of the scale parameter in Y-direction, which deviates largely from 1. When constraining the scale factor in the former two directions, the situation does not improve. The scale in Y-direction still deviates largely from one, and above that, the orbit fit is about twice as bad compared to the unconstrained estimation approach. This can be explained by the fact that here, with the scale factors in X- and Z-direction constrained, no degree of freedom for force model deficiencies in these directions remains. In the previous case this was not observed, because there the scale factor in X- and Z-direction was able to vary. The drag-free control of GOCE is thus functioning very well, preventing a stable estimation of the scale factor in X-direction by POD.

Estimating empirical accelerations as well again results in an orbit fit mainly dominated by a cross-track offset (of -13.4 cm), and a small radial offset (of -1 cm). This improves again when constraining the bias in Y- and Z-direction to an a priori value, with a 3D RMS fit of 3.9 cm and no offsets.

6.3.3 Manoeuvres case

During September 18, 2009, (DOY 261) small manoeuvres were executed on GOCE by the ion thruster, which are visible in the accelerations in along-track direction in the bottom part of Figure 6.2 as a positive and negative offset after mid-day. The offsets differ by about 200 nm/s^2 equivalent to 0.2 mN steps of the ion thruster (the mass of GOCE is approximately 1000 kg).

Inspecting the estimated calibration values for this case in the bottom part of Table 6.3 reveals that in this case a scale factor in X-direction can be estimated freely. However, the scale parameter in Y-direction deviates largely from one. This does not improve when constraining the scale factor in Z-direction, and the resulting orbit fit is, as observed in the previous case, more than twice as high.

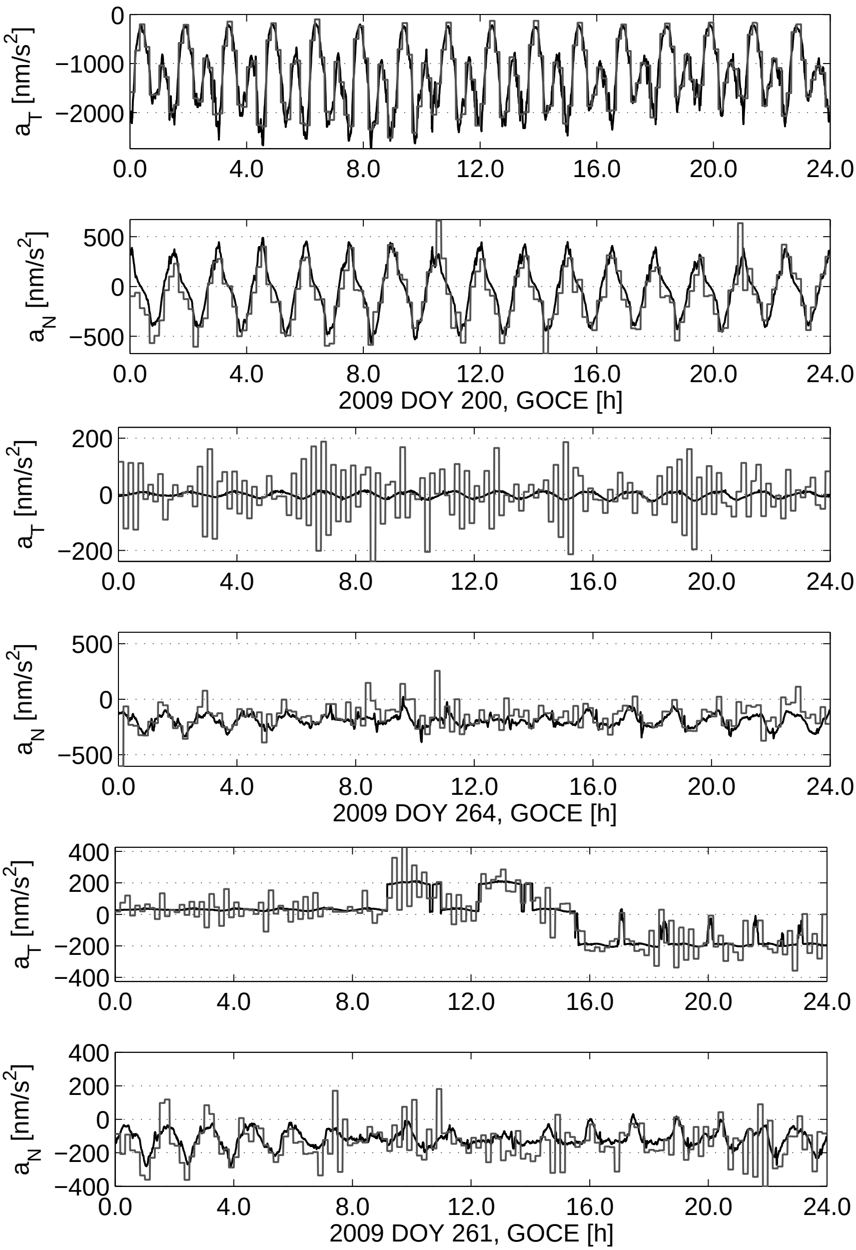

Figure 6.2 GOCE common-mode accelerations (black lines) and estimated empirical accelerations (gray lines) in along-track and cross-track direction for GOCE during DOY 200 (top, drag-free mode not active), DOY 264 (middle, drag-free mode active) and DOY 261 (bottom, manoeuvres) of 2009

DOY 200 drag-free off	no constraints	S_Z=1.0	S_Z=1.0, + emp accs	S=1.0, B=$B_{apriori}$, + emp accs
S_X [-]	1.020	1.020	1.038	1.0
S_Y [-]	1.025	1.023	1.021	1.0
S_Z [-]	2.12	1.0	1.0	1.0
B_X [nm/s^2]	-193	-193	-174	-210
B_Y [nm/s^2]	400	396	283	322
B_Z [nm/s^2]	1.2	19	-24	-22
3D RMS [cm]	24.7	25.5	5.3	4.3
DOY 264 drag-free on	no constraints	S_X=1.0, S_Z=1.0	S_X=1.0 S_Z=1.0, + emp accs	S=1.0, B=$B_{apriori}$, + emp accs
S_X [-]	-14.8	1.0	1.0	1.0
S_Y [-]	0.882	0.843	1.030	1.0
S_Z [-]	2.58	1.0	1.0	1.0
B_X [nm/s^2]	2756	-185	-183	-185
B_Y [nm/s^2]	162	179	104	295
B_Z [nm/s^2]	-119	-7.9	15	-50
3D RMS [cm]	19.9	44.5	14.2	3.9
DOY 261 manoeuvres	no constraints	S_Z=1.0	S_Z=1.0, + emp accs	S=1.0, B=$B_{apriori}$ + emp accs
S_X [-]	1.007	1.010	1.014	1.0
S_Y [-]	0.863	0.920	1.102	1.0
S_Z [-]	3.29	1.0	1.0	1.0
B_X [nm/s^2]	-187	-188	-186	-185
B_Y [nm/s^2]	233	291	160	321
B_Z [nm/s^2]	-58	-38	23	-40
3D RMS [cm]	24.6	56.4	13.3	3.4

Table 6.3 Scale and bias parameters for the GOCE common-mode accelerations in the gradiometer reference frame, for DOY 200, 261 and 264 in 2009. First results of a free estimation (no constraints and no empirical accelerations) are given, next S_Z is constant at 1.0 (and no empirical accelerations), then the same is repeated with empirical accelerations. When in drag-free mode (DOY 264), the second and third approach have S_X constant at 1.0 as well. Finally, the bias in radial and cross-track direction is constrained to a priori values, with the scale factor in each direction constant to 1.0. To indicate the orbit quality, the 3D RMS fit with respect to PSO reduced dynamic orbits is also provided.

Although the scale factor in X-direction is hardly constrained here, now the constant (manoeuvre) signal in this direction does not allow to account for any deficiencies (other than a constant offset) in X- and Z-direction.

When estimating empirical accelerations, again a large cross-track offset is observed, which disappears when constraining the bias in this direction to an a priori value.

6.3.4 Analysis of 2 months of data

To further asses the possibility to estimate stable common-mode calibration parameters, two one-month data sets are analyzed. These cover a period when the drag compensation was not yet active, July 2009, and one when GOCE was flying in drag-free-mode, December 2009. Three approaches are presented, first a purely dynamic estimation, where only 12 parameters are estimated each day. Then the same is repeated with a different gravity field model (GGM01S), to check the influence of gravity field model errors. Finally, the scale factors are kept fixed to one, the bias parameters (in Y- and Z-direction) are constrained to a priori values (obtained by a classic reduced dynamic technique) and empirical accelerations are estimated, which gives the best orbit fit (w.r.t PSO orbits). The calibration parameters for these data sets are grouped in Table 6.4. Finally, also the multi-arc technique is applied for these two months, and these results are presented at the end of this section.

Daily estimated parameters

The top part of the table corresponds to a period when GOCE was not flying drag-free (and still in commissioning phase), namely July 2009. Some days were excluded (DOY 183-184, 186-188, 202 and 209), because they showed gaps in the common-mode accelerations. Inspecting the values in the table of the unconstrained estimation (in X- and Y-direction) reveals that the estimated scale factors in these directions are quite stable, with respectively variations of 0.01 and 0.03. Because of the low altitude of GOCE, the influence of gravity field model errors is large, causing bigger variations in the estimated scale factor, especially in the Y-direction. The variation in X-direction is still small, only 0.02, when using an older gravity field model. When keeping the scale factor constant, the bias values differ a lot. This is explained by the fact that the total signal is much larger and in the first two approaches scale and bias parameters are anti-correlated.

The bottom part of the table corresponds to December 2009, with GOCE in science mode and flying drag-free. In this case the scale in X-direction is always kept constant at one, because of the small signal in this direction. The estimated scale in Y-direction is now smaller than one and also the variation is higher, up to 0.09. The signal in Y-direction in drag-free mode is about four times as small compared to the first case (the ion engine thrust also affects this direction), with an average signal

07/2009	(1)	(2)	(3)
S_X [-]	1.02 ± 0.01	1.03 ± 0.02	1.0
S_Y [-]	1.00 ± 0.03	1.05 ± 0.09	1.0
S_Z [-]	1.0	1.0	1.0
B_X [nm/s^2]	-191 ± 1	-188 ± 20	-210 ± 6
B_Y [nm/s^2]	378 ± 90	363 ± 105	311 ± 18
B_Z [nm/s^2]	-17 ± 145	172 ± 262	-21 ± 12
3D RMS [cm]	32	80	4.8
12/2009	(1)	(2)	(3)
S_X [-]	1.0	1.0	1.0
S_Y [-]	0.96 ± 0.09	0.96 ± 0.42	1.0
S_Z [-]	1.0	1.0	1.0
B_X [nm/s^2]	-184 ± 1	-183 ± 3	-184 ± 3
B_Y [nm/s^2]	304 ± 74	298 ± 244	299 ± 16
B_Z [nm/s^2]	-72 ± 118	-179 ± 308	-11 ± 9
3D RMS [cm]	35	107	4.7

Table 6.4 Scale and bias parameters for the GOCE common-mode accelerations in the gradiometer reference frame, for July 2009 (excluding DOY 183-184, 186-188, 202 and 209) and December 2009 (bottom of the table). First results of a free estimation are given, except with S_Z constant at 1.0 (1). Next a different gravity field model, GGM01S, is applied (2). Finally, the bias in radial and cross-track direction is constrained to a priori values, with the scale factor in each direction constant to 1.0 and empirical accelerations are estimated (3). The 3D RMS fit with respect to PSO reduced dynamic orbits is also provided.

strength of 75 nm/s^2 for this period compared to 300 nm/s^2 for July. Consequently the formal error of the estimated scale factor in Y-direction is also higher, consistent with a larger variation.

Inspecting the value of the bias in X-direction over the two periods (interval of 5 months) shows a difference of 26 nm/s^2 (for the approach (3), with constant scale factors). In the other two directions the change is smaller and it has to be noted that the bias in these 2 directions is more influenced by the a priori values. The last approach, keeping all scale factors constant and constraining the bias (in Y- and Z-direction) to a priori values results in both cases in good orbit fits w.r.t the PSO orbits, below 5 cm (3D).

Multi-arc technique

The two months analyzed in this section are also processed with the stacked matrices approach, introduced in section 5.7. The results are presented in Table 6.5 for periods of 3, 12 and 24 days, as deviations from the a priori value of 1. These results confirm that a multi-arc technique gives more stable results, as the variation of the parameter reduces with a longer period.

When not flying drag-free, the estimation (of the correction to the scale factor) in X-direction is stable, a correction of 0.026 is found. It seems that this is also possible when flying drag-free, as the correction amounts to 0.036. However it turned out that this value is driven by two days during which a manoeuvre took place (DOY 354 and 355). This is supported by the results of the shorter arcs, which show corrections of about 4 and 3. The estimation in Y-direction is stable during both periods, showing the smallest formal error (between brackets at the bottom part of the table). The estimation of the scale factor in Z-direction is unreliable, especially in July because of the small signal strength (on average only 9 nm/s^2) and also possibly because of the gravity model error. In December, it is twice as high (18 nm/s^2 on average), and this is reflected by the smaller correction and formal error.

Again, this illustrates the advantage of the multi-arc technique, where days with a stronger signal contribute more to the solution. In December, the 24 day solution in X-direction is driven largely by these two days with manoeuvres taking place. Excluding these days, the signal strength in X-direction when flying drag-free is too small (RMS about mean of only 2 nm/s^2) to allow a reliable estimation.

		July	December
3 days			
	S_X [-]	0.026 $\pm$ 0.012	4.1 $\pm$ 9.1
	S_Y [-]	0.004 $\pm$ 0.026	-0.04 $\pm$ 0.074
	S_Z [-]	-0.893 $\pm$ 0.623	-0.116 $\pm$ 0.18
12 days			
	S_X [-]	0.023 $\pm$ 0.009	3.25 $\pm$ 4.5
	S_Y [-]	0.014 $\pm$ 0.006	-0.037 $\pm$ 0.023
	S_Z [-]	-0.906 $\pm$ 0.33	-0.12 $\pm$ 0.053
24 days			
	S_X [-]	0.026 (0.0002)	0.036 (0.0026)
	S_Y [-]	0.014 (0.00007)	-0.039 (0.0004)
	S_Z [-]	-0.945 (0.025)	-0.145 (0.011)

Table 6.5 Corrections to the a priori scale factors (equal to one) of the GOCE common-mode accelerations in the gradiometer reference frame, obtained with the multi-arc technique for a period of 3, 12 and 24 days (with the formal error between brackets for the longest period) in July and December 2009

To conclude, it can be stated that the multi-arc technique is only a good approach to determine the scale factors for GOCE in X- and Y-direction when not flying drag-free. In that case, the obtained parameters do not deviate statistically significant from one, which indicates that the in-flight calibration of the gradiometer is done well.

Chapter 7

Conclusions and outlook

The main objective of the research described in this dissertation was to develop and implement a method to calibrate accelerometer measurements of LEO satellites by processing them with a GPS based orbit determination technique. The batch least squares estimator of the GHOST software suite, providing reduced dynamic orbits, is adapted to process accelerometer measurements. Data from the CHAMP, GRACE and GOCE satellite missions have been analyzed with the developed method. For the first two missions, calibration parameters were estimated on a routine basis for a 5 year period. In other research, such as gravity field determination, these parameters are adjusted together with the gravity field coefficients. In this research the calibration parameters themselves are of interest and the orbit products provide insight in the data and processing quality over the long time span. As is shown in the previous chapters, calibration of accelerometers by POD is complicated. In general, in flight direction the calibration can be done precisely. In the other directions, the POD technique is more a validation than a calibration. This is elaborated further in the next section.

First, an overview of the main conclusions of the accelerometer calibration of the before mentioned missions is given. Because the GOCE mission differs from the CHAMP and GRACE missions on several aspects, with the most important one the drag compensation on board of GOCE, the discussion starts with the CHAMP and GRACE cases. Conclusions about the calibration of the GOCE common-mode accelerations are given afterwards. This chapter ends with an outlook discussing topics for further research, which might enhance the current research and might be relevant for the processing of future data sets.

7.1 Conclusions

CHAMP and GRACE accelerometer calibration

For CHAMP and GRACE, the calibration parameters in flight direction can be well determined with the GPS-based orbit determination technique. The accelerometer signal strength is the driving factor to accurately determine the scale. When the non-gravitational signal is strong enough, the along track scale factor can be estimated purely dynamically, without constraints and empirical accelerations, with a consistency level of 0.015 for the GRACE satellites and 0.024 for CHAMP (for a 30 day test period with an above average signal strength and for daily arcs). In the other two directions the accelerometer signal strength is too low to enable a reliable estimation. When the scale factor is not constrained, scale and bias parameters are highly anti-correlated. A much smoother bias series is found when the scale factor is kept constant. In this case, a trend in the bias values and occasional jumps are visible, which can be related to instrument behavior. For the CHAMP satellite, the same trend and jumps were found by the CHAMP project team calibration (H. Lühr, GFZ, private communication). In radial and cross-track direction, the estimation is less stable and strong constraints to a priori bias values are necessary. Otherwise there is a strong correlation with the state vector, resulting in offsets of the estimated orbit in these two directions. Therefore in these two directions this technique is more a validation of the a priori bias and scale values. The best consistency with high-quality reference orbits is obtained when small empirical accelerations are estimated as well (an RMS around mean of 5 nm/s^2), to account for deficiencies in the applied gravitational force models. Over 5 years of CHAMP and GRACE data were processed in this manner, and the calibrated accelerometer measurements were used successfully to retrieve thermosphere density and winds [*Doornbos et al.*, 2009].

From the above it can be concluded that an optimal calibration consists of an iterative procedure, where in the first step daily biases and scale factors are estimated, after which the average of the scale factor is determined. In the second step, this scale factor is kept constant and new bias parameters are estimated, which are no longer explicitly correlated with the scale factor. The scale factor can be obtained with a free estimation or with other techniques, such as the stacked normal matrices approach, where one value for a long period is determined. This is implemented and tested as well. Again the signal strength is the determining factor, as in the multi-arc approach, days with a lower signal strength implicitly have a smaller contribution. With this technique, also in radial and cross-track direction a more reliable scale factor can be estimated compared to the daily estimation. Conceptually, the stacked matrices approach is an optimal technique to estimate the scale parameter.

The developed method results in high quality orbits, comparable to external reduced dynamic trajectories, with a fit of 3.5 cm (3D RMS) for GRACE orbits compared to JPL reduced dynamic orbits and 6.0 cm for CHAMP orbits with respect to reduced dynamic orbit solutions computed with GEODYN. Analysis of SLR residuals supports this quality as well, with an RMS of the residuals below 3 cm for both missions. Ionosphere-free phase residuals fluctuate around 9 mm for the GRACE satellites and are further reduced to about 6 mm when phase center variation maps are applied.

In the GHOST software a cannonball model is used to compute the solar radiation pressure and thus the a priori bias. This is not accurate enough, especially when the angle between the orbital plane and the sun vector increases. A large periodic cross-track offset with respect to external orbits became apparent, correlated with this angle. When an a priori bias determined with more accurate force models is applied, the periodic offset is no longer present (see also section 7.2).

Finally, in case of strong solar activity, the application of accelerometer data is beneficial over the estimation of empirical accelerations, as the accelerometer also picks up the higher frequency part of the experienced accelerations, which are difficult to account for by empirical accelerations [*Van den IJssel and Visser*, 2007].

GOCE orbit determination and common-mode acceleration calibration

In the framework of the GOCE High-level Processing Facility (HPF), rapid kinematic orbits are determined with a latency of one day. These orbits have a precision of around 4 cm (3D RMS) with respect to precise (reduced dynamic) science orbits determined by AIUB, indicating the high quality of the GOCE GPS receiver. Reduced dynamic orbits, after proper tuning, reach a consistency level with the AIUB orbits of 2.5 cm (3D RMS).

Although the GOCE spacecraft also has accelerometers on board, the mission differs from CHAMP and GRACE in several aspects. GOCE flies at an altitude of 254 km which is much lower, resulting in higher aerodynamic forces acting on the spacecraft. These are compensated by the drag-free control system when in science mode, resulting in a small net acceleration in along-track direction. The common-mode accelerations are applied in the precise orbit determination technique, and calibration parameters for these combined measurements are estimated.

When the satellite is not flying in drag-free mode, a scale factor in X- and Y-direction (which predominantly coincide with along track and cross-track direction) can be estimated unconstrained and values close to one are found. The scale in Z-direction is constrained to one because of the small signal in this direction. When the drag compensation is active, also the the scale factor in X-direction is kept constant at one, as the common-mode signal in this direction is also small now. The bias parameter in flight direction can still be estimated reliably. The scale parameter in Y-direction shows a larger variation from one in this case, as a part of the ion thrust also works in this direction. A constant scale factor in all directions, constraining the bias in Y- and Z-direction to a priori values and estimating empirical accelerations, results for both months in the best orbit fit, below 5 cm with respect to external reduced dynamic orbits, with no offsets in any direction.

Two one month data sets are processed, to check the stability of the common-mode calibration parameters. For a period when GOCE was not flying drag-free, July 2009, the estimated scale factor in X- and Y-direction is stable when estimated freely, with respectively variations of 0.01 and 0.03. A second period corresponds to December 2009, with GOCE in science mode and flying drag-free. Now only the scale parameter in Y-direction is estimated freely and the resulting average value is smaller than one and also the variation is higher, up to 0.09. These two months are also processed with the stacked matrices approach, and results of this technique support that the signal strength is the driving factor for a reliable estimation of the scale parameter. From all obtained results, it can be concluded that there is no indication that the scale factors for GOCE are statistically different from one.

7.2 Outlook

As already mentioned, over 5 years of CHAMP and GRACE accelerometer data are processed. The processing of the accelerometer data will be continued for the rest of the lifetime of both missions, with CHAMP probably reaching the end of its lifetime in the summer of 2010 and GRACE lasting for more years to come. Also GOCE is interesting for this kind of research, where the common-mode accelerations in flight direction have to be augmented by the thrust of the ion-engine to retrieve the total aerodynamic force acting on the satellite. The Swarm mission will also carry accelerometers (status May 2010), and the calibration method described in this dissertation can readily be applied to this mission, as each Swarm satellite will carry an accelerometer, a GPS receiver and star cameras for attitude observation.

Furthermore, as shown earlier, the force modeling in the GHOST software, certainly of the solar radiation pressure, can be improved, e.g. by considering a more advanced box model. Also the procedure to obtain the calibration parameters can be improved, which now involves some manual interference. It can be implemented such that only one orbit determination run is necessary, where the calibration parameters are a by-product of the precise reduced dynamic orbit.

The GOCE results presented in this dissertation are limited in scope, as they stem from preliminary analysis because of the short time available to analyze and process them. More in depth analysis have to be performed. First, different combinations of accelerometer measurements can be formed and applied in the precise orbit determination, to check whether the combinations are consistent or some perform better. Also the individual accelerometer measurements can be used, if corrected for gravitational and rotational effects. This allows a calibration of the individual accelerometers, instead of the combination used in the common-mode accelerations [*Visser*, 2009]. Because the total non-gravitational acceleration on the spacecraft is measured, it can be investigated if the ion engine thrust can be applied for calibration purposes, e.g. by changing the thrust as is done when executing manoeuvres (see section 6.3.3). Finally a GOCE gravity field model can be applied, as only pre-launch models are used for the analysis presented here (at the time of research, no final GOCE gravity field models were available yet).

In the coming years the European Galileo system will become operational, and also the improved Russian GLONASS and newly developed Chinese BEIDOU system. Additional observations will not help to resolve fundamental problems, such as unobservability due to small signal strength (e.g. drag-free control) or high correlations between certain estimated parameters. However, the different systems can help to mitigate such problems. The amount of available highly precise phase observations each epoch will increase, which can augment the strength of the estimated orbit. However, as the research in this dissertation pointed out, calibration of accelerometer data by GPS based POD is limited by other factors than observation accuracy and availability.

As pointed out earlier, the acceleration signal strength is the most important factor for a stable estimation of calibration parameters. In flight direction the developed method gives reliable results, where in the other directions it is more a validation of scale factors (obtained e.g with a multi-arc technique) and bias parameters derived from dynamic models, by comparing with high-quality reference orbits. These models, both non-gravitational and gravitational, can further be improved.

Bibliography

Andrés, J.I. (2007), *Enhanced Modelling of LAGEOS Non-Gravitational Perturbations*, Ph.D. dissertation, Delft University of Technology, ISBN 978-90-5623-081-4.

B.D.Tapley, J.C. Ries, S. Bettadpur, and M. Cheng (2007), Neutral density measurements from the gravity recovery and climate experiment accelerometers, *Journal of Spacecraft and Rockets*, *44*(6), 1220–1225.

Bettadpur, S. (2003), Recommendation for a-priori Bias & Scale Parameters for Level-1B ACC Data (Release 00), GRACE TN-04-02.

Bettadpur, S. (2007), Gravity recovery and climate experiment product specification document (rev 4.5 – february 20, 2007), Center for Space Research, The University of Texas at Austin.

Bierman, G.J. (1977), *Factorization Methods for Discrete Sequential Estimation*, Academic Press, Inc., New York.

Bock, H., A. Jäggi, D. Svehla, G. Beutler, U. Hugentobler, and P. Visser (2007), Precise Orbit determination for the GOCE satellite using GPS, *Advances in Space Research*, *39*, 1638–1647.

Brown, R.G., and P.Y.C. Hwang (1997), *Introduction to Random Signals and Applied Kalmann Filtering*, John Wiley and Sons, New York.

Bruinsma, S., D. Tamagnan, and R. Biancale (2003), Atmospheric densities from CHAMP/STAR accelerometer observations, *Planetary and Space Sciences*, *52*, 297–312, DOI: 10.1016/j.pss.2003.11.004.

Case, K., G. Kruizinga, and S. Wu (2002), *GRACE Level 1B data product user handbook*, NASA Jet Propulsion Laboratory, Jet Propulsion Laboratory, Pasadena, JPL Publication D-22027.

Cesare, C., and G. Catastini (2005), Gradiometer on-orbit calibration procedure analysis. Technical note to ESA, GO-TN-AI-0069, Issue 3, Alenia Aerospazio.

Chapront-Touze, M., and J. Chapront (1988), ELP 2000-85: a semi-analytical lunar ephemeris adequate for historical times, *Astron. Astrophys.*, *190*, 342–352.

Cunningham, L.E. (1970), On the computation of the spherical harmonic terms needed during the numerical integration of the orbital motion of an artificial satellite, *Celestial Mechanics*, *2*, 207–216.

Danzmann, K. (2000), LISA mission overview, *Advances in Space Research*, *25*(6), 1129–1136, February 2000.

DeBra, D.B. (1973), Disturbance compensation system design, *APL Technical Digest 12*, pp. 14–26, April–June 1973.

Doornbos, E., H. Klinkrad, and P. Visser (2005), Atmospheric density calibration using satellite drag observations, *Advances in Space Research*, *36*, 515–521.

Doornbos, E., M. Förster, B. Fritsche, T. Van Helleputte, J. van den IJssel, G. Koppenwallner, H. Lühr, D. Rees, and P. Visser (2009), Air density models derived from multi-satellite drag obervations, final report, ESA, ESTEC contract 21022/07/NL/HE.

Dow, J.M., R.E. Neilan, and G. Gendt (2005), The International GPS Service (GPS): celebrating the 10th anniversary and looking to the next decade, *Advances in Space Research*, *36*(3), 320–326.

Drinkwater, M.R., R. Floberhagen, R. Haagmans, D. Muzi, and A. Popescu (2003), GOCE: ESA's first Eearth Explorer core mission, in *Earth gravity field from space - from sensors to Earth sciences, vol. 18 of Space Sciences Series*, edited by G.B. Beutler, pp. 419–432, Kluwer academic publishers.

Edwards, P.G, B. Berruti, P. Blythe, J. Callies, S. Carlier, C. Fransen, R. Krutsch, A.R. Lefebvre, M. Loiselet, and N. Stricker (2006), The MetOp satellite - weather information from polar orbit, ESA Bull 127:8-17.

ESA (1999), *Gravity Field and Steady-State Ocean Circulation Explorer, Reports for Assessment: The Four Candidate Earth Explorer Core Missions*, ESA SP-1233(1), ESA Publications Division, ESTEC, Noordwijk.

Estey, L. H., and C. M. Meertens (1999), TEQC: The Multi-Purpose Toolkit for GPS/GLONASS Data, *GPS Solutions*, *3*(1), 42–49.

Flury, J., S. Bettadpur, and B.D. Tapley (2008), Precise accelerometry onboard the GRACE gravity field satellite mission, *Advances in Space Research*, *42*(8), 478–484.

Foerste, C., F. Flechtner, R. Schmidt, R. Stubenvoll, M. Rothacher, J. Kusche, K.-H. Neumayer, R. Biancale, J.-M. Lemoine, F. Barthelmes, J. Bruinsma, R. Koenig, and U. Meyer (2008), EIGEN-GL05C - A new global combined high-resolution GRACE-based gravity field model of the GFZ-GRGS cooperation, in *General Assembly European Geosciences Union (Vienna, Austria 2008), Geophysical Research Abstracts, Vol. 10, Abstract No. EGU2008-A-06944*.

Förste, Ch. (2002), Format Description: The CHAMP Data Format, CH-GFZ-FD-001.

Förste, Ch., and S. Choi (2005), CHAMP Accelerometer Preprocessing at GeoForschungsZentrum Potsdam, in *Earth Observation with CHAMP, Results from Three Years in Orbit*, edited by Ch. Reigber *et al.*, pp. 169–174, Springer Berlin Heidelberg, Heidelberg.

Francou, G., L. Bergeal, J. Chapront, and B. Morando (1983), Nouvelles ephemerides du Soleil, del la Lune et des planetes, *Astron. Astrophys.*, *128*, 124–139.

Friis-Christensen, E., H. Lühr, D. Knudsen, and R. Haagmans (2008), Swarm - an Earth observation mission investigating geospace, *Advances in Space Research*, *41*(1), 210–216.

Fritsche, B., M. Ivanov, A. Kashkovsky, G. Koppenwallner, A. Kudryavtsev, U. Voskoboinikov, and G. Zhukova (1998), Radiation pressure forces on complex spacecraft, final report, ESOC contract 11908/96/D/IM, HTG, Germany and ITAM, Russia.

Frommknecht, B. (2007), *Integrated sensor analysis of the GRACE mission*, Ph.D. dissertation, TU München.

Frommknecht, B., U. Fackler, and J. Flury (2006), Integrated sensor analysis of GRACE, in *Observation of the Earth system from space*, edited by J. Flury *et al.*, pp. 99–114, Springer.

Gill, E. (1996), Smooth bi-polynomial interpolation of Jacchia 1971 atmospheric densities for efficient satellite drag computation, *DLR–GSOC IB 96–1*, German Aerospace Center (DLR).

Gopalswamy, N., L. Barbieri, E.W. Cliver, G. Lu, S.P. Plunkett, and R.M. Skoug (2005), Introduction to violent Sun-Earth connection events of October-November 2003, *Journal of Geophysical Research*, *110*(A09S00).

Hedin, A.E., E.L. Fleming, A.H. Manson, F.J. Schmidlin, S.K. Avery, R.R. Clark, S.J. Franke, G.J. Fraser, T. Tsuda, F. Vial, and R.A. Vincent (1996), Empirical wind model for the upper, middle and lower atmosphere, *Journal of atmospheric and terrestrial physics*, *58*(13), 1421–1447.

Helleputte, T. Van (2004), Reduced dynamic orbit determination with GPS observations, Master's thesis, Delft University of Technology.

Helleputte, T. Van, and P. Visser (2008), GPS based orbit determination using accelerometer data, *Aerospace Science and Technology*, *12*(6), 478–484.

Helleputte, T. Van, P. Visser, and E. Doornbos (2009), CHAMP and GRACE accelerometer calibration by GPS-based orbit determination, *Advances in Space Research*, *43*, 1890–1896.

Hofmann-Wellenhof, B., H. Lichtenegger, and J. Collins (2001), *GPS Theory and Practice*, Springer Verlag, New York.

Hugentobler, U., M. Meindl, G. Beutler, H. Bock, R. Dach, and A. Jäggi (2008), CODE IGS analysis center technical report 2003/04. In: Gowey K. (ed) IGS technical reports 2003/04, IGS Center Bureau, JPL, CA.

Husti, G.J. (2000), *Global Positioning System, een inleiding*, Serie on Mathematical Geodesy and Positioning, Delft University Press, Delft, The Netherlands, In Dutch.

IGSCB (2009), IGS Products, http://igscb.jpl.nasa.gov/components/prods.html, Last accessed: 2009.

IJssel, J. van den, and P.N.A.M. Visser (2007), Performance of GPS-based accelerometry: CHAMP and GRACE, *Advances in Space Research*, *39*(10), 1597–1603.

IJssel, J. van den, P.N.A.M. Visser, and E.P. Rodriguez (2003), CHAMP Precise Orbit Determination Using GPS Data, *Advances in Space Research*, *31*(8), 1889–1895, doi: 10.1026/S0273-1177(03)00161-3.

Jacchia, L.G. (1971), Revised Static Models of the Thermosphere and Exosphere with Empirical Temperature Profiles, *SAO Special Report 332*.

Jäggi, A., U. Hugentobler, and G. Beutler (2006), Pseudo-stochastic orbit modeling techniques for low-Earth orbiters, *Journal of Geodesy*, *80*(1), 47–60.

Jäggi, A., R. Dach, O. Montenbruck, U. Hugentobler, H. Bock, and G. Beutler (2009), Phase center modeling for LEO GPS receiver antennas and its impact on precise orbit determination, *Journal of Geodesy*, *83*, 1145–1162.

Kim, J., and B.D. Tapley (2002), Error Analysis of a Low-Low Satellite-to-Satellite Tracking Mission, *Journal of Guidance, Control, and Dynamics*, *25*(6).

Knocke, P.C., J.C. Ries, and B.D. Tapley (1988), Earth Radiation Pressure Effects on Satellites, in *Proceedings of the AIAA/AAS Astrodynamics Conference, 88-4292-CP*, pp. 577–587.

Koop, R., T. Gruber, and R. Rummel (2006), The status of the GOCE high-level processing facility, in *Third GOCE User Workshop, 6-8 November, 2006, Frascati, Italy, ESA SP-627*, pp. 199–205.

Kouba, J. (2002), *A Guide to Using IGS Products*, Geodetic Survey Division, Natural Resources Canada, Ottowa, Ontario.

Kroes, R. (2006), *Precise Relative Positioning of Formation Flying Spacecraft using GPS*, Ph.D. dissertation, Delft University of Technology, ISBN 90-8559-150-3.

Lichten, S.M. (1990), Estimation and filtering for high-precision GPS positioning applications, *Manuscripta Geodaetica*, *15*, 159–176.

Liu, H., H. Lühr, S. Watanabe, V. Henize, W. Köhler, and P. Visser (2006), Zonal winds in the equatorial upper thermosphere: Decomposing the solar flux, geomagnetic activity, and seasonal dependencies, *Journal of Geophysical Research*, *111*(A07307), doi: 10.1029/2005JA011415.

Loiselet, M., N. Stricker, Y. Menard, and J.p. Luntama (2000), GRAS-MetOp's GPS-based atmospheric sounder, ESA Bull. 127:8-17.

May, J.A. (1980), A study of the effects of state transition matrix approximations, Proceedings of a Symposium held at Greenbelt, MD, Oct. 17-18, 1979, *NASA CP 21123*, NASA/GSFC.

McCarthy, D.D. (1996), IERS Conventions, 1996, *IERS Technical Note 21*, Central Bureau of IERS, Observatoire de Paris, Paris.

McCarthy, D.D., and G. Petit (2003), IERS Conventions, 2003, Observatoire de Paris, Paris.

Meehan, T.K., D. Robison, T.N. Munson, L.E. Young, and S. Stoyanov (2006), Orbiting GPS receiver modified to track new L2C signal, in *Record - IEEE PLANS, Position Location and Navigation Symposium*, pp. 1071–1073.

Misra, P., and P. Enge (eds.) (2001), *Global Positioning System: Signals, Measurements and Performance*, Ganga-Jamuna Press, Lincoln, MA.

Montenbruck, O. (2000), Quaternion Representation of BIRD Orientation and Reference System Transformations, *Technical Note TN 00–03*, German Space Operations Center.

Montenbruck, O., and E. Gill (2000), *Satellite Orbits: Models, Methods and Applications*, Springer Verlag, Heidelberg.

Montenbruck, O., and R. Kroes (2003), In-flight performance analysis of the CHAMP BlackJack GPS Receiver, *GPS Solutions*, *7*(2), 74–86, DOI: 10.1007/s10291-003-0055-5.

Montenbruck, O., T. Van Helleputte, R. Kroes, and E. Gill (2005*a*), Reduced dynamic orbit determination using GPS code and carrier measurements, *Aerospace Science and Technology*, pp. 261–271.

Montenbruck, O., J. Williams, T. Wang, and G. Lightsey (2005*b*), Preflight Validation of the IGOR GPS Receiver for TerraSAR-X, *Technical Note GTN–TST–0200*, German Space Operations Center.

Montenbruck, O., M. Garcia-Fernandez, Y. Yoon, S. Schön, and A. Jäggi (2008*a*), Antenna phase center calibration for precise positioning of LEO satellites, *GPS Solutions*, DOI: 10.1007/s10291-008-0194-z.

Montenbruck, O., Y. Andres, H. Bock, T. Van Helleputte, J. van den IJssel, M. Loiselet, C. Marquardt, P. Silvestrin, P. Visser, and Y. Yoon (2008*b*), Tracking and orbit determination performance of the GRAS instrument on MetOp-A, *GPS Solutions*, (2), 289–299, DOI: 10.1007/s10291-008-0091-2.

NASA (2002), Studying the Earth's gravity from space: the Gravity Recovery and Climate Experiment (GRACE), *NASA Facts, Doc. No. FS–2002–1–029–GSFC*, NASA.

Perosanz, R. (2003), *On board evaluation of the STAR accelerometer, in First CHAMP Mission Results*, 11–18, Springer Verlag.

Perosanz, R., R. Biancale, S. Loyer, J.M. Lemoine, A. Perret, P. Touboul, B. Foulon, G. Pradels, L. Grunwald, T. Fayard, N. Vales, and M. Sarrailh (2003), On board evaluation of the STAR accelerometer, in *First CHAMP Mission Results*, pp. 11–18, Springer Verlag.

Perosanz, R., R. Biancale, J.M. Lemoine, N. Vales, S. Loyer, and S. Bruinsma (2005), Evaluation of the CHAMP accelerometer on two years of mission, in *Earth Observation with CHAMP, Results from Three Years in Orbit*, edited by Ch. Reigber *et al.*, pp. 77–82, Springer Berlin Heidelberg.

Picone, J.M., A.E. Hedin, D.P. Drob, and A.C. Aikin (2002), NRLMSISE-00 empirical model of the atmosphere: Statistical comparisons and scientific issues, *Journal of Geophysical Research*, *107*(A12), doi: 10.1029/2002JA009430.

Press, W.H., B.P. Flannery, S.A. Teukolsky, and W.T. Vetterling (eds.) (1992), *Numerical recipies in C-the art of scientific computing*, Cambridge University Press, Cambridge.

Reichinger, H., F. Griesauer, F. Zangerl, A. Consoli, F. Piazza, and A. Garcia-Rodriguez (2006), A highly integrated modular European spaceborne dual frequency GPS receiver, in *NAVITEC'2006*, Noordwijk, the Netherlands, December 11–13 2006.

Reigber, Ch., R. Bock, C. Förste, L. Grunwaldt, N. Jakowski, H. Lühr, P. Schwintzer, and C. Tilgner (1996), CHAMP Phase B - Executive Summary, *STR96/13*, GeoForschungsZentrum, Potsdam.

Reigber, Ch., H. Lühr, and P. Schwintzer (2002), CHAMP mission status, *Advances in Space Research*, *30*(2), 129–134.

Remondi, B.W. (1991), NGS second generation ASCII and binary orbit formats and associated interpolation studies, in *Proceedings of the twentieth general assembly, International Union of Geodesy and Geophysics*, Vienna, Austria, August 11–14 1991.

Schmid, R., P. Steigenberger, G. Gendt, M. Ge, and M. Rothacher (2007), Generation of a consistent absolute phase center correction model for GPS receiver and satellite antennas, *Journal of Geodesy*, (81), 781–798, DOI:10.1007/s00190-007-0148-y.

Schutz, B.E., B.D. Tapley, P.A.M. Abusali, and H.J. Rim (1994), Dynamic orbit determination using GPS measurements from TOPEX/POSEIDON, *Geophysical Research Letters*, *21*(19), 2179–2182.

Sentman, L. H. (1961), Free molecule flow theory and its application to the determination of aerodynamic forces, *LMSC–448514*, Lockheed Missiles & Space Company.

Shampine, L.F., and M.K. Gordon (eds.) (1975), *Computer Solution of Ordinary Differential Equations*, Freeman and Comp., San Francisco.

Silvestrin, P., R. Bagge, M. Bonnedal, A. Carlström, J. Christensen, M. Hägg, T. Lindgren, and F. Zangerl (2000), Spaceborne GNSS radio occultation instrumentation for operational applications, in *Proceedings of ION-GPS-2000 Conference*, pp. 872–880, Salt Lake City.

Spofford, P.R., and B.W. Remondi (2009), The National Geodetic Survey Standard GPS Format, ”http://www.ngs.noaa.gov/orbits/sp3_docu.txt”, Last accessed: March 2009.

Svehla, D., and M. Rothacher (2003), CHAMP Double Difference Kinematic POD with Ambiguity Resolution, in *First CHAMP Mission Results for Gravity, Magnetic and Atmospheric Studies*, edited by C. Reigber *et al.*, pp. 70–77, Springer Verlag, Berlin.

Tapley, B.D., B.E. Schutz, and G.H. Borne (2004*a*), *Statistical Orbit Determination*, Elsevier Academic Press, Burlington, MA.

Tapley, B.D., S. Bettadpur, J.C. Ries, P.F. Thompson, and M. Watkins (2004*b*), GRACE measurements of mass variability in the Earth system, *Science*, *305*(5683), 503–505.

Teunissen, P.J.G. (2000), *Adjustment theory, an introduction*, Serie on Mathematical Geodesy and Positioning, Delft University Press, Delft, The Netherlands.

Teunissen, P.J.G., and A. Kleusberg (1998), GPS Observation Equations and Positioning Concepts, in *GPS for Geodesy*, edited by P.J.G. Teunissen and A. Kleusberg, Springer Verlag, Heidelberg.

Tiberius, C., N. Jonker, and F. Kenselaar (1999), The Stochastics of GPS Observables, *GPS World*, pp. 49–54, February 1999.

Touboul, P. (2001), Space Accelerometers: Present Status, in *Gyros, Clocks, Interferometers...: Testing Relativistic Gravity in Space*, edited by C. Lämmerzahl *et al.*, p. 273291, Springer Berlin, Heidelberg.

UT/CSR (2004), GRACE Gravity Model GGM02, http://www.csr.utexas.edu/grace/gravity/ggm02/GGM02_Notes.pdf, University of Texas, Center for Space Research, Last accessed: September 2008.

UT/CSR (2006), UT/CSR Ocean Tide Models, ftp://ftp.csr.utexas.edu/pub/grav/OTIDES.TOPEX 4.0, University of Texas, Center for Space Research, Last accessed: November 2006.

Visser, P.N.A.M. (2008), Exploring the possibilities for star-tracker assisted calibration of the six individual GOCE accelerometers, *Journal of Geodesy*, *82*(10), 591–600.

Visser, P.N.A.M. (2009), GOCE gradiometer: estimation of biases and scale factors of all six individual accelerometers by precise orbit determination, *Journal of Geodesy*, *83*, 69–85.

Visser, P.N.A.M., J. van den IJssel, T. Van Helleputte, H. Bock, A. Jäggi, G. Beutler, D. Svehla, U. Hugentobler, and M. Heinze (2008), Orbit determination of the GOCE satellite, *Advances in Space Research*, *43*(5), 760–768.

Woo, K.T. (2000), Optimum semicodeless carrier-phase tracking for L2, *Navigation*, *47*(2), 82–99.

Wu, J.T., S.C. Wu, G.A. Hajj, W.I. Bertiger, and S.M. Lichten (1993), Effects of antenna orientation on GPS carrier phase, *Man. Geodetica*, *18*, 91–98.

Wu, S.C., T.P. Yunck, and C.L. Thornton (1991), Reduced-dynamic technique for precise orbit determination of low Earth satellites, *Journal of Guidance Control and Dynamics*, *14*(1), 24–30.

Wu, S.C., G. Kruizinga, and W. Bertiger (2006), Algorithm Theoretical Basis Document for GRACE Level-1B Data Processing V1.2, *D–27672*, JPL Pasadena.

Yunck, T.P., S.C. Wu, J.T. Wu, and C.L. Thornton (1990), Precise tracking of remote sensing satellites with the Global Positioning System, in *IEEE Transactions on Geoscience and Remote Sensing*, vol. 28, pp. 108–116.

Yunck, T.P., W.I. Bertiger, S.C. Wu, Y. Bar-Sever, E.J. Christensen, B. Haines, S.M. Lichten, R.J. Muellerschoen, Y. Vigue, and P. Willis (1993), First assessment of GPS-based reduced dynamic orbit determination on Topex/Poseidon, *Geophys. Res. Lett.*, (21), 2179–2182.

Zin, A., S. Landenna, A. Conti, L. Marradi, and Di Raimondo M.S (2007), ENEIDE: an experiment of a Spaceborne, L1L2 Integrated GPS/WAAS/EGNOS Receiver, *Microgravity - Science and Technology*, *19*(5–6), 54–59.

Zumberge, J.F., and G. Gendt (2001), The demise of selective availability and implications for the International GPS Service, *Physics and Chemistry of the Earth*, *26A*(6–8), 637–644.

Curriculum Vitae

Tom Van Helleputte was born in Gent (Belgium) on April 13th, 1980. He attended secondary school at the Sint-Lievenscollege in Gent, and graduated in the science & mathematics class. After that he studied Aerospace Engineering at the Delft University of Technology. In June 2004 he graduated cum laude with a Master's thesis on reduced dynamic orbit determination of LEO satellites, at the Astrodynamics and Satellite Systems group. During that time he did an internship at the German Space Operations Center (GSOC) of the DLR. After graduation he worked in industry for some time, and in September 2005 took on a PhD position at the same group, under the supervision of Prof. B.A.C. Ambrosius and dr. P.N.A.M. Visser. During his PhD research he spent two months at GSOC in 2008, to continue collaboration with Dr. O. Montenbruck. From September 2010 on, he is working at Septentrio Satellite Navigation N.V., in Leuven, Belgium, as GNSS/INS engineer.

Acknowledgements

This research is the result of 5 years of hard work, during which a lot of people helped and supported me. Here I want to put them in the picture. First of all, I want to thank my daily supervisor and co-promotor Pieter Visser for giving me the opportunity and freedom to work on this subject, as well as the supervision to conclude it and the reviews of this dissertation. I also owe a lot to Oliver Montenbruck, for the use of the GHOST software, the collaboration through email and during my visit to the German Space Operations Center of the DLR and the support at my first conference abroad. Finally, I want to thank my promotor Boudewijn Ambrosius, for hiring me in the first place and running such a nice group to work in. Hereby I want to greet all the colleagues of the Astrodynamics and Satellite Systems group, and say a word to some in person: Jose, for the work on GOCE and POD related subjects, and the pleasant company during the GOCE meetings; Eelco, for leading the density project in a successful way and always asking me for new sets of calibration parameters; Luuk, for sharing an office for a great deal of the time; Marc, for the support on computer related topics, and discussions on one of my passions, music; Wim, fellow Belgian and my final office mate; and Relly, for taking care of lots of practical things.

I also owe my gratitude to the European Space Agency, for funding of the GOCE HPF consortium and the study on density retrieval of multi-satellite drag observations. For the former I want to thank all HPF colleagues for the interesting meetings, under the guidance of Reiner Rummel and Rune Floberhagen and specially mention Heike Bock and Adrian Jäggi for the support and collaboration on POD related topics. For the latter, I want to thank Roger Haagmans and Michael Kern for the guidance of the study and the discussions on calibration related topics.

Work without pleasure is an unsuccessful combination, therefore I had the pleasure to find two good friends when I started my PhD. Bert and Jef, you were sitting too close to the coffee machine not to pass by. I appreciate your fun company and good taste (in music and beer to name two). Here I want to thank Marlene as well, for the same company, the open and welcome door, and the great pizzas. Next, I want to thank my old housemates, Wim, Peter, Bert, Sepp, and Guido, Gandert and Bram (and their wives or girlfriends), for your friendship, the lovely dinners and travels, a place to sleep, discussions on work and politics, being my pappenheimer, and a ceiling to fall through. Although I never shared a house with her, Lene fits here as well. My more recent housemates, Miet, Francesca, Pablo and Stijn, thanks for sharing that nice place in the center of Delft. The 'Buities', for the great dinners and mailing-list discussions and the Promood board members when I joined them. All friends from my study time in Delft, and specially Roeland and Tom, for the continued interest in my work and pleasure. Although only mentioned here, she should be at the top: Tine, thanks for always being there. My other friends in and around Gent, thanks for not minding my frequent coming and going and all the good times. And Emma, you were the first to look up my papers, not out of scientific interest, and you are my blood buzz.

Finally I want to thank my family, Leen and Pim, and Bert and Ted, it feels good to live in your neighbourhood (again). To my parents I want to say the biggest thank you, for supporting me in all of my (sometimes strange) choices, and the welcome home, whenever I'm there, expected or unexpected.

To conclude, sometimes someone asked me if the satellites (on which I based my research) were still flying. In answer to that I always said yes (and changed subject), here I want to add 'they keep on flying, they always will*, and that's their beauty'.

Tom Van Helleputte, Gent, August 2010

* the CHAMP mission ended on September 19, 2010